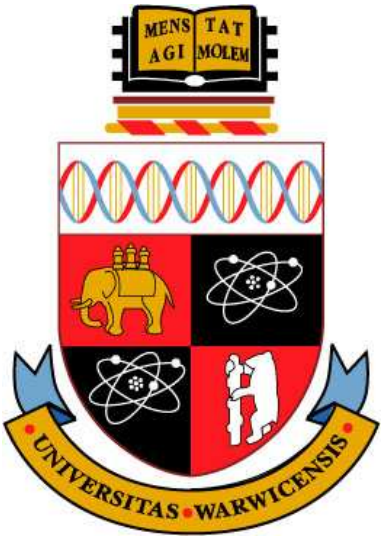

The Orbital Period Distribution of Cataclysmic Variables from the Sloan Digital Sky Survey (SDSS)

by

MONIHAR DILLON

Thesis

Submitted to the University of Warwick

for the degree of

Doctor of Philosophy

Department of Physics

November 2008

THE UNIVERSITY OF WARWICK

"... our hopes and expectations, black holes and revelations..."

MUSE: Starlight

Contents

List of Tables **vii**

List of Figures **viii**

Acknowledgments **x**

Declarations **xi**

Abstract **xiii**

Chapter 1 Introduction **1**

1.1 The Nature of Cataclysmic Variables 1

1.2 CV Evolution 4

1.2.1 Magnetic Braking 5

1.2.2 Gravitational Radiation 7

1.3 Populations, Distributions and the Standard Scenario of CV Evolution 8

1.4 CV Classification 12

1.4.1 Non-magnetic CVs 12

1.4.2 Magnetic CVs 15

1.5 Spectroscopic Properties of CVs 18

1.5.1 White Dwarf 18

1.5.2 Secondary Star 19

1.5.3 Accretion Disc 19

Chapter 2 The CV Population, Observational Selection Effects and Surveys 21

2.1 The Missing Period 'Spike' and the Missing CV Population 21

2.2 Observational Selection Effects and Surveys Past and Present 25

2.2.1 Sloan Digital Sky Survey (*SDSS*) 28

Chapter 3 Observations and Data Reduction 32

3.1 Observations and Data Reduction 32

3.1.1 Photometry 33

3.1.2 Spectroscopy 33

3.1.3 CCD Data Reduction 33

3.2 Telescopes and Instrumentation 36

3.3 Log of Observations/Summary of System Properties 37

3.4 Time-Series Analysis 44

3.4.1 Fourier Analysis and Acquisition of Data 44

3.5 `MIDAS` Utilities for Time-Series Analysis 46

3.5.1 Fourier Type Methods 46

3.5.2 Phase-Folding/Analysis of Variance Methods 48

3.6 Analysis of Photometric Data 52

3.7 Analysis of Spectroscopic Data 53

3.8 Bootstrapping 54

3.9 Monte Carlo Simulations 55

Chapter 4 Time-Series Photometric Observations of 15 CVs Identified by the SDSS 57

4.1 Introduction 58

4.2 Results on Individual Systems 59

4.2.1 SDSS J00183454. 59

4.2.2 SDSS J0027−0108 (EN Cet). 63

4.2.3 SDSS J0151+1400. 63

4.2.4 SDSS J0748+2905. 64

4.2.5 SDSS J0824+4931. 65

4.2.6 SDSS J0854+3905 (EUVE J0854+390). 66

4.2.7 SDSS J0901+4809. 67
4.2.8 SDSS J0904+4402. 68
4.2.9 SDSS J0919+0857. 70
4.2.10 SDSS J1244+6135. 72
4.2.11 SDSS J1250+6655. 72
4.2.12 SDSS J1514+4549. 73
4.2.13 SDSS J1711+3013. 73
4.2.14 SDSS J2116+1134. 74
4.2.15 SDSS J2154−0901. 76
4.3 Discussion 76
4.4 Conclusions 80

Chapter 5 Time-Series Spectroscopic and Photometric Observations of 14 CVs Identified by the SDSS. 82

5.1 Introduction 82
5.2 Results on Individual Systems 85
5.2.1 SDSS J0802+4010 85
5.2.2 SDSS J0808+3131. 86
5.2.3 SDSS J0903+3300. 86
5.2.4 SDSS J0932+4725. 87
5.2.5 SDSS J1249+0357. 88
5.2.6 SDSS J1457+5148. 89
5.2.7 SDSS J1538+5123 90
5.2.8 SDSS J1610+4459. 91
5.2.9 SDSS J1703+3209. 91
5.2.10 SDSS J2048−0610. 91
5.2.11 SDSS J2101+1052. 92
5.2.12 SDSS J2234+0041. 93
5.2.13 SDSS J2258−0949. 94
5.2.14 SDSS J2303+0106. 94
5.3 Discussion 95

5.4 Conclusions 99

Chapter 6 The Period Minimum Spike **100**

6.1 Introduction 100

6.2 Orbital Period Measurements 101

6.3 The Orbital Period Distribution of the SDSS CVs 107

6.4 Properties of the Period-Spike CVs found by SDSS 110

6.5 Discussion 115

6.5.1 Deep, Deeper, the Deepest 115

6.5.2 Caveats? 122

6.5.3 Implications on CV Population Models 124

6.6 Conclusions 126

Chapter 7 Conclusions and Future Work **128**

7.1 Results in Context 128

7.2 Current State of the Field 135

7.3 The Future of Understanding Binary Evolution 137

List of Tables

3.1 Log of Observations for Chapter 4: Photometric Observations. 40

3.2 Log of Observations for Chapter 5: Photometric and Spectroscopic Observations. 42

4.1 Eclipse Timings for SDSS J0901+4809 and SDSS J1250+6655 69

5.1 Eclipse Timings for SDSS J0903+3300 and SDSS J0932+4725 89

5.2 Radial Velocity Measurements of SDSS J1249+0357 89

5.3 Comparison of Photometric and Spectroscopic Sample Properties 97

6.1 Newly identified SDSS CVs 103

6.2 Previously Known CVs 105

6.3 Comparison of SDSS, HQS and PG and their potential for discovering period-minimum CVs 116

6.4 WZ Sge candidate systems brighter than $V \simeq 17$ identified prior to SDSS 125

List of Figures

1.1 Roche-lobe Geometry 3
1.2 Alternative AML Prescriptions 7
1.3 Orbital Period Distribution from Ritter and Kolb (2003) 9
1.4 Evolution of a Single CV from Howell (2000) 11
1.5 Schematic of 2 types of Cataclysmic Variable 12
1.6 Analysis of the Period Distribution by Aungwerojwit (2007) 17
1.7 Spectra of SDSS J0837,SDSS J1137,SDSS J1138,SDSS J1339 20

2.1 Percentage of Systems at Various Mass Transfer Rates 23
2.2 Observed and Synthesised Orbital Period Distribution of CVs under 116 mins . 24
2.3 CVs, QSO's and Stars in Colour Space. 30

3.1 Data Reduction Process 34
3.2 Light-Curves and Periodograms of SDSS J0854 50
3.3 Light-Curves and Periodograms of SDSS J1244 51

4.1 ID Spectra and Light-Curves SDSS J0018 to SDSS J2154 60
4.2 Periodograms for 11 CVs from Photometric Observations 62
4.3 Periodograms for SDSS J0748+2905 65
4.4 Periodograms for SDSS J0018+3454 66
4.5 Monte Carlo Simulation for SDSS J0904+4402 using INT data. 71
4.6 Monte Carlo Simulation for SDSS J0904+4402 using NOT data. 71
4.7 Monte Carlo Simulation for SDSS J0919+0857 using CAFOS data 72

4.8 Periodograms for SDSS J1514+4549 74
4.9 Periodograms for SDSS J1711+3013 75
4.10 Monte Carlo Simulation for SDSS J1711+3013 75
4.11 Photometric Periods vs Ritter and Kolb Distribution 78
4.12 Photometric Periods vs Ritter and Kolb Distribution KS Test 79

5.1 ID Spectra for SDSS J0802 to SDSS J2303 83
5.2 Phased Radial Velocity Plots and Periodograms 84
5.3 Phase-Folded Lightcurves and Periodograms 85
5.4 Stacked Spectra of SDSS J1249+0357 90
5.5 Trail Spectra of SDSSJ 1457+5148, SDSS J1703+3209 and SDSS J2101+1052 92
5.6 Spectroscopic and Photometric Periods vs Ritter and Kolb Distribution 98
5.7 Spectroscopic and Photometric Periods vs Ritter and Kolb Distribution KS Test 98

6.1 Comparisons of Orbital Period Distributions 108
6.2 Two-sided Kolmogorov-Smirnov Comparing Orbital Period Distributions . . . 110
6.3 Venn Diagram of SDSS CVs with Accurate Orbital Periods 113
6.4 Spectra of SDSS CVs 114
6.5 Magnitude Limits Applied to the SDSS CV Sample. 123

7.1 My Sample vs SDSS CVs vs Ritter and Kolb Distribution 130
7.2 Photometric Periods vs Spectroscopic Periods KS Test 131
7.3 Magnitude limit for SDSS CVs 138

Acknowledgments

First I would like to thank my supervisor Boris Gänsicke, for his help, support and guidance throughout my PhD, without whom, none of this would have been possible. I would also like to thank, Tom Marsh and Danny Steeghs, for their advice and support and readiness to answer all my questions astronomy related and otherwise. I would also like to thank Pablo Rodríguez-Gil for the reduction of the spectroscopic data used in thesis, and to all those mentioned in Tables 3.1, 3.2 for their significant contribution and effort in obtaining the data used in this thesis.

I would also like to give a special thanks to John Southworth, for his help and advice and efforts in proof-reading this thesis, and Jaroslaw ‘Grok’ Zachwieja for helping me with my computer related problems.

On a very personal note, I would like to thank the following wonderful people, in no particular order; David Russell, Susana Barros, David Collins, Nesrin Refai, Adam Aitkenhead and Jim Collett. Thank you for the long lunches, even longer telephone conversations, professional input and friendship.

And last but not least, I’d like to give my deepest thanks and gratitude to my husband Allan Dillon for his love, patience and unwavering devotion throughout these very long years.

Declarations

I, Monihar Dillon declare that the work presented in this thesis has not been submitted in any previous application for a degree at a university. The contents of this thesis represents my own work, except where references to other works are given and where contributions made by my collaborators has also been appropriately referenced.

Chapter 3, contains details on observations and data reduction contributed by my collaborators. All spectroscopic data was handled and reduced by Dr. P. Rodríguez-Gil; Instituto de Astrofísica de Canarias at Tenerife, Spain.

Chapter 4, is based on a refereed publication that was submitted during the course of my studies.

Dillon, M. and Gänsicke, B. T. and Aungwerojwit, A. and Rodríguez-Gil, P. and Marsh, T.R. and Barros, S.C.C. and Szkody, P. and Brady, S. and Krajci, T. and Oksanen, A. "Orbital periods of cataclysmic variables identified by the SDSS. III. Time-series photometry of 15 systems obtained during the 2004/5 International Time Project on La Palma". *2008MNRAS.386.1568D*.

Chapter 5, is based on a publication due for submission in July 2008.

Dillon, M. and Gänsicke, B. T. and Aungwerojwit, A. and Rodríguez-Gil, P. and Marsh, T.R. and Barros, S.C.C. and Szkody, P. "Orbital periods of cataclysmic variables identified by the SDSS. III. Time-series spectroscopy of 14 systems obtained during the 2004/5 International Time Project on La Palma". *Dillon et al. 2008b in prep*.

Chapter 6, is based on a publication due for submission in May 2008, in which I am named second author. Chapter 6; Sections 6.4, 6.5 and 6.6 are authored solely by B.T. Gänsicke.

B.T. Gänsicke, M. Dillon, P. Rodríguez-Gil, J. Southworth, J. Thorstensen, A. Aungwerojwit, T.R. Marsh, P. Szkody, S.C.C. Barros, J. Casares, D. de Martino, P.J. Groot, P. Hakala, U.

Kolb, S.P. Littlefair, I.G. Martínez-Pais, G. Nelemans, M.R. Schreiber “SDSS unveils the predicted population of intrinsically faint cataclysmic variables at the minimum orbital period”. *Gänsicke et al. 2008 in prep.*

Abstract

Over the years, substantial effort has gone into calculating models of the intrinsic population of galactic Cataclysmic Variables (CVs). However, comparison with the observed properties of the known CV sample has consistently failed to match the predictions put forward by the 'disrupted magnetic braking' model of CV evolution. Some of the discrepancies have been blamed on the heterogeneous set of known CVs, which are not well-suited for a quantitative test of the population models.

The Sloan Digital Sky Survey (SDSS) has dramatically improved the observational side of CV population studies. Sampling a large volume in *ugriz* colour space and extending deeper than any previous large-scale survey, SDSS provides the most homogeneous and complete sample of CVs to date.

At the time of writing, the sample of SDSS CVs contains 213 systems, of which 177 are new discoveries. Establishing the detailed properties of these CV is a major task. The work presented in this thesis is part of a larger effort to derive the orbital period distribution of SDSS CV sample.

In this thesis, I present my contribution and results of time-series photometric and spectroscopic observations of a total of 29 SDSS CVs. I provide a discussion of their properties and determine orbital periods for 20 systems. I also provide a quantitative analysis of the new sample of CVs from SDSS and compare their intrinsic qualities with the previously known population of CVs.

The results show that the period distribution of the SDSS CVs differs from that of the previously known CVs at a 3-σ level. A substantially larger fraction of below-the-gap to above-the-gap systems is observed, accompanied by a prominent accumulation of CVs at the orbital period minimum. This result is important, as the accumulation of systems at short orbital periods has been long theorised but never proved observationally. More specifically, the origin of the 80–86 min period spike is entirely due to the new CVs identified in SDSS. The systems in the period spike also differ in spectral morphology and accretion activity from the longer-period CVs. Indeed $\sim$ 20% of the CVs identified by SDSS have white-dwarf dominated spectra indicating low mass transfer rates and late spectral type donors, the majority of which have been found close to the period minimum.

A homogeneously selected sample of CVs, with well defined parameters has been long overdue and the results from SDSS are very promising. With this improved observational evidence, theoretical models can be modified to re-address the discrepancies in the current theories that have long plagued our understanding of CV evolution.

Chapter 1

Introduction

1.1 The Nature of Cataclysmic Variables

Observational evidence has shown that the majority of stars in the Universe are either formed and/or exist in multiple systems. As a consequence, a large fraction of these will interact at some point in their lifetime. ($\backsim$ 50% according to Iben 1991). In the case of 'wide' binary systems, with large orbital separations, the presence of an additional component is unlikely to significantly influence the stellar evolution. However in 'close' or interacting binaries, the decrease in orbital separation and/or the expansion of a star and subsequent mass transfer will alter the evolution of each stellar component. As a result the initial mass of a star on the zero age main sequence (ZAMS) is no longer the sole parameter determining its evolution (Iben 1991; Postnov & Yungelson 2006).

The importance of observing close and interacting binary stars cannot be over-estimated. These systems are precursors to some of the most exotic phenomena in the Universe: binary black hole candidates, milli-second pulsars, candidates for Type Ia supernovae – used as extra-galactic distance indicators, and double degenerate systems – thought to be sources of gravitational radiation and possible progenitors of gamma-ray bursts. Systems in which mass transfer via an accretion disc can be observed provide ideal laboratories for an understanding of the accretion onto compact objects, formation of young stellar objects (YSOs) and planet formation, as well as providing insight into the mechanisms responsible for powering much larger-scale phenomena such as active galaxies and quasars.

Interacting binaries of particular value are Cataclysmic Variables (CVs). These systems are composed of a white dwarf (WD) 'primary', accreting material via an accretion disc from a late-type main-sequence 'secondary'.

The majority of observed CVs have magnitudes, $12 \lesssim \mathrm{V} \lesssim 20$, with short periods, most of which are between $80\mathrm{min} \lesssim \mathrm{P_{orb}} \lesssim 6\mathrm{hr}$. They are also numerous, which allows for systematic population studies to be carried out on them. In fact a large arsenal of analytical methods can be used to derive their properties in detail: time-resolved photometry and spectroscopy (from X-ray to IR), Doppler tomography, eclipse mapping, polarimetry and stellar atmosphere modelling. All these methods can be used to determine distances, masses, densities, magnetic field strengths, temperatures, orbital and spin periods etc. providing a wealth of information for astronomers on stellar evolution.

The geometry and shape of the stellar components of a CV is defined by the Roche potential dictated by the mass ratio of the component stars $q = M_2/M_1$, where M_1 is the mass of the white dwarf primary (WD), M_2 is the mass of the secondary, and a is the binary separation. The critical equipotential surface of a Roche lobe defines the maximum volume in space within which orbital material is gravitationally bound to that star. It is also the surface at which the two lobes touch at the inner Lagrangian point ($\mathrm{L_1}$), which lies along a line joining the centres of the binary components. At the $\mathrm{L_1}$ point, the gravity of the stellar components and the centripetal force in the rotating system cancel.

An illustration of the Roche lobe geometry of a CV is shown in Figure 1.1, including the Lagrangian points $L_1 - L_5$. The Lagrangian points, are locations where the forces within the system cancel out. L_1, is the inner Lagrangian point encompassed by the Roche lobe – the saddle point through which matter can flow from the secondary into the gravitational well of the WD. L_2 or 'outer Lagrangian' point is the easiest gateway by which matter can escape from the gravitational field of the system. L_3 located on the opposite side is a region of higher potential to L_2. The points of greatest potential are at L_4 and L_5.

Using the centre of the primary as the origin for a Cartesian co-ordinate system (x,y,z), the z-axis is parallel to the rotation axis and the x-axis lies along the line joining the centres of the two stars. The y-axis lies perpendicular to the other two axes. The position of the secondary lies at $(a, 0, 0)$, with the centre of mass at $(\mu a, 0, 0)$, where $\mu = M_2/(M_1 + M_2)$. The total potential

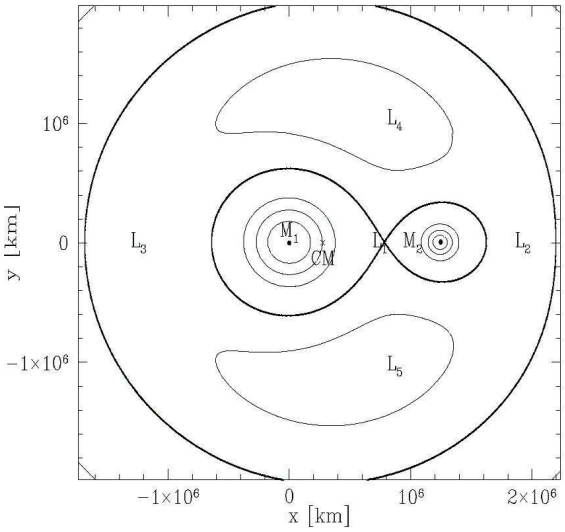

Figure 1.1: Roche lobe geometry and equipotential surfaces for a Cataclysmic Variable with $q = 1/3$. M_1 is the white dwarf primary (WD), M_2; the secondary. The locations of the Lagrangian points $L_1 - L_5$, where the forces within the system cancel out are also shown. Provided by B. Gänsicke

in the Roche equipotentials, Φ = constant, is given by the sum of the gravitational potential of both stars plus the rotational potential (Pringle & Wade, 1985).

$$\Phi = -\frac{GM_1}{(x^2+y^2+z^2)^{1/2}} - \frac{GM_2}{((x-a)^2+y^2+z^2)^{1/2}} - \frac{\Omega^2}{2}[(x-\mu a)^2+y^2] \qquad (1.1)$$

$G = 6.67 \times 10^{-11}\mathrm{m^3kg^{-1}s^{-2}}$, is the gravitational constant.

$\Omega = 2\pi/P_{\mathrm{orb}}$

The relationship between the orbital separation a and orbital period P_{orb} of the binary about the common centre of mass is given by Kepler's 3^{rd} law.

$$a^3 = \frac{G(M_1+M_2)P_{\mathrm{orb}}^2}{4\pi^2} \qquad (1.2)$$

The radius of the secondary varies due to its distorted shape. In accordance to Eggleton (1983) a sphere containing the same volume as the Roche lobe has a radius:

$$R_{L(2)} = \frac{a0.490q^{2/3}}{0.6q^{2/3} + \ln(1+q^{1/3})} \qquad \text{for all } q \qquad (1.3)$$

The criterion for Roche lobe overflow for an object of an average density $\bar{\rho}$ with a volume-equivalent radius for the Roche lobe, $R_{L(2)}$, as shown by Eggleton (1983) is:

$$\bar{\rho} = \frac{M_2}{\frac{4\pi}{3} R_{L(2)}^3} = 1.07 \times 10^5 P_{\rm orb}^{-2}(\rm h) \quad [\rm kgm^{-3}] \quad (0.01 \leq q \leq 1) \tag{1.4}$$

Due to the relatively small separation between the two stellar components, the secondary is able to fill its Roche lobe and a mass transfer stream forms at the L_1 point. An immediate consequence of this Roche lobe filling is that the spin period of the donor star in the CV becomes tidally locked with the orbital period, i.e. $P_{\rm orb} = P_{\rm spin}$. The material is initially propelled by the thermal pressure from the stellar atmosphere of the secondary and on passing through the L_1 point, is then under the gravitational influence of the white dwarf. The material carries with it excess angular momentum which must be lost in order for it to be accreted onto the WD. The result is the formation of an accretion disc where viscous interactions allow for the dissipation of energy. Angular momentum is transferred outwards so that material is able to flow onto the surface of the white dwarf. The total potential energy released during the accretion of matter onto the WD is given by:

$$L_{\rm acc} = \frac{G M_{\rm wd} \dot{M}}{R_{\rm wd}} \tag{1.5}$$

$M_{\rm wd}$ = white dwarf mass

$R_{\rm wd}$ = white dwarf radius

$\dot{M}$ = accretion rate.

1.2 CV Evolution

Binaries destined to become CVs begin as systems consisting of an intermediate-mass main-sequence star ($1 - 10 M_\odot$) with a low-mass companion ($M \lesssim 1 M_\odot$), with orbital periods on the order of years. As the more massive star evolves, it expands to become a red giant filling its Roche lobe transferring its outer layers onto its companion.

However, mass transfer in this configuration from a massive companion to the lower-mass counterpart is dynamically unstable. The transferred material moving away from the centre

of mass gains momentum, so the binary compensates by a decrease in separation. This allows for mass transfer to continue as the massive companion maintains Roche lobe contact.

As more material is transferred, a runaway feedback loop is triggered and the entire envelope of the red giant is dumped onto the companion. The material now fills both Roche lobes forming a cloud encompassing both stars – this is the 'Common Envelope' phase (Paczynski, 1976; Iben & Tutukov, 1993).

The effect of orbiting in such an environment causes drag on the stars dissipating their orbital energy. The stars then spiral inwards transferring a significant amount of angular momentum to the envelope. This extremely efficient process means the binary is able to decrease its separation from $\sim 100R_{\odot}$ to $\sim 1R_{\odot}$ in as little as 10^3 years. If the energy deposited in the envelope exceeds the binding energy, the envelope will be ejected into interstellar space.

On emerging from the common envelope phase, the system is now either a CV or a pre–CV, which is essentially a detached white dwarf plus main–sequence binary. There is no mass transfer in a pre–CV as there is no Roche lobe contact. The system evolves towards shorter orbital periods and into Roche lobe contact and stable mass transfer through further loss of angular momentum.

The evolution of cataclysmic variables is determined by the rate at which angular momentum ($\dot{J}$) is lost from the binary orbit. In a CV we have a case where mass is being transferred from a low-mass companion onto a higher-mass WD. The secondary is therefore further away from the centre of mass and, due to the conservation of angular momentum, the binary compensates for the transfer of mass by increasing the stellar separation. As a result, the secondary detaches from its Roche lobe and mass transfer ceases. In order for Roche lobe contact to be maintained and stable mass transfer to continue, the orbital separation must decrease, and this occurs through the loss of angular momentum.

There are at least two mechanisms by which CVs lose angular momentum, gravitational radiation and magnetic braking.

1.2.1 Magnetic Braking

The cause of magnetic braking is the interplay between the ionised stellar wind of the secondary and the stellar magnetic field. The mechanisms by which these fields are produced - perhaps by

a dynamo action deep within the star, where convection forces bubbles of gas to move in circular motions - is poorly understood. Many stars are observed to possess strong magnetic fields. It also appears that rapid rotation of a star enhances the strength of the magnetic field. Since tidal forces ensure that the spin of a secondary is locked to the orbital period, giving a rotation period of hours as opposed to a similar type single star with a rotational period of days, the secondaries in CVs are thought to be highly magnetic.

As matter in a stellar wind is forced to flow along and to co-rotate with the magnetic field lines, it is accelerated off to greater distances and then thrown off into space taking with it a substantial amount of angular momentum.

The effect of the angular momentum loss is to brake the rotation of the secondary. Since the star's rotational period is locked to the orbital period, the angular momentum is supplied by the orbit which then shrinks in consequence. The rates of mass transfer via magnetic braking are typically $10^{-9} - 10^{-8} \mathrm{M}_{\odot}\mathrm{yr}^{-1}$ (Howell et al., 2001).

The efficiency of magnetic braking is uncertain (Section 2.2). However the rate at which angular momentum is lost from the system, following the standard scenario of magnetic braking of Verbunt & Zwaan (1981) and Rappaport et al. (1983), the angular momentum loss (AML) due to magnetic braking is given by:

$$\dot{J}_{\mathrm{MB}} = -3.8 \times 10^{30} M_2 R_{\odot}^4 \left(\frac{R_2}{R_{\odot}}\right)^{\gamma} \left(\frac{2\pi}{P_{\mathrm{orb}}}\right)^{\gamma} \tag{1.6}$$

where γ governs the efficiency of the magnetic braking process.

Figure 1.2 shows alternative angular momentum loss prescriptions for a Cataclysmic Variable with a WD of $0.6 M_{\odot}$ (Schreiber & Gänsicke, 2003). The dotted lines represent the two different versions of the 'standard' disrupted magnetic braking (Verbunt & Zwaan, 1981) where $\gamma = 2$ and $\gamma = 4$. $\gamma = 2$ is the most frequently used in the context of CV evolution. The solid line in the plot represents the revised empirical angular momentum loss prescription derived by Sills et al. (2000) from open cluster data of single stars. The abrupt decrease in $\dot{J}$ corresponds to the 'shut-off' in magnetic braking for a donor of mass $M_2 < 0.3 M_{\odot}$. The dashed line represents angular momentum loss by gravitational radiation only, and represents a lower limit on $\dot{J}$.

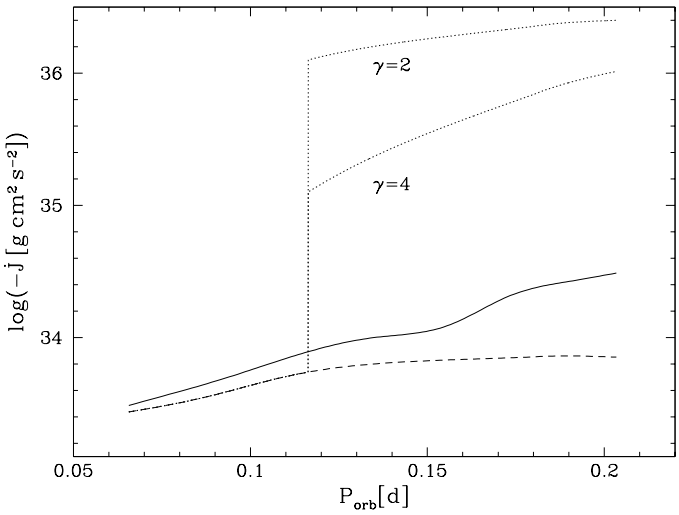

Figure 1.2: Alternative angular momentum loss prescriptions for a Cataclysmic Variable with a WD of $0.6M_{\odot}$ (Schreiber & Gänsicke, 2003). The dotted lines represent the two different versions of the 'standard' disrupted magnetic braking (Verbunt & Zwaan, 1981). The revised empirical angular momentum loss prescription is represented by the solid line (Sills et al., 2000). The decrease in $\dot{J}$ corresponds to the shut-off in magnetic braking. The dashed line represents angular momentum loss by gravitational radiation only.

The corresponding timescale for angular momentum loss (Kolb & Stehle, 1996) is:

$$\tau_{\rm MB} = -\left(\frac{J}{\dot{J}}\right)_{\rm MB} = 2.2 \times 10^9 \frac{M_1 M_2}{(M_1 + M_2)^{1/3}} R_2^{-4} P_{\rm orb}^{10/3}(d) \quad \text{[years]} \tag{1.7}$$

1.2.2 Gravitational Radiation

As systems evolve to shorter periods gravitational radiation becomes a more significant source of angular momentum loss. The repetitive orbit of two stars causes a rhythmic warping in space, which ripples outward in a periodic wave. As the energy to generate the wave is extracted from the binary orbit, the stars slowly spiral inwards. The rate of mass transfer due to gravitational radiation is around $10^{-10}\mathrm{M}_{\odot}\mathrm{yr}^{-1}$ in short-period CVs (Howell et al., 2001).

The rate at which angular momentum is lost to radiation of gravitational waves, from Einstein's quadrupole formula is:

$$\dot{J}_{GR} = -\frac{32G^{7/3}}{5c^5}\frac{M_1^2 M_2^2}{(M_1 + M_2)^{2/3}}\left(\frac{2\pi}{P_{\rm orb}}\right)^{7/3} \tag{1.8}$$

The corresponding timescale for both angular momentum loss via gravitational radiation and magnetic braking respectively (Kolb & Stehle, 1996) is:

$$\tau_{\rm GR} = -\left(\frac{J}{\dot{J}}\right)_{\rm GR} = 3.8 \times 10^{11}\frac{(M_1 + M_2)^{1/3}}{M_1 M_2}P_{\rm orb}^{8/3}(d) \quad \text{[years]} \tag{1.9}$$

In accordance with Kolb & Stehle (1996), CVs found above the gap are thought to be around $1.5\text{x}10^9$ yr old whilst those below the gap are around $3 - 4\text{x}10^9$ yr old. Typical evolutionary timescales for CVs to evolve from $P_{\rm orb} \simeq 10\,\text{hr}$ to $P_{\rm orb} \simeq 2\,\text{hr}$ are $\sim 10^8\,\text{yr}$, and $\sim 10^9\,\text{yr}$ to evolve through the period gap.

1.3 Populations, Distributions and the Standard Scenario of CV Evolution

The orbital period; $P_{\rm orb}$, of a CV is the most easily determined global parameter. As the period of a CV changes on the mass transfer timescale, the distribution of CVs as a function of their orbital period is an important marker of their evolutionary status. The current population of CVs to date with known orbital periods is 675 (Ritter & Kolb 2003,V7.8). Figure 1.3 shows the orbital period distribution of 531 CVs from Ritter & Kolb (2003),V7.3. A number of distinctive features in this distribution are highlighted as follows:

(a). The number of systems dwindles at longer periods.

(b). There is a dearth of systems around 2-3 hrs, known as the period gap.

(c). There is a sharp cut-off of the number of systems around 80 minutes.

(d). There is approximately the same number of systems above and below the period gap.

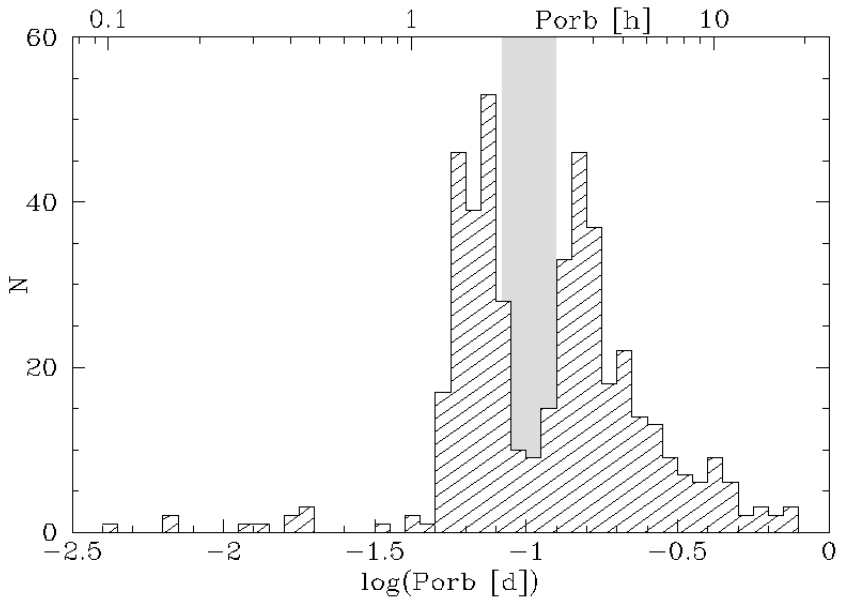

Figure 1.3: Orbital Period distribution of 531 CVs as listed in V7.3 of the Ritter & Kolb (2003) catalogue. The 2-3 hr period gap is indicated in grey. The distribution for $P_{\rm orb} \lesssim 65$min contains degenerate Helium WDs with shorter orbital periods, which are known as AM CVn stars. The discussion of these systems is beyond the scope of this thesis.

The drop in the number of systems at longer periods is easily illustrated by recalling that for stable mass transfer $q = M_2/M_1 \lesssim 1$ – i.e. the secondary star has to be less massive than the primary. Since the WD must be below the Chandrasekhar limit $\approx 1.4 M_\odot$, this value also provides the upper limit for the mass of the red dwarf. Constrained by '$q < 1$' – as long as the donor is not evolved, (see Equation 1.4) this leads to a limit in the orbital period of CVs to around $\approx$ 12hr.

The standard evolutionary model provided to explain the most prominent features of the orbital period distribution is the theory of 'disrupted magnetic braking' put forward by Rappaport et al. (1983); Paczyński & Sienkiewicz (1983); Spruit & Ritter (1983).

A key attribute of this theory is that the evolution of CVs is divided into two distinct phases dependent on the prevailing AML mechanism, and its success lies in its ability to explain the 2-3hr period gap.

The evolution of the orbital periods of binaries reflects the evolution of the donor star. This is governed by two competing mechanisms; the mass transfer which perturbs the thermal equilibrium of the star causing it to expand – the rate of which is described by the mass transfer

timescale $\tau_{\dot{M}} = -M_2/\dot{M}_2$, and the thermal relaxation time – which re-establishes thermal equilibrium and contracts the star to a radius appropriate to its new mass. This is described by the Kelvin-Helmholtz (thermal) timescale $\tau_{KH} \approx GM^2/RL$.

If $\tau_{\dot{M}} \gg \tau_{KH}$ then the secondary is able to contract in response to the mass loss, but if $\tau_{\dot{M}} \ll \tau_{KH}$, then the star will not shrink rapidly enough, and will become over-sized for its mass.

Magnetic braking is deemed to be dominant for systems with periods $P_{orb} > 3$hrs, in which the secondary stars have radiative cores. Initially, $\tau_{\dot{M}} \gg \tau_{KH}$ and the secondary is able to respond quickly to the mass loss, evolving close to the main-sequence. As the mass (M_2) of the secondary decreases, so does its radius (R_2) along with the orbital period; P_{orb}. However as the system continues to evolve, $\tau_{\dot{M}}$ increases but not as fast as τ_{KH} due to its $\approx M^{-2}$ dependency. Eventually $\tau_{\dot{M}} \ll \tau_{KH}$, and the star finds itself with a radius too large for its mass. Its has been driven out of equilibrium.

At $P_{orb} = 3$hrs, ($M_2 \approx 0.3M_\odot$) the secondary stars are thought to become completely convective and magnetic braking is deemed no longer 'effective'. This results in the cessation of mass transfer, allowing the secondary to shrink within the limits of the Roche lobe to its equilibrium. Roche lobe contact is lost and mass transfer ceases, the binary becomes detached and the system evolves towards shorter orbital periods through angular momentum loss via gravitational radiation. As there is no mass transfer these systems are relatively faint and difficult to observe. A number of actively accreting CVs that are found within the period gap can be explained by systems which achieve the first Roche lobe contact and hence begin mass transfer within the period gap.

At $P_{orb} \simeq 2$hrs, the binary separation has decreased through loss of angular momentum via gravitational radiation, and the separation between the two stellar components is sufficient for the secondary to fill its Roche lobe again, resuming mass transfer. This time, evolution is driven solely by the less efficient AML mechanism of gravitational radiation (Paczyński, 1981; Paczyński & Sienkiewicz, 1983) leading to longer evolutionary timescales and lower mass transfer rates. As the system continues to evolve the binary separation continues to decrease. As before, the mass transfer timescale increases but not as fast as the thermal timescale and the secondary is driven out of thermal equilibrium. Eventually, the mass of the secondary star becomes so low ($\lesssim 0.08M_\odot$) that hydrogen fusion ceases, and the secondary evolves towards a degenerate

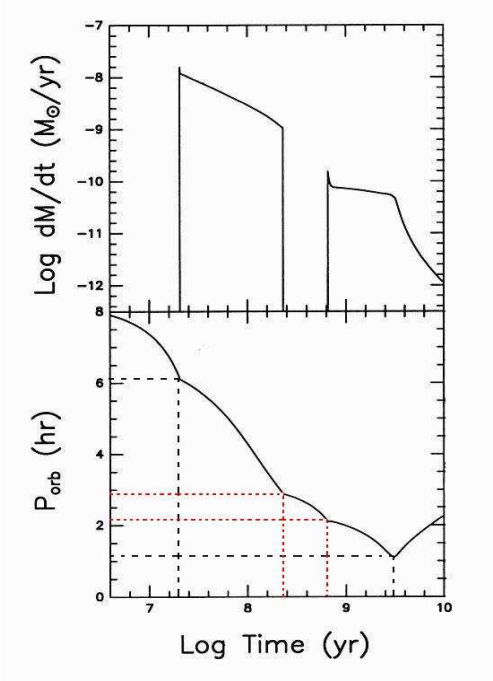

Figure 1.4: The evolution of a single CV with initial masses, $M_2 = 0.9\mathrm{M}_\odot$, $M_{\mathrm{wd}} = 1.1\mathrm{M}_\odot$. This system comes into Roche lobe contact at $\mathrm{P_{orb}} = 6$ hr, and evolves through the period gap to the minimum in $\mathrm{P_{orb}}$ in $2.8\mathrm{x}10^{10}$ yr then evolves towards longer periods. The dotted lines have been added to provide a clearer illustration of the positions of the onset of mass transfer, the upper and lower limit of the period gap and period minimum. Modified from Howell et al. (2001).

state becoming a brown dwarf (BD), where an decrease in mass results in an increase in radius. Consequently, there exists a minimum period, where $\tau_{\dot{\mathrm{M}}} = \tau_{\mathrm{KH}}$. After reaching this point, the CV evolves back to longer periods.

Figure 1.4 provides illustrative support to the previous discussion. The plot shows the evolution of a single CV with initial masses, $M_2 = 0.9\mathrm{M}_\odot$, $M_{\mathrm{wd}} = 1.1\mathrm{M}_\odot$. The system is shown to come into Roche lobe contact at $\mathrm{P_{orb}} = 6$ hr evolving towards shorter orbital periods as its evolution is predominantly driven by magnetic braking. The period gap can be seen clearly in the top panel, here the mass transfer rate drops to zero, but the binary still evolves towards shorter orbital periods (via gravitational radiation) until the secondary fills its Roche lobe at 2 hours. Mass transfer recommences driven by gravitational radiation. This system reaches the period minimum in around $2.8\mathrm{x}10^{10}$ yr, then evolves towards longer periods.

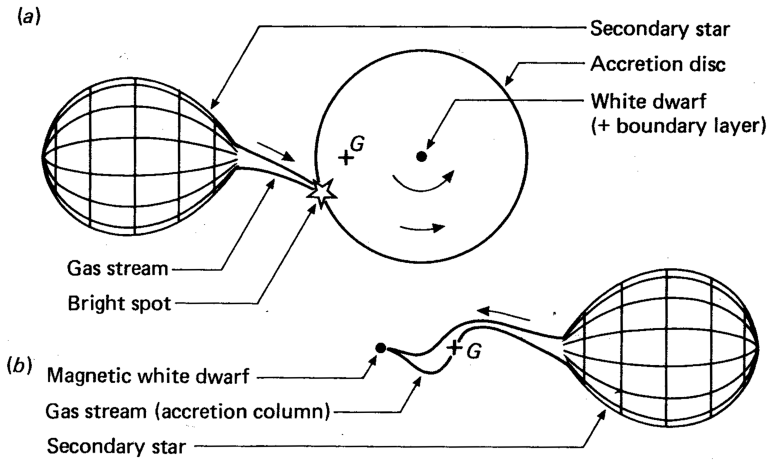

Figure 1.5: An illustration of two types of Cataclysmic Variable. (a) An illustration of a disc-type systems viewed pole on, with the two stars revolve anti-clockwise about the centre of *G*, in the plane of the diagram (b). A system with a strongly magnetised WD. In both diagrams the WD is three times the mass of the secondary. The arrows indicate the direction of the flow of material. As shown in Pringle & Wade (1985).

1.4 CV Classification

In the past the majority of CVs owed their discovery to their optical variability. As scientific and technological advancements allowed for more detailed examination of these enigmatic systems, CVs are now considered in terms of their intrinsic properties. The main physical properties affecting the frequency, period and timescale of variability of a CV are the orbital period of a system (determined by the orbital separation of a system), the mass transfer rate and the strength of the magnetic field of the white dwarf. Schematics of the two major classes of CVs are shown in Figure 1.5. I provide a brief discussion of the various classes and sub-types of CVs below.

1.4.1 Non-magnetic CVs

A non-magnetic CV is composed of a main-sequence secondary and a white dwarf primary with a relatively weak magnetic field ($B < 1.0$MG). The dominant mechanism responsible for fluctuations in the brightness of these systems is due to changes in the rate of mass transfer through the disc affecting the thermal stability of the disc (Osaki, 1974; Smak, 2002). Observations show for systems with lower mass transfer rates, discs are unstable. In these systems, it is believed

that mass transfer from the secondary star occurs at a constant, but higher rate than can be transported through the disc via viscous interactions. As a consequence, material piles up on the disc increasing the surface density until it reaches a critical value. At this point the consequential rise in the temperature has led to the partial ionisation of hydrogen which is extremely sensitive to temperature ($\propto T^{10}$). The disc is thermally unstable. A small rise in temperature means a rapid rise in opacity boosting the viscosity and further increasing the transport of angular momentum through the disc. The material is spread both outward and inward towards the white dwarf. This increased accretion rate – 'outburst', enhances the luminosity of the system and drains the disc of material. Eventually, the disc then drops back into a cooler, lower viscous state – 'quiescence', where it is replenished by the mass transfer stream from the secondary repeating the cycle. This mechanism is responsible for the eruptive phenomena observed in a class of systems known as 'Dwarf novae'.

For systems with higher mass transfer rates, the disc is stable. An equilibrium is reached at a higher surface density above the critical value. These systems exist on the hotter side of the thermal instability. The discs are hotter and the hydrogen is fully ionised and they do not undergo outbursts. These binary systems are therefore intrinsically brighter and are known as 'Novalike' variables.

The material then leaves the accretion disc via a transition region known as the boundary layer. In order for material to accrete onto the WD surface, the velocity of the accreting material must drop significantly. In the boundary layer, the kinetic energy of the slowing material is converted to heat and radiated away, emitting up to half the total luminosity of the system. At high accretion rates the boundary layer can contain enough material to block emerging radiation, making it optically thick.

Dwarf novae (*DN*) represent the most populous CV sub-class ($\sim$ 46% of known CVs) and undergo recurrent fluctuations in brightness by 2–7 magnitudes on quasi-periodic timescales that range from days to years. Examples of dwarf nova sub-types are;

Z Cam (Z Camelopardalis). These systems show periods of rapid outbursts interspersed with periods of stable enhanced accretion known as 'standstills' similar to novalikes. The stand-

stills are initiated by outbursts which allows for the system to exist on the hotter side of the thermal instability where the brightness of the system is sustained mid-way to minimum brightness, lasting from tens of days to years. All Z Cams lie above the period gap.

SU UMa (SU Ursae Majoris). Such binaries undergo less frequent but regular cycles of sustained outbursts known as 'super-outburst', interspersed by normal dwarf nova type outbursts, called 'super-cycles'.

The photometry of super-outbursts reveals a peculiarity, a hump-shaped modulation appearing near super-outburst maximum, occurring at a few percent longer than the orbital period. The origin of these 'super-humps' are thought to be due to tidal instabilities caused by the influence of the gravitational field of the secondary on the accretion disc. For systems with a small enough mass ratio, i.e. $q \leq 0.33$ (necessary for the disc to grow), resonance with the orbital period of the secondary can drive the outer Keplerian orbits of the accretion disc elliptical, causing it to precess. As the orbits in the outer parts of the accretion disc are no longer parallel to neighbouring material, the orbits intersect. Collisions result in the dissipation of energy, resulting in the observed modulations of SU UMa light curves.

The SU UMa class is split into a further two sub-classes, WZ Sge (WZ Sagittae) and ER UMa (ER Ursae Majoris), which is determined by the length of the super-cycle. For SU UMa, these cycle are around a few hundred days, whereas ER UMa stars have super-cycles of 20-50 days, and WZ Sge have super-cycles lasting decades. The majority of SU UMa stars have orbital periods below the gap.

U Gem (U Geminorum). These dwarf nova systems do not show standstills or super-humps and super-cycles, which are the respective characteristics of Z Cam and SU UMa stars.

Novalike Variables (*NL).* These systems represent $\sim$ 15% of CVs in the Ritter & Kolb (2003) catalogue. Existing on the hotter side of the thermal instability, these systems are stuck in 'permanent outburst', also known as high states. Examples of Novalike sub-types are;

VY Scl (VY Sculptoris). These systems undergo periods of 'low states' and are some-

times termed ‘anti-dwarf-novae’. In these low states, the systems fade by several magnitudes during which the mass transfer rate drops dramatically or shuts off entirely for periods of several weeks to years. During these low states, these systems look spectroscopically similar to quiescent dwarf novae, but do not undergo outbursts.

SW Sex (SW Sextantis). First proposed as a class by Thorstensen et al. (1991a), they represent nearly 40% of the total population of novalikes. The majority of SW Sex stars are eclipsing and are preferentially found at 3hr $\lesssim P_{\rm orb} \lesssim$ 4hr (Rodríguez-Gil et al., 2007b; Rodríguez-Gil, 2005). These systems display several peculiar characteristics.

- Single-peaked emission lines, with absorption dips at particular phases.
- A high-velocity feature is seen to zig-zag across the line profiles moving with the orbital cycle and extending far into the line wings.
- Odd V-shaped eclipse profiles in high-inclination systems.
- Spectra show moderately strong He II 4686Å emission lines.

UX UMa (UX Ursae Majoris). The spectra of these systems display persistent broad Balmer absorption line spectra, indicative of optically thick discs seen at low inclination. These systems do not undergo low states.

1.4.2 Magnetic CVs

There are systems in which the magnetic field significantly affects the accretion process. These systems are further subdivided into Polars, also known as AM Her (*AM Herculis*) stars, where $B_{\rm wd} \sim 10 - 200$MG and intermediate polars also known as IPs (*Intermediate Polars*), $B_{\rm wd} \sim 1 - 10$MG. There is an overlap between the system types around the boundary values, determined by the interplay between the strength of the magnetic field and the rate of accretion, which influences the size and extent of the inner magnetically-dominated region (magnetosphere) in relation to the outer weaker magnetic region, which can be modelled as non-magnetic.

AM Her (AM Herculis). The strength of the magnetic field of the WD in these binaries prevents the formation of an accretion disc. The field is so strong that it is able to interact with the smaller magnetic field of the secondary, forcing the system to become spin-synchronised with the WD and controlling the flow of stellar material via the magnetic field lines (Warner, 1995).

The material is channelled to one or two accretion spots near the poles at supersonic velocities under free-fall via an accretion column on passing through a standing shock above the surface of the WD. The column is composed of a hot dense plasma of accreted material and is a source of hard X-rays. Some of these X-rays and accreted material passing through the shock are able to heat the surface of the WD where the re-radiated emission is in the form of soft X-rays.

It is this interaction of matter in the presence of a strong magnetic field and hot plasma that gives rise to cyclotron radiation and polarisation that are the defining characteristic of AM Her stars. There is preference of polars to be found below the period gap.

IPs (Intermediate Polars). These systems have the combined characteristics of a magnetic system and a non-magnetic system in one. They have accretion discs which are truncated at smaller radii by the magnetic field of the WD. In an intermediate polar the magnetic field is either too weak, or the separation between the stellar components too large, to synchronise the orbital period of the secondary to the spin period of the WD. The WD often rotates with the spin period of $P_{\rm spin} \sim 0.1 P_{\rm orb}$ (Patterson, 1994; Norton et al., 2004).

The nature of IPs are primarily confirmed by the pulses seen in the X-ray lightcurves occurring at the spin period and/or the beat period between the spin and orbital cycles due to the accretion processes near the magnetic pole. There are currently 30 IPs known and their orbital periods are concentrated above the gap (Norton et al., 2004).

Only five IPs have been found to emit polarised light, whereas in all polars the emitted light is both linearly and circularly polarised, due to cyclotron emission processes near the surface of the WD. A small number of IPs also show circular polarisation which gives hints of cyclotron beaming effects (see Katajainen et al. 2007 and references therein).

Further analysis of the distribution of various classifications of CV sub-types within the orbital period distribution from the Ritter & Kolb (2003) catalogue, were carried out by

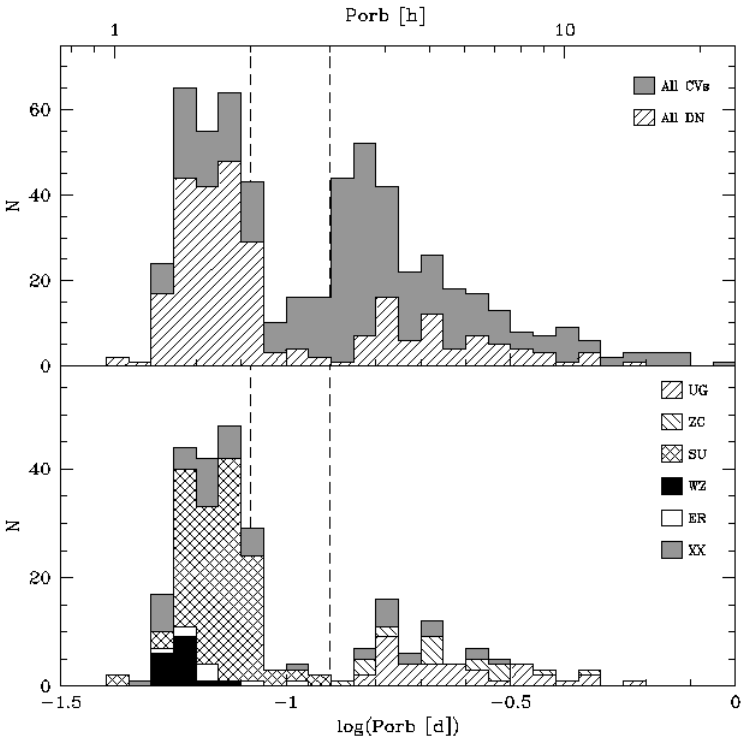

Figure 1.6: CV sub-types; their fractions and ratios from Ritter & Kolb 2003 (V7.5, 2005), as shown in Aungwerojwit (2007).

Aungwerojwit (2007). A summary is provided in the form of Figure 1.6 where details of the ratios of CV sub-types are detailed as follows:

Top panel: shaded grey region shows CVs within the orbital period range of $\sim$ 1hr to $\sim$ 1day having removed all AM CVns (*AM Canum Venaticorum*). 262 systems out of 572 (46%) are dwarf novae (DN), of which 166 (63%) have $P_{\rm orb} \lesssim$ 2hr, 26 (10%) are found in the 2-3 hr period gap, whilst 70 (27%) are found above $P_{\rm orb} \gtrsim$ 3hr.

Bottom panel: displays all known DN according to their sub-types. 159 (61%) SU UMa, 37 (14%) U Gem, 18 (7%) Z Cam and 48 (18%) are unclassified (XX). For completeness the SU UMa class includes 8 ER UMa stars (which have very short outburst cycles) and 19 WZ Sge stars (which have extremely long outburst cycles. All confirmed U Gem and Z Cam stars lie above the gap and a large majority of SU UMa stars (85%) lie below the gap

All the afore-mentioned systems, both magnetic and non-magnetic, can be precursors to much more extreme phenomena;

Classical novae (CN). The origin of a nova explosion is a thermonuclear runaway event on the surface of the WD, caused by the ignition of hydrogen-rich material accumulated from the secondary. During these explosions the brightness of the system can increase by 10 - 20 magnitudes, lasting for as long as weeks to years as the material is thrown outwards into the interstellar medium. The recurrence timescale of a classical nova is $\sim 10^3 - 10^4$ years. $\sim$ 12% of systems in Ritter & Kolb (2003) are listed as classical novae.

Type Ia Supernova (SN Ia). In such cases, the WD primary has accreted enough material from the secondary that it is pushed over the Chandrasekhar limit, $1.4M_{\odot}$. The pressure and temperature increase cause the ignition of carbon within the WD resulting in a runaway thermonuclear reaction which causes the star to explode.

1.5 Spectroscopic Properties of CVs

A great deal of information can be attained from observing the photometric variability of CVs. However, for even greater detail relating to the intrinsic properties of the components of a CV, spectroscopic observations are even more telling.

1.5.1 White Dwarf

White dwarfs in CVs have temperatures typically > 11000K (Gänsicke, 2000; Sion, 1999). As a result the flux of the white dwarf rises steeply towards the UV wavelengths of the electromagnetic spectrum. The spectra of a WD is particularly notable for the broad absorption features originating from the WD atmosphere. This effect is due to the phenomenon of pressure broadening. The high density and intense gravity on the surface of the white dwarf means that atoms are constantly perturbed by neighbouring atoms, which enhance uncertainties in the energies of electron orbits. Photons are able to interact with atoms over a larger range of wavelengths and so the absorption lines are broadened out.

1.5.2 Secondary Star

The majority of secondary stars in cataclysmic variables are K or M type stars, with temperatures ranging from $\sim 5200 - 3900$K and < 3900K respectively. Their flux increases towards the red/infrared wavelengths. The low temperatures of these stars mean that molecules are responsible for many of the features seen in their spectra, apparent as a series of complex dips. These stars show strong metal lines of iron (Fe), titanium (Ti), and calcium (Ca I and Ca II). As one moves from M0 to M9, the strength of titanium oxide lines (TiO) increase, becoming particularly dominant in M type stars, manifesting themselves as a series of strong absorption bands.

1.5.3 Accretion Disc

The temperature of an accretion disc is strongly dependent on the mass transfer rate of a system and can vary from $\sim$ 3000K at the outer edge of the disc, to $\gg$ 30000K through the release of gravitational potential energy close to the WD. The flux contribution is also dependent on whether or not it is in outburst, quiescence or in a high or low state. Typically, the disc emission of a cataclysmic variable can dominate in the UV, dropping off monotonically at longer wavelengths. Lines of low-ionisation species such as hydrogen, (Lyman, Balmer, Paschen), as well as helium (He I), calcium (Ca II), also known as the calcium triplet, and iron (Fe II) are observed. Systems with higher mass transfer rates or strong magnetic fields can be identified by lines of ionised helium (He II) and Bowen fluorescence blend.

Figure 1.7 shows examples of spectra of various CVs, taken from the Sloan Digital Sky Survey (SDSS) database[1]. These systems are; SDSS J0837+3830, a confirmed polar discussed in Szkody et al. (2005) and Schmidt et al. (2005a). The system shows cyclotron humps in the blue plus Balmer emission lines, as well as an M star continuum at longer wavelengths. SDSS J1137+0148 (RZ Leo); discussed in Szkody et al. (2003a), previously catalogued in Downes et al. (2001). This systems shows strong doubled hydrogen Balmer lines (indicating a high inclination system) flanked by broad absorption from the WD. Some He I contribution can be seen. Towards redder wavelengths emission from the secondary is apparent as well as Ca II emission from the disc. SDSS J1138+0322 (T Leo) also discussed in Szkody et al. (2003a)

[1] www.sdss.org

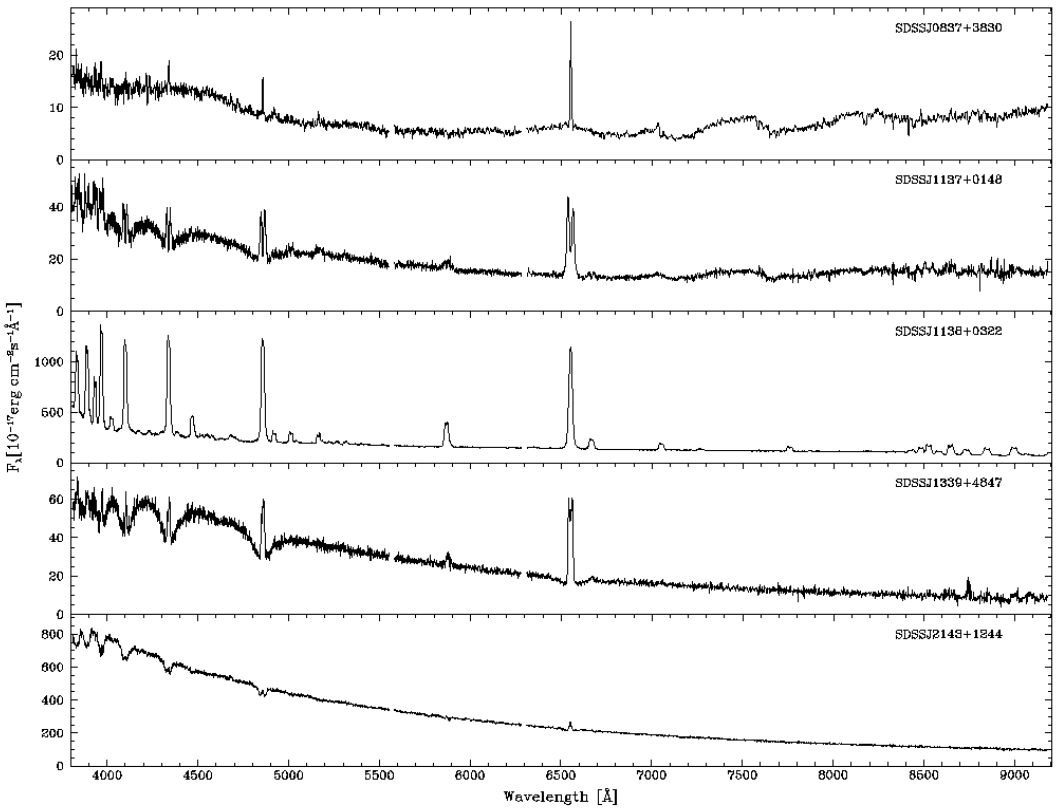

Figure 1.7: *From top to bottom.* A selection of spectra of various SDSS CVs; SDSS J0837+3830 – a polar, SDSS J1137+0148 (RZ Leo) – a high inclination system, SDSS J1138+0322 (T Leo) – a dwarf nova in quiescence. SDSS J1339+4847 – a WD dominated system, SDSS J2143+1244 (HS2143+1244) – a high accretion rate system.

and previously catalogued in Downes et al. (2001). This system shows typical characteristics of a dwarf nova in quiescence. The system is dominated by its accretion disc, displaying prominent hydrogen Balmer and helium lines as well as Ca emission in the infra-red. SDSS J1339+4847 was discussed in Szkody et al. (2005). Further analysis and study of this system (Gänsicke et al., 2006), shows it to contain a WD displaying non-radial pulsations. The spectrum of this system is dominated by the WD showing broad absorption features around the Balmer lines. SDSS J2143+1244 (HS2143+1244) was discussed in Szkody et al. (2005), where the nature of this system was contemplated to be either a system in outburst or a high accretion rate novalike with an optically thick disc. Further investigation, showing the flux to be similar during different observations, indicate it to be the latter.

Chapter 2

The CV Population, Observational Selection Effects and Surveys

2.1 The Missing Period 'Spike' and the Missing CV Population

Whilst the main merit of the 'disrupted magnetic braking' model is in its ability to provide an explanation for the period gap, there is a significant scientific drawback: thus far there has been no observational evidence for a discontinuous change in spin-down rate due to magnetic braking between late-type field stars that are fully convective and those that have a radiative core (Andronov et al., 2003; King & Schenker, 2002).

There are, in fact, a number of severe disagreements between the predictions of the standard model and observational evidence. The response to these failings has been the proposal of several modifications/alternatives (King & Kolb, 1995; Kolb et al., 1998; Patterson, 1998; Kolb & Baraffe, 1999; King et al., 2002; King & Schenker, 2002; Andronov et al., 2003; Barker & Kolb, 2003), none of which have been completely successful in matching all the features observed in the current CV period distribution.

(1) The predicted period minimum is $\approx$ 65 min, whilst the observed value is $\approx$ 80 min (Kolb & Baraffe, 1999; Paczyński, 1971).

The period minimum is a prominent feature of the observed period distribution and is

thought to occur when $\tau_{\dot{M}} = \tau_{KH}$ (Paczyński, 1971; King, 1988). This is the point in the evolution of a binary where the consequence of mass loss has resulted in the transition of the donor star from a main sequence star to a degenerate, brown dwarf. As mass loss continues, the BD responds by expanding adiabatically, as the binary separation increases to compensate for the mass transfer. Roche lobe contact is maintained by the expanding BD, and the system evolves towards longer periods.

The actual period P_{min} at which CVs 'bounce' depends on the ratio $\tau = t_{KH}/t_{\dot{M}}$. If τ is small, then P_{min} is short. Thus P_{min} is sensitive to the orbital angular momentum loss rate which determines the rate of mass transfer $-\dot{M}_2$ and also, to the interior structure of the donor.

Paczyński was the first to point out that $P_{min} \approx 80$ min, if gravitational wave radiation drives the mass transfer. Since then, stellar models with different input physics have been employed to verify a quantitative agreement between the observed and calculated P_{min}. However a number of calculations have thrown a spanner in the works: Kolb & Ritter (1992); Howell et al. (1997); Kolb & Baraffe (1999) notoriously give P_{min} at ≈ 65 min instead of the observed ≈ 80 min.

(2) Population synthesis models show that there should be a significant accumulation of systems near the period minimum, (Paczyński & Sienkiewicz, 1983; Paczyński, 1971) and that 99% of CVs should have orbital periods below the period gap (Howell et al., 1997; Kolb, 1993), whilst the period distribution plot shows similar numbers of CVs above and below the period gap.

The probability of finding a system within a given period range is proportional to the time taken to evolve through this region, $N(P) \propto 1/|\dot{P}|$ (King & Schenker, 2002).

Since $\dot{P} = 0$ at P_{min}, then N(P) must clearly have a significant maximum. Thus compared to the rapid evolution above the period gap, where high mass transfer rates are driven by magnetic braking, there should be large accumulation of systems, corresponding to the slow velocity in period space, driven by a lower mass transfer rates attributed to gravitational wave radiation, which would increase the probability of detection (de Kool, 1992; de Kool & Ritter, 1993; Kolb, 1993; Kolb & Baraffe, 1999).

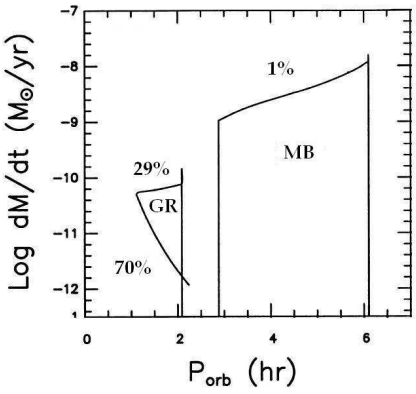

Figure 2.1: The evolution of the orbital period P_{orb} of a system with the mass transfer rate – $\dot{M}$. Also shown are the percentages of systems believed to populate particular stages of the evolution. 99% of systems are theorised to exist below the period gap. Modified from Howell et al. (2001)

Unfortunately observational evidence for the presence of a large population of systems with low mass transfer rates has thus far remained elusive.

Figure 2.1 provides an illustrative support to the discussion. The plot shown shows the percentages of CVs theorised to populated different stages of CV evolution. According to the standard theory 1% of systems are believed to exist above the gap, while 99% have periods below the gap, 70% of all systems should be post period minimum systems. Figure 2.2 from Barker & Kolb (2003) compares the observed orbital period distribution (top panel) to the theorised distribution (bottom panel) for systems below the period gap. The predicted change of mass transfer rate due to gravitational radiation has also been plotted (middle panel). Note the large accumulation in systems 'spike' that is expected to exist at the period minimum of 65 min in the theoretical distribution, which is absent from the observed sample which has a minimum at 80 min.

(3) Population synthesis also suggests that the space density of CVs should range from 10^{-5} – 10^{-4}pc^{-3} (Politano, 1996; de Kool, 1992), whereas the number derived from observations is 10^{-6} – 10^{-5}pc^{-3} (Downes, 1986; Ringwald, 1996; Pretorius et al., 2007b; Araujo-Betancor et al., 2005a; Aungwerojwit et al., 2006).

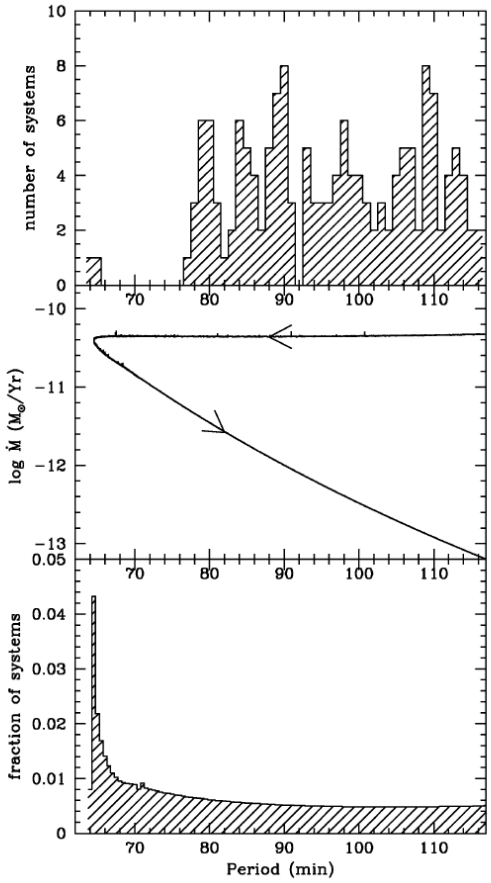

Figure 2.2: *Top panel*: the observed period distribution of CVs with periods less than 116 min (Ritter & Kolb, 1998). *Middle panel*: calculated evolutionary track in the orbital period versus mass rate $\dot{M}$ plane for CVs that evolve under the influence of angular momentum loss via gravitational radiation. The systems reach a period minimum of ~ 65 min. *Lower panel*: period distribution expected from evolutionary trace in middle panel. As shown in Barker & Kolb (2003).

If the standard model is correct, then the vast number of systems below the period gap would infer a high space density. Unfortunately, current observations have so far identified only 1-10% of the predicted CV population (Gänsicke et al., 2002b).

Possible causes of all these discrepancies have been attributed to the uncertainties in CV evolution (King, 1988; Schenker & King, 2002; Andronov et al., 2003; Barker & Kolb, 2003; Taam et al., 2003) as well as observational selection effects, (Downes, 1986; Ringwald, 1996; Gänsicke, 2005).

2.2 Observational Selection Effects and Surveys Past and Present

The CVs in the currently known distribution (see Figure 1.3) have been found through a variety of different means, dictated by the intrinsic nature of the binary systems. These systems have been discovered using one of the following criteria: *variability*; the variation in brightness clearly observed in classical and dwarf novae when undergoing outbursts, *X-ray emission*; especially significant for magnetic CVs, where large amounts of energy are released close to the surface of the WD near the magnetic poles, *peculiar colours* (usually implying blue); the hot component of a CV such as the accretion disc, accretion column and/or WD can dominate, making the system appear blue/UV, and *spectroscopic properties* (composite spectra, emission lines); also useful for identifying systems which cannot be resolved by photometry alone, the presence of strong emission lines, hydrogen (Balmer) and helium (He I) indicate the presence of ongoing accretion.

Dividing the CVs in the Ritter and Kolb distribution according to their method of discovery (Gänsicke, 2005), it has been shown that practically all CVs were found using one of the afore mentioned criteria. Further analysis of CV sub-types showed that 86% of CVs discovered due to their variability are dwarf/classical novae, 57% of CVs discovered via X-ray observations are magnetic CVs, 43% of CVs identified due to their peculiar colours are nova-likes and those that were detected spectroscopically, seemed to show no preference to a particular sub-type. Another interesting feature to note is that plotting the period distribution of CVs according to their method of discovery (Gänsicke, 2005), the defining characteristics of the orbital period distribution i.e. the period gap and the period minimum remain.

The various methods used to identify CVs also brings into question the effects of observational bias on the sample. As the CVs in Figure 1.3 were found by a variety of different means over a number of years, the cumulative effects are difficult to quantify.

The three most dominant selection effects are:

Optical Flux Limits. The simplest of selection effects, the properties of (bolometric) magnitude-limited samples have been studied before (Kolb, 1993; Howell et al., 2001). The assumption is that the observed radiation is the time-averaged accretion luminosity, and CVs are distributed uniformly through space. These assumptions make comparisons of limited use.

Blue Optical Colours. Most known CVs have $U - B < -0.5$ (Bruch & Engel, 1994). This is because for systems with high mass transfer rates, their luminosity is radiated away at blue/UV wavelengths. However, for systems with low mass transfer rates, the accretion-heated WD may be quite cool ($T_{\rm eff} \leq 10\,000$K) meaning the system may only be detectable at optical/red wavelengths. As a result selection cuts in the U-B can exclude the faintest of CVs.

Restrictions in Galactic Latitudes. Restricting observations in Galactic latitudes can create observational biases due to two things. Firstly due to the number of stars available for observation defined by the galactic latitude range. It can be assumed that the vertical density profile of CVs is exponential $\rho(z) = \rho_0 e^{-|z|/h}$, where z is the perpendicular distance from the galactic plane (i.e $z = d\sin b$ where b is the Galactic latitude). The local space density is defined as $\rho = \rho(0)$, the mid-plane value of ρ. This means that there is a rapid drop off in the number of systems available for observation as one moves to higher Galactic latitudes. The second effect is due to the effective volume which can be observed. For instance magnitude-limited surveys at high Galactic latitudes are likely to yield samples very different from those focused on the Galactic plane, because they detect a larger fraction of all systems inside the volume defined by the Galactic range (Pretorius et al., 2007a). These samples are likely to contain more intrinsically fainter (evolved) systems which are relatively close by. For similar magnitude-limited surveys focused along the Galactic plane on the other hand, intrinsically bright objects would be seen out to greater distances than fainter, ones and would be included disproportionately to their space density (Pretorius et al., 2007a). Widely used empirical values of the Galactic scale height of CVs can be found in Patterson (1984). In Pretorius et al. (2007a) the scale-heights were set to $h =$ 120, 260 and 450 pc for long systems, short-period systems and period bouncers respectively.

It is apparent that all samples of CVs are subject to strong selection effects, as a result of observational bias inherent to the parent survey. It therefore imperative to our understanding of CV evolution to acquire a large homogeneous sample of CVs, with well-determined parameters where the effects of observational biases can be accurately modelled and accounted for, giving a truer representation of the intrinsic population of CVs.

The following section provides a brief overview of key surveys that have provided the greatest observational input in the study of CVs.

Palomar Green Survey (*PG*). The Palomar Green high Galactic latitude UV excess survey comprises a statistically complete sample of 1715 stellar objects, covering 10 714 deg^2 to a limiting magnitude of B = 16.2. Observations were taken using the Palomar 18inch Schmidt telescope (San Diego, California) at Galactic latitude $|b| > 30^\circ$ and declination $\delta > -10^\circ$ (Green et al., 1986). Spectroscopic classification was obtained for candidates with U − B < −0.46[1] within the spectral range of 3700Å − 6500Å. Cataclysmic Variables and composite spectrum binaries accounted for 5% of the sample. Of the 70 CV candidates listed by Green et al., intensive follow-up observations revealed only 30 as genuine CVs, four of which were previously known and the rest, mis-identified SdB and other hot high gravity stars, including some detached binaries. The sample contained five SW Sex stars (Thorstensen et al., 1991b), defining the SW Sex stars as a class of CVs in their own right (Ringwald, 1993, 1996).

Edinburgh Cape Survey (*EC*). The Edinburgh Cape blue object survey was very similar in terms of specifications to the Palomar Green survey, and was proposed to address the imbalance between the number of discoveries and objects known between the northern and southern hemispheres.

The survey was designed to detect blue stellar objects (U − B < −0.4) brighter than B = 18 covering an area of sky of 10 000 deg^2 with $|b| > 30^\circ$, $\delta < 0^\circ$ using the UK Schmidt telescope at the AAO (Anglo Australian Observatory). Follow-up spectroscopic observations (3600 − 5200Å) obtained at the South African Astronomical Observatory (SAAO) however are only complete to B = 16.5 (Stobie et al., 1997; Kilkenny et al., 1997). 25 CVs were identified by the EC survey, 15 of which were new discoveries. In fact 2% of blue objects brighter than B = 16.5 were found to be CVs (Chen et al., 2001).

Roentgen Satellite/Position Sensitive Proportional Counter (*ROSAT/PSPC CVs).* The ROSAT /PSPC survey was the first all sky survey in soft X-rays (0.1-2.4keV; 100 − 5Å) and the

[1]Work by Jester et al. (2005) show that the U − B < −0.46 is inaccurate, and is actually U − B < −0.71

extreme UV (0.025-0.2keV; 500 – 60Å) using imaging telescopes (Voges et al., 1999), which has resulted in the identification of 105 924 X-ray sources.

Since the temperatures and luminosities of the WD components of CVs are substantially higher than those of field WDs due to heating from accretion, and since accretion itself is a source of EUV and especially X-ray luminosity in Polars and IPs, the ROSAT mission has had a huge impact on the number of magnetic systems known to exist (Schwope et al., 2002; Jiang et al., 2000; Beuermann et al., 1999; Thomas et al., 1998). In fact the number of ROSAT-led CV discoveries have exceeded 100.

Hamburg Quasar Survey (*HQS*). The Hamburg Quasar survey was a wide-angled objective prism survey aimed at finding bright Quasars in the northern sky. The survey was carried out using the 80cm Schmidt telescope at Calar Alto (Spain), covering $\simeq$ 13 600 deg^2 of sky at $|b| > 20°$, $\delta > 0°$ with a limiting magnitude of B $\lesssim$ 17.5. The dynamic range of the survey is 13 $\lesssim$ B $\lesssim$ 17.5 (Hagen et al., 1995), with a spectral range of 3400 – 5400Å. Blue objects were classified after visual inspection into a small number of categories, mainly candidates for quasars, hot stars and narrow emission line objects (Hagen et al., 1999). Candidates from HQS were selected via the detection of Balmer emission lines and of blue colour plus variability. This has resulted in the identification of 53 new CVs with an intriguing result that nearly 54% of HQS novalike variables are SW Sex stars, with orbital periods in the 3-4hr range (Rodríguez-Gil et al., 2007a). This observation of such a large number of high mass transfer systems so close to the period gap is difficult to reconcile with the standard theory of CV evolution.

2.2.1 Sloan Digital Sky Survey (*SDSS*)

The Sloan Digital Sky Survey is carried out by a purpose-built 2.5m telescope at the Apache Point Observatory (APO); New Mexico. It has been designed to obtain deep ($g \approx 23$) photometric observations using a large mosaic CCD camera made up of 30 2048 $\times$ 2048 (13 $\times$ 13′) photometric CCDs (Lupton et al., 2001) capable of quasi-simultaneous imaging in five broad optical bands, *ugriz*, centred at effective wavelengths of 3500, 4800, 6250, 7700 and 9100Å respectively (Gunn et al., 1998; Fukugita et al., 1996).

SDSS is also designed to take spectroscopic observations of $> 10^6$ objects in $10^4 \mathrm{deg}^2$ of sky at $|b| > 30°$, to a limiting magnitude of $g \simeq 20$. This is achieved using 3° diameter spectrographic plates which hold 640 fibres leading to two 320-fibre-fed spectrographs (each with two 2048×2048 CCDs) with a range of $3900 - 6200$Å for the blue beam and $5800 - 9200$Å for the red beam with a resolving power of 1800, or $167 \mathrm{kms}^{-1}$ (York et al., 2000).

The main purpose of the SDSS is to accrue photometric and spectroscopic data on galaxies and QSOs. First the acquired data is reduced by a photometric pipeline (Lupton et al., 2001), which separates stars from galaxies, using their surface brightness distribution and computes magnitudes in the five *ugriz* colours. Objects are chosen for spectroscopic observations by a number of different selection algorithms (Stoughton et al., 2002). These algorithms cover colour loci of quasars (Richards et al., 2002), cool stars, white dwarfs, white dwarfs plus cool dwarf binaries. CVs are found serendipitously as their colours overlap with those of hot stars, quasars, WDs and M stars, depending on how much the accretion disc, or accretion column, contributes to the optical light over that of the underlying WD and late-type secondary star. Once spectra of target objects have been acquired, the data are wavelength- and flux- calibrated, and atmospheric disturbances are corrected using sdF stars. The resulting spectra are classified as stars, galaxies, or quasars, and redshifts are determined.

During the earliest stages of SDSS, a number of photometric selection criteria were attempted to try and maximise the chances of finding CVs (Szkody et al., 2002b). It was found that CVs easily separate from main-sequence stars in $u - g$ colour space but as previously mentioned overlap with quasars (Fan, 1999) and white dwarfs. The simultaneous red and blue colour selection criteria $u - g < 0.45$, $g - r < 0.7$, $r - i > 0.3$, $i - z > 0.4$ were used to select CVs with little disc contribution, however, the problem was that this was successful in identifying mostly non-interacting WD plus M dwarf binaries and only a few CVs. It was then decided by Szkody et al. that the most efficient way to detect CVs was to use the fact that since spectroscopic fibres were used to target candidate quasars and their colours overlapped with CVs (see Figure 2.3), a pipeline could be used to search through spectra of these candidate quasars to find CVs. Figure 2.3 shows the exclusion regions of the SDSS quasar target selection (light-blue shaded boxes), which was designed to limit contamination of the quasar search by white dwarfs, A-stars and white dwarf main sequence binaries (WDMS) (Richards et al., 2002). The black

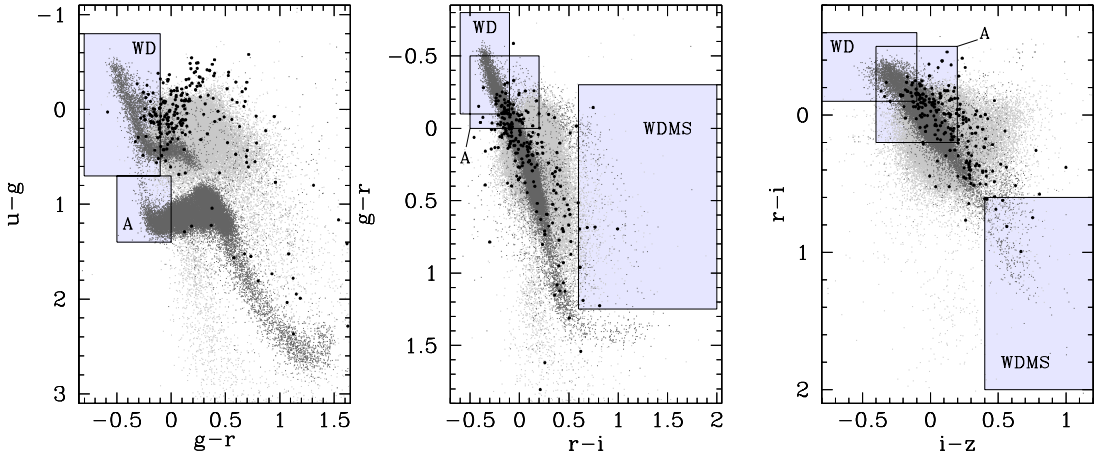

Figure 2.3: The panels show the location of stars and white dwarfs (dark grey), quasars (light grey) from SDSS in $u-g/g-r$, $g-r/r-i$ and $r-i/i-z$ colour-colour diagrams. The black dots are CVs. Shown as light-blue shaded boxes are the exclusions regions of the SDSS quasar target selection, designed to limit contamination by white dwarfs, A-stars and white dwarf main sequence binaries (WDMS).

dots represents all known CV identified by SDSS, 213 so far. On inspection, one may wonder as to why there are so many CVs within the exclusion regions. There are two reasons for this: Firstly, the implementation of the exclusion algorithms did not come into effect until after the first SDSS Data Release (DR1; July 2001) which resulted in the identification of the first CVs published in (Szkody et al., 2002b). Second, in addition to the exclusion boxes there are also two inclusion regions which overlap with the colour-cuts of the exclusion regions: (1) "mid-z", used to select $2.5 < z < 3$ quasars whose colours cross the stellar locus in SDSS colour space, and (2) "UVX", used to duplicate the selection of $z \lesssim 2.2$ UV-excess quasars. As a result, spectroscopic follow-up of some of these targets has led to the discovery of a number of CVs. Further details of these inclusion and exclusion boxes, and spectroscopic follow-up processes are discussed in (Richards et al., 2002).

CVs are formally identified in the SDSS spectra through an algorithm that selects objects with Balmer and helium emission/absorption lines at zero redshift (which typically implies ongoing accretion), and the resulting objects are then classified by eye. According to Szkody et al. (2007a) it is estimated that more than 90% of CVs that exist in the SDSS data base are found with a few missed through mis-identification or low S/N of spectra.

The features of SDSS mean that it is the most comprehensive method of CV detection to date. Its broad colour selection range gives it serious advantages over previous blue-only surveys like Palomar Green and Edinburgh Cape. Its deep magnitude limit will allow for the detection of intrinsically faint systems, with lower accretion rates out to many hundreds of parsecs above the Galactic plane, sampling several scale heights of the CV population.

A series of papers on CVs have been published annually; Szkody et al. 2002b, 2003a, 2004, 2005, 2006, 2007a, henceforth PSI–PSVI. At the time of writing, 213 CVs have been identified through SDSS, 177 of which are new discoveries (Szkody et al., 2007a). Of the systems for which orbital periods have been determined, approximately 70% have periods under 2hours, 10% are in the period gap (mostly Polars), and 20% are long-period systems above the period gap.

Chapter 3

Observations and Data Reduction

3.1 Observations and Data Reduction

In order to improve our understanding of CV evolution, it is imperative that we accrue a large, homogeneous sample of CVs with well determined parameters, which are representative of the intrinsic population of CVs. After initial identification of CVs by the SDSS, follow-up observations in the form of time-series photometry and spectroscopy have been undertaken in order to detect any photometric or spectroscopic variability associated with the orbital period of the binary and its CV sub-type.

The majority of observations in this thesis were carried out as part of the 2004/05 International Time Programme (ITP), at the Observatorio del Roques de los Muchachos at La Palma, with some additional data obtained at Calar Alto observatory at Almeria, Spain.

I have been on two scheduled runs as part of the ITP, during which I gathered both photometric and spectroscopic data: 30^{th} December 2004 - 8^{th} January 2005 at the Isaac Newton Telescope (INT), William Herschel Telescope (WHT) and Telescopio Nazionale Galileo (TNG), and 18^{th} - 25^{th} May 2005 once again at the INT.

This chapter includes a discussion of the basics of astronomical data reduction, tables and logs of all observations regarding CVs discussed in this work, and a discussion of time-series analysis used in the determination of orbital periods ($P_{\rm orb}$).

3.1.1 Photometry

Photometry concerns the measurement of flux or intensity of the electromagnetic radiation from an astronomical object over defined wavelength bands. *Absolute photometry* is the measurement of the apparent brightness of an object on a standard photometric system. This requires accurate calibrations and good stable atmospheric conditions. *Differential photometry*, or *time-series differential photometry*, as used for all observations discussed in this work, is the measurement of the changes in the brightness of a star relative to one or more comparison stars, which are assumed to be constant. These observations can be carried out in non-photometric conditions, as the target and comparison stars are in the same field of view, so are observed simultaneously under the same observing conditions. The measurements are then recorded and plotted as a function of time to produce a light-curve of the object.

3.1.2 Spectroscopy

Time-series spectroscopy is a very efficient means of deducing a number of physical parameters of cataclysmic variables, some of which cannot be determined from photometric observations alone. Orbital periods and estimates for radial velocities of stellar components can be determined by the measurement of the Doppler shifts of emission and absorption lines. With this information it is possible to estimate the masses, radii and temperatures of the WD and secondary, the spectral type of the secondary, as well as the distance to the system.

A typical astronomical spectrograph used for such observations consists of internal light sources used for flat-fielding and wavelength calibration, a slit placed at the focus of the telescope, a collimator that intercepts the divergent telescope beam, a dispersing element (a prism, grating, or grism) and a camera which focuses the dispersed light onto a CCD detector.

3.1.3 CCD Data Reduction

The recording of astronomical images is normally carried out using a CCD camera.

A CCD camera, or charge couple device, is a made from a silicon wafer, segmented into an array of individual light-sensitive cells or ‘pixels’. Photons impinging on the array create free electrons via the photoelectric effect. The electrons emitted in the CCD are fenced within

(a) Raw Image (b) Bias Image (c) Dark Image

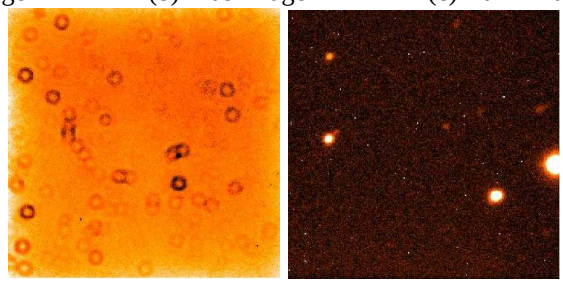

(d) Flat Image (e) Clean Image

Figure 3.1: Images above are 516 x 516 pixel CCD frames obtained from the Kryoneri 1.2m telescope (National Observatory of Athens). (a) Raw image contains the target object. (b). The bias frame is averaged from ten bias images. (c) Dark frame averaged from three dark frames with exposure times of 10 min. (d) Mean flat-field obtained from ten individual flat-field images. The artifacts in this image are due to dust/condensation on the CCD. (e) The final image, once bias-subtraction, dark-subtraction and flat-fielding have been carried out.

non-conductive boundaries, so they remain in the area of the photon strike. As long as light is allowed to continue to impinge on the pixel, the number of electrons within it will accumulate. Over time, exposure to photons produces an image made up of electrons on the CCD.

To read out an image captured on a CCD requires shifting the information out of the pixels to a read-out register. Photons are converted to a charge and finally to a voltage for measurement. An amplifier is then used to boost the signal to a useful level. Finally, the voltage is then converted to a digital count and fed into a computer to produce a two dimensional image.

Before astronomical data can be analysed, the data must be processed in order to optimise the signal-to-noise ratio, correct for instrumental artifacts and maximise the information within a photometric or spectroscopic frame. This is achieved by carrying out the following procedures; bias-subtraction, dark-subtraction and flat-fielding on a target frame/image and is referred to as data reduction. Figure 3.1 shows how a raw astronomical image is reduced to produce a clean target image using the processes described below.

Bias. This is a zero second exposure taken with the camera's shutter closed, or extracted from an overscan region - an area of the CCD not exposed to light. The response within the frame contains the signal from the readout noise which is generated when measuring the charge quantity in each pixel and an offset value in order to avoid negative values in the readout process. In practice a number of bias frames are taken and combined to produce a mean bias which is then subtracted from the target frame. This process is known as bias-subtraction and is the first stage of data reduction.

Dark Frame. A dark frame is acquired with the shutter closed. It contains information of the dark current in a CCD, created from the thermal generation of electrons which increases proportionally with time. As a result, the exposure time for a dark frame is the same as the target frame. As with bias frames, multiple dark frames are averaged together to produce a final dark calibration frame, which is then subtracted from the target frame. The overall effect of a dark current can be minimised by ensuring that the CCD is kept at a constant low temperature, and in fact many modern CCDs are cooled sufficiently, that the dark current becomes negligible and dark frames need not be taken.

Flat-field. Flat-fielding is a process used to ensure that any spatial (pixel-to-pixel) variation in the sensitivity of a detector, and effects from dust or vignetting, is accounted for. In order to achieve this, an image of a photometrically flat surface must be taken. This can be either a patch of uniformly illuminated area within the telescope dome or of a blank region of sky. Normally this is achieved at twilight when the sky is brighter than most stars which may be in the field of view. For spectroscopic observations, a series of flat-field spectra are usually obtained via illumination of a tungsten lamp located inside the spectrograph before the entrance slit. The exposure time must be adjusted in order to ensure that the image is not saturated. A series of flat-field images are taken in order to produce a normalised frame, by averaging a number of flat-field frames and dividing by the mean value. The target frame is then simply divided by this mean flat-field frame.

3.2 Telescopes and Instrumentation

The following Section provides a description of the telescopes, instruments and configurations used for observations presented in Chapters 4 and 5.

Isaac Newton Telescope (INT). Time-series photometric observations were carried out with the 'Wide Field Camera' (WFC): an optical mosaic camera used at the prime focus of the 2.5 m INT. It consists of four 2048×4100 pixel EEV CCDs with a $0.33''\text{pixel}^{-1}$ scale. Binning and windowing is not supported and hence the full area of all four CCDs has to be read out, which causes a dead time of 42 s between two exposures. We only reduced CCD4, which contains the target for all of our observations.

William Herschel Telescope (WHT). Time-resolved photometry was obtained with the 'Auxilliary Port Imaging Camera' (AUX Port) which was mounted at the Cassegrain auxiliary port of the 4.2 m WHT. It is equipped with a 1024×1024 pixel TEK CCD with a $0.11''\text{pixel}^{-1}$ scale and provides an unvignetted field of view of $\sim 1.8'$. We used the AUX Port with a binning 4×4, decreasing the read-out time of the full CCD to a few seconds. Time-resolved spectroscopy was achieved using the 2-arm spectrograph ISIS. On the blue arm the R600B grating was used in conjuction with the 4kx2k pixel EEV detector, covering the $3900 - 5400$Å wavelength range with a spectral resolution of $\simeq 2.0$Å. The R316R grating with the 4.5kx2k pixel Marconi detector was used on the red arm, covering $6100 - 8900$Å, with a spectral resolution of $\simeq 4$Å. A slit width of $1.2''$ was used.

Liverpool Telescope (LT). The LT is a fully robotic 2m telescope. Time-series photometry was acquired using the optical CCD camera RATCAM, equipped with a 2048×2048 pixel EEV with $0.14''\text{pixel}^{-1}$ scale covering a field of view of $4.6' \times 4.6'$. A binning 2×2 is the default for this instrument. Windowing is not supported, and the read-out time for the full CCD is 10 s.

Nordic Optical Telescope (NOT). The low-resolution imaging spectrograph ALFOSC on the 2.5 m NOT telescope contains a 2048×2048 pixel EEV CCD with an $0.19''\text{pixel}^{-1}$ scale. Time-series photometric data were obtained by binning the CCD 2×2 and windowing around the target star, reducing the read-out time to a few seconds. Time-series spec-

troscopic observations were obtained using grism #7 with a 1.2″ slit width providing a spectral resolution of 3Å. The sampled wavelength range is between 3800 – 6800Å.

Telescopio Nazionale Galileo (TNG). The Device Optimized for the Low-Resolution (DOLORES) on the 3.6 m TNG was used for time-series photometry. A 2048×2048 Loral CCD with a $0.28''\text{pixel}^{-1}$ scale, covers a field of view of about $9.4' \times 9.4'$. The CCD was not binned, but was windowed in order to reduce readout time to $\sim$ 10 s. Time-resolved spectroscopy was carried out using the HR-V grating. 2×2 binning was implemented on the CCD and a slit width of 1″ was used. The wavelength range covered was 4650Å – 7000Å with a spectral resolution of $\simeq 4$Å.

Calar Alto (CA22). The Calar Alto Faint Object Spectrograph (CAFOS) was used on the 2.2 m telescope. Used for time-series photometry, the instrument is equipped with a 2048×2048 SITe CCD with a scale of $0.53''\text{pixel}^{-1}$ and a field of view of $16'$. Windowing was applied to reduce the readout time to $\sim$ 10 s.

3.3 Log of Observations/Summary of System Properties

The following pages show tables which include information of observations taken of SDSS CVs, including details of the observational properties of systems as determined through analysis of photometric and/or spectroscopic data; such as orbital period, apparent magnitude, and CV subtype. In addition the 'source' for each system has been added i.e. which paper the identification details of each system was first published. Szkody et al. 2002b, 2003a, 2004, 2005, 2006, 2007a also referred to as PSI–PSVI as stated in Chapter 2.

CVs selected for follow-up observations are done so by taking into consideration a number of factors such as, the time of year – which effects whether or not a system is available for observation and the length of time it can be observed, weather conditions, lunar cycles, and the object's apparent magnitude. Whilst all these factors can effect the types of observation which can be carried out i.e. time-series photometric or spectroscopic, the availability and limitations of instruments also effects the types of object one may wish to observe. An obvious constraint is the aperture of the telescope which determines the magnitude limit. Another is that for spec-

troscopic observations, the target needs to be brighter than a photometric target as a higher signal-to-noise ratio is required. This can be proven by comparing the average *g*-magnitude of the two samples discussed in this thesis. For the photometric sample (Table 3.1) discussed in Chapter 4, $< g_{phot} >= 19.14$ and the mainly spectroscopic sample (Table 3.2) discussed in Chapter 5, $< g_{spec} >= 18.26$. The average magnitude of the mainly spectroscopic sample is 0.88 magnitude brighter than the photometric sample. A table comparing the properties of the two samples is given in Table 5.3.

In order to accrue viable data, the aim is to maximise on the number of counts that can be detected from a star, and invariably, conditions tend to lead towards the targeting of brighter objects over fainter ones.

The aim of the ITP was to follow-up as many objects as possible and determine their orbital parameters. A list of possible candidates for both spectroscopic and photometric observations are drawn up based on the afore mentioned criteria. One can see that impromptu choices based on adverse changes in observing conditions are likely to lead to a bias towards brighter systems, which are either bright as they are close by, or due to their inherently high mass transfer rates – which would culminate in a sample of CVs with long orbital periods. The only way to get rid of this problem is by carrying out observations of all CVs within the SDSS database, or at least to a certain limiting magnitude, so that biases are removed from the follow-up process. A further detailed discussion is given in Section 7.3 of the 'Future Work' section of this thesis.

It should be mentioned at this point that a number of observations were acquired by amateur astronomers for SDSS J0901+4809 and SDSS J1250+6655, the details of which are highlighted in Table 3.1. Below are details of the instrumentation and configurations, provided by the amateur astronomers.

Hankasalmi Observatory (HaO). Observations were carried out by A. Oksanen in New Mexico. A RCOS Carbon 16RC 0.40 m Ritchey-Chretien telescope mounted on a Paramount ME, along with an SBIG STL-1001E CCD camera. The data were dark subtracted and flat fielded and measured using aperture photometry with the MaxImDL software.

Astrokolkhoz Observatory (AO). Observations were carried out by T. Krajci in Finland. A 0.28 m Schmidt-Cassegrain telescope with a focal length of 1.8 m along with an SBIG ST-

7 CCD camera binned 2×2. The data were dark and bias-subtracted, and flat fielded and measured using aperture photometry with AIP4WIN.

Hudson Observatory (HO). Observations were carried out by S. Brady from a private observatory located in southern New Hamphsire, USA. Instruments include a 0.4m robotic Newtonian Telescope mounted on a Paramount ME along with an SBIG ST-8XME CCD camera, and BVRI filters (which were not utilised due to the faint magnitude). The robotic system was programmed to monitor a list of poorly studied CV candidates and to initiate immediate time-series observations if an outburst was detected, as was the case with SDSS J0901+4809 and SDSS J1250+6655. All images were bias subtracted, flat-field corrected and photometrically reduced using MaxIm DL.

Table 3.1: Log of Observations for Chapter 4: Photometric Observations.

SDSSJ	Porb [min]	SDSS g	mag	Type	Date/Time [UT]	Telescope	Filter	Exp(s).	Frames	Source	Observor
001856.93+345444.3	-	17.8	17.2	He II/RD	2005-01-01 20:55-23:46	INT	clear	25	153	PSIV	AA,MD
			17.8		2005-01-05 19:50-23:01	TNG	clear	40	176		TM
			17.5		2005-01-06 19:35-23:17	TNG	clear	30	321		“
			17.7		2005-01-07 19:29-22:48	TNG	clear	30	275		“
002728.01-010828.5	85.44 ± 0.07	20.7	20.6	DN/WD	2004-12-31 20:08-22:55	WHT	*V*	40-100	215	PSIV	SB,TM
			20.6		2005-01-01 19:49-22:44	WHT	*V*	40	233		“
			20.6		2005-01-02 19:35-22:29	WHT	*V*	40	231		“
015151.87+140047.2	118.68 ± 0.04	20.3	19.9	DN/RD	2004-08-15 02:47-05:39	INT	*g*	40	129	PSI	AA
			19.9		2004-08-16 01:35-05:50	INT	*g*	40-60	169		“
			19.9		2004-08-17 01:58-05:30	INT	*g*	40-60	148		“
074813.54+290509.2	-	18.6	19.2	He II	2004-09-12 04:57-05:53	LT	*g*	60	50	PSIII	Robotic
082409.73+493124.4	95 ± 3	19.3	21.0	DN	2005-01-04 23:06-03:56	WHT	*V*	20	698	PSI	TM,SB
			20.8		2005-01-05 21:00-04:56	WHT	*V*	30	380		“
			21.0		2005-01-07 00:37-04:24	WHT	*V*	20-30	532		“
085414.02+390537.3	113.26 ± 0.03	19.2	19.2	AM	2005-01-03 00:07-07:13	INT	*g*	80-120	112	PSIV	AA,MD
			19.5		2005-01-03 23:47-07:13	INT	*g*	50-60	303		“
090103.93+480911.1	112.14793	19.9	19.5	DN/RD/EC	2006-02-06 23:08-04:27	CA22	clear	60	240	PSIV	Service
	±0.00005		16.2		2007-10-06 06:52-09:39	HO*	clear	160	52		SBr
			17.0		2007-10-09 08:38-12:12	AO*	clear	60	192		TK
			17.1		2007-10-09 20:42-00:22	HaO*	clear	95	128		AO
			18.1		2007-10-11 08:10-12:09	AO*	clear	90	138		TK
090452.09+440255.4	-	19.4	19.6	WD	2005-01-05 02:33-04:06	INT	*g*	30-40	73	PSIII	AA,MD
			19.1		2005-01-05 04:10-06:55	INT	clear	30-35	143		“
			19.6		2005-02-02 23:30-02:00	NOT	clear	15	544		PR,MJA
091945.11+085710.0	81.6 ± 1.2	19.9	18.9	WD	2006-01-24 03:17-06:14	CA22	clear	25	252	PSIV	AA
124426.26+613514.6	142.9 ± 0.2	18.8	18.6	He II	2005-05-18 21:37-02:20	INT	*g*	40-60	215	PSIII	BG,MD
			18.4		2005-05-19 21:03-00:29	INT	*g*	40	160		”
			18.7		2005-05-20 21:02-00:05	INT	*g*	40-60	123		”
12503.85+665525.5	84.5793893	18.7	19.1	DN/EC	2005-02-03 04:19-05:38	NOT	clear	15-30	151	PSII	PR,MJA
	±0.0000036		19.3		2005-02-05 01:14-05:19	NOT	clear	10-20	451		“
			19.0		2005-03-16 03:15-06:42	LT	*g*	60	169		Robotic
			19.1		2005-03-17 23:19-23:47	LT	*g*	60	33		“
			19.0		2005-03-18 01:13-03:14	LT	*g*	60	166		“
			16.0		2008-01-29 01:36-08:52	HO	clear	70	306		
			16.4		2008-01-31 01:18-10:40	HO	clear	120	231		
			16.6		2008-02-04 03:32-08:06	HO	clear	160	93		

...continued on next page

Table 3.1 continued.

SDSSJ	Porb [min]	SDSS g	mag	Type	Date/Time [UT]	Telescope	Filter	Exp(s).	Frames	Source	Observer
151413.72+454911.9	-	19.7	20.1	WD	2005-04-01 04:11-06:29	LT	*g*	60	114	PSIV	Robotic
			20.1		2005-05-10 01:30-05:35	LT	*g*	60	205		“
171145.08+301320.0	80.35 ± 0.05	20.3	20.2	WD	2004-08-14 21:15-01:03	INT	*g*	40-60	141	PSIII	AA
			20.2		2004-08-15 21:05-00:13	INT	*g*	40-60	129		“
			20.2		2004-08-16 21:05-23:46	INT	*g*	45-120	63		“
			20.3		2005-08-11 21:28-00:04	NOT	clear	40	198		BG
			20.3		2005-08-12 21:11-22:30	NOT	clear	40	101		“
211605.43+113407.5	80.2 ± 2.2	15.3	22.1	DN	2005-08-09 00:54-03:59	NOT	clear	60	164	PSIII	BG
			22.1		2005-08-10 00:40-02:24	NOT	clear	60	93		“
			22.1		2005-08-11 02:40-04:33	NOT	clear	90	70		“
			18.8		2005-08-24 23:12-02:08	LT	*g*	90	110		Robotic
215411.12-090121.6	319 ± 0.7	19.2	20.4		2005-08-11 00:29-05:42	NOT	W	40	396	PSII	BG
			20.3		2005-08-12 22:33-04:11	NOT	W	40	427		“
			20.4		2005-08-14 00:33-05:38	NOT	W	40	376		“

∗ indicate observations taken by amateur astronomers. (SBr; S. Brady, TK; T. Krajci, AO; A. Oksanen)

Log/summary of photometric observations and summary of systems properties. Given are the orbital periods as determined from photometric time-series, the *g* magnitude from the SDSS imaging data, the magnitude during our observations, information on system (WD = white dwarf dominated spectrum, RD = secondary star is visible, He II = noticeable He line, EC = eclipsing, DN = dwarf nova, AM = polar), Observers: (AA; Amornrat Aungwerojwit, BG; Boris Gänsicke, MD; Monihar Dillon, MJA; Maria Jesús Arévalo, PR; Pablo Rodríguez-Gil, SB; Susana Barros, TM; Tom Marsh), Telescope (CA22; Calar Alto; INT; Isaac Newton Telescope, LT; Liverpool Telescope, NOT; Nordic Optical Telescope, TNG; Telescopio Nazionale Galileo, WHT; William Herschel Telescope, HaO; Hankasalmi Observatory, AO; Astrokolkhoz, HO; Hudson Observatory)

Table 3.2: Log of Observations for Chapter 5: Photometric and Spectroscopic Observations.

SDSSJ	Porb[min]	SDSS g mag	Type	Date/Time [UT]	Telescope	Filter/Grating	Exp(s)	Frames	Source (PS)	Observer
080215.38+401047.1	221.62 ± 0.04	16.69	NL	2004-11-05 04:23-06:07	NOT (s)	grism #7	600	11	PSII	PR
				2004-11-06 01:16-06:22	NOT (s)	grism #7	600	28		”
				2004-12-05 03:14-06:54	NOT (s)	grism #7	600	21		”
080846.19+313105.9	296.45 ± 0.75	19.43	DN	2004-12-31 23:58-05:28	WHT(s)	R600B,R316R	1200-1500	16	PSIII	AA,MD,SB,TM
				2004-10-26 02:20-06:38	LT (p)	*g*	60	223		Robotic
				2004-12-07 23:49-02:11	LT (p)	*g*	60	122		“
				2004-12-08 23:28-04:19	LT (p)	*g*	60	254		“
090350.73+330036.1	85.22 ± 0.14	18.84	Eclipse	2005-01-03 00:32-06:49	WHT (s)	R600B,R316R	24	900	PSIV	AA,MD,SB,TM
				2005-01-04 01:01-03:42	WHT (s)	R600B,R316R	16	600		“
				2005-01-01 00:14-07:11	INT (p)	clear	309	30		AA,MD
093249.56+472523	95.475 ± 0.0001	17.81	Eclipse/He II	2005-01-08 00:17-02:26	WHT (s)	R600B,R316R	18	400-600	PSIII	AA,MD,SB,TM
				2005-01-08 03:01-07:06	TNG (p)	clear	323	30		TM
124959.75+035726.6	–	16.63	WD/RD	2005-01-01 05:53-06:47	WHT (s)	R600B,R316R	6	600	PSIII	AA,MD,SB,TM
145758.21+514807.9	–	19.52	WD	2005-05-11 21:21-00:25	NOT (s)	grism #7	18	600	PSIV	PR
				2005-06-05 23:01-04:07	LT (p)	*g*	240	60		Robotic
				2005-05-10 22:25-04:20	NOT (p)	clear	1153	10		PR
				2005-05-12 00:40-05:23	NOT (p)	clear	411	30		PR
153817.33+512338	93.11 ± 0.09	18.61		2005-04-30 03:04-05:23	TNG (s)	HR-V	9	900	PSIII	DM
				2005-05-01 22.32-05:30	TNG (s)	HR-V	22	900		“
161030.34+445901.7	–	19.81	WD	2005-07-10 22:28-01:28	WHT (s)	R600B,R316R	17	600	PSIII	BG,PS
				2005-07-12 01:07-02:57	WHT (s)	R600B,R316R	11	600		“
170324.08+320953.1	–	18.17	RD	2004-08-19 21:39-00:18	TNG (s)	HR-V	18	500	PSIII	PG
				2004-08-20 21:11-23:47	TNG (s)	HR-V	18	500		”
				2004-08-22 21:01-23:40	TNG (s)	HR-V	17	500		”
				2005-07-11 02:09-02:50	WHT (s)	R600B,R316R	5	600		BG,PS
				2004-08-16 23:31-00:58	INT (p)	clear	41	40		AA
204817.84-061044.8	87.49 ± 0.32	19.35	WD	2005-07-10 01:04-04:49	WHT (s)	R600B,R316R	20	600	PSII	BG,PS
				2005-07-11 03:12-05:08	WHT (s)	R600B,R316R	11	600		“

...continued on next page

Table 3.2 continued.

SDSSJ	Porb[min]	SDSS g mag	Type	Date/Time [UT]	Telescope	Filter	Exp(s)	Frames	Source (PS)	Observer
210131.26+105251.5	–	18.08	He II	2004-08-21 22:16-02:19	TNG (s)	HR-V	23	500	PSII	PG
				2004-08-23 00:57-04:10	TNG (s)	HR-V	19	500		“
				2005-07-11 01:48	WHT (s)	R600B,R316R	1	600		BG,PS
				2005-07-13 22:32-05:14	WHT (s)	R600B,R316R	37	600		“
223439.92+004127.2	127.29 ± 0.25	18.10	DN	2004-08-20 01:02-05:31	TNG (s)	HR-V	36	400	PSII	PG
				2004-08-21 00:31-05:46	TNG (s)	HR-V	43	400		“
225831.17-094931.6	119.45 ± 3.92	15.61	DN	2004-08-22 02:45-05:42	TNG (s)	HR-V	53	180	PSII	“
				2004-08-23 04:38-05:52	TNG (s)	HR-V	12	180		“
				2004-11-03 20:55-01:04	NOT (s)	grism #7	45	300		PR
				2004-11-04 23:23-00:43	NOT (s)	grism #7	12	300		“
				2004-11-05 19:53-00:42	NOT (*s)	grism #7	53	300		“
230351.63+010651.1	110.51 ± 0.24	19.05	DN/RD	2005-07-12 03:18-05:20	WHT (s)	R600B,R316R	12	600	PSI	BG,PS
				2005-07-13 01:55-05:19	WHT (s)	R600B,R316R	19	600		“

Log of photometric and spectroscopic observations and summary of systems properties. Observers: AA; Amornrat Aungwerojwit, BG; Boris Gänsicke, DM; Domitilla de Martino, MD; Monihar Dillon, PG; Paul Groot, PR; Pablo Rodríquez-Gil, PS; Paula Szkody, SB; Susana Barros, TM; Tom Marsh. Information on system: s = spectroscopic data, p = photometric data, * = system in outburst, WD = white dwarf dominated spectrum, RD = secondary star is visible, He II = noticeable He line, EC = eclipsing, DN = dwarf nova, AM = polar

3.4 Time-Series Analysis

Time-series analysis is the application of mathematical and statistical processes in which time-varying data is replicated or 'transformed' from the time domain to the frequency domain, to produce a power spectrum or a periodogram. This technique is not unique to astronomy and is used not only to quantify the variation being analysed, but to possibly to constrain it, or gain some understanding of the physical processes which caused it.

In order to determine an orbital period for a CV, or indeed detect any periodic signature from photometric or spectroscopic data, it is necessary to perform time-series analysis.

There are a number of different types of time-series analysis. The methods in the scope of this thesis are Fourier type analysis and phase-folding/analysis-of-variance type procedures which are most appropriate for studying astronomical data, and are amongst the most commonly used.

3.4.1 Fourier Analysis and Acquisition of Data

In accordance with Fourier's theorem, any continuous time-varying signal can be expressed as a series of sine and cosines (Fourier series) of varying frequencies. Each sinusoid has specific amplitude and phase coefficients (Fourier coefficients) which are determined by the relative contribution to the observed time-varying signal.

Fourier transforms are used to transform the time-varying data, from the time domain to the frequency domain. The result is a plot of the amplitude squared versus the frequency to produce a power spectrum or periodogram.

Consider a simple case of an infinitely long signal composed of a sine wave. The corresponding power spectrum will consist of a single peak in the form of a δ – function at the frequency of variability. Complex waves – such as the canonical example of the square wave – can be recreated by first taking a sine with a frequency corresponding to the period of the system (fundamental frequency) then adding sines which are multiples of that frequency (harmonics). The subsequent power spectrum will be composed of a series of peaks at frequencies corresponding to the sines used to compose the square wave, i.e. the fundamental and harmonics. For a signal which is composed of several signals, the power spectrum will resolve this variability

into different peaks corresponding to the different signals.

In astronomy, there are a number of practical issues which affect the data which are used for time-series analysis, which in turn affects the type and method of time-series analysis which is used. One such problem is the sampling rate.

A lightcurve is limited by the rate at which it is sampled. Periodicities faster than this are not recoverable. The sampling theorem states that, in order for a perfect reconstruction of a signal, the sampling frequency (f_s) must exceed twice that of the maximum frequency (f_{max}), of the intrinsic variability being sampled i.e. $f_s > 2 \cdot f_{max}$. The frequency $2 \cdot f_{max}$ is known as the Nyquist sampling rate. Half of this value (f_{max}) is known as the Nyquist frequency and represents an upper limit on the frequencies which one can search for in a given data set with some sampling rate. When the sampling rate is not high enough, aliasing can occur in the periodogram. The effect of aliasing is caused when components of frequencies greater than the Nyquist frequency are reconstructed as components of the signal below the Nyquist frequency. Fortunately, though, aliasing of higher frequencies is not a problem in determining orbital periods for CVs as the frequencies of variability corresponding to the orbital period is much lower than the sampling rate.

An additional problem to that of the sampling rate is the length of observations, or more specifically the number of cycles which are covered during observations. The frequency resolution of the data is directly proportional to the inverse of the data length $\Delta f = 1/\Delta t$. Thus a long dataset will produce a narrow peak in the transform whilst a short train will produce a broader peak. The shorter the dataset, the less accurately a period can be determined.

Another important issue in the context of astronomy is that the time series photometric or spectroscopic data are always unevenly sampled. These gaps can be the result of clouds or bad seeing and, of course, due to daylight. The implication of this is that it is very possible that the amount of data either side of the data gap may not be sufficient to determine with enough accuracy the number of orbital cycles that may have occurred between one observation and the next. This leads to a phenomenon known as *cycle ambiguity* and leads to the issue of aliasing. This is where several peaks appear in the periodogram alongside the 'real' peak corresponding to the true orbital period. The alias peaks are separated from the true frequency by integer multiples of the frequency of observations, i.e. observations carried out every night are separated by $1\mathrm{d}^{-1}$.

If the true period is short compared to the frequency of observations, and the data are obtained just with regular sampling, the power spectrum will contain several alias peaks with similar statistical significance regardless of how much data are accumulated. However uneven sampling can reduce the power of the $1d^{-1}$, if greater portions of a cycle, or number of cycles can be covered and the frequency of observations can be increased, whilst the opposite can result in an increase in the complexity of the aliasing pattern.

3.5 MIDAS Utilities for Time-Series Analysis

The ESO-MIDAS system [1] is a tool for processing astronomical images and data reduction created by ESO (European Southern Observatory). It includes special packages for use with data taken from ESO instrumentation at La Silla and the VLT (Very Large Telescope) at Paranal and contains generic applications for photometry, image deconvolution and decomposition, and statistics.

There are several methods of time-series analysis implemented in the MIDAS/TSA context written by Schwarzenberg-Czerny for the analysis of unevenly sampled data. These fall into two principal categories; Fourier type methods and phase folding/analysis of variance procedures, both of which transform the observed data from the time-series domain into the frequency domain to produce a power spectrum or periodogram.

3.5.1 Fourier Type Methods

Fourier analysis methods involve decomposing a signal into a series of sines and cosines, via a Fourier transform (a generalised form is given below) which effectively converts data from the time domain into the frequency domain. Fourier analysis is useful for the detection of weak, periodic sinusoidal/quasi-sinusoidal signals with smooth variations. The following integration is performed on each measurement in the light curve.

$$F(\nu) = \int f(t)e^{i2\pi\nu t}dt$$

[1] http://www.eso.org/sci/data-processing/software/esomidas

where f(t) is the data in the time domain, $F(\nu)$ is the data in the frequency domain, ν is the frequency and dt is the time interval between data points. The complex exponential function in the integral is a complex sum of sine and cosine terms. For a given test frequency, each measurement in time is multiplied by this function and the time difference between each point (dt) and then summed over all measurements, to produce one data point in the power spectrum. The integration is then performed for all test frequencies to obtain the complete power spectrum.

The range of periods which are tested for are constrained by the length and sampling rate of the data set, which place limits on the resolution of the period search as discussed in Section 3.4.1. Two Fourier-type methods are implemented in the `TSA` context:

- `POWER/TSA`. This is simply the discrete classical Fourier transform (FT). The original classical FT concerns transforming a mathematical function into Fourier space whereas the discrete FT is a modified version which transforms discrete, unevenly sampled data into Fourier space. `POWER` computes a discrete power spectrum for unevenly sampled data by a slow method. This means that the number of computations carried out for N data points is proportionally to N^2 whereas the fast method is proportional to $Nlog_2N$. Whilst this method represents the most simple and straightforward method of time-series analysis, the power spectrum has no well defined statistical properties. As a result it is used only as a means of ascertaining variations in the spectral window.

- `SCARGLE/TSA`. Based on Scargle's (1982) method. A periodogram is computed for unevenly sampled data by a slow method. The `scargle` statistic uses a pure sine model and is a special case of the power spectrum normalised to the variance of the raw data. The purpose of this modification of the classical power spectrum (as described above), is to add statistical significance to the spectral features within the periodogram, allowing the observer to identify real periodic signals amongst the spurious spectral peaks created by noise. The resulting `scargle` periodogram is relatively similar to the original periodogram even though computational details differ. This explains the striking similarity between the `POWER` and `scargle` periodograms shown for SDSS J0854+3905 and SDSS J1244+6135 as shown in Figures 3.2 and 3.3.

3.5.2 Phase-Folding/Analysis of Variance Methods

Such methods involve folding the light curve over a set of test periods, then binning the data and analysing the statistical significance of the deviation of the binned data from a constant value. To elaborate, consider the case where a light curve containing a periodic signal is folded over the correct period; the phase folded light curve will show a strong correlation between the flux and the phase. The light curve is then binned. The variance of the mean value of each bin is calculated across the whole phase folded light curve, i.e. across all bins. In the above case the variance will be large as the phase folded lightcurve will display a clear structure. In the case of folding at a period unrelated to the real period, the variance across the phase folded lightcurve will be small, as the mean value within each bin will be similar between bins; there will be no correlation between the flux and phase. In these techniques it can be seen that the variance is representative of the power at that folded period.

These methods are aptly suited for determining features in light curves with sharp variations such as eclipses. However one side effect of these methods is that they can produce signals/power at the sub harmonics of the strongest signal. The power appears at timescales related to the period; integer multiples of the period (P) and fractions: $n \times P$ and $\frac{P}{n}$ where n is an integer (Schwarzenberg-Czerny, 1989).

- `AOV/TSA`. Schwarzenberg-Czerny (1989)'s method. As described above, the data are folded over a set of trial periods and the variance is computed from the resulting phase-binned light curve, the greatest variance corresponding to the most likely period. As this method is sensitive to detect sharp variations, such as eclipses, using phase bins of width comparable to that of these features will boost the sensitivity above that attainable with the Scargle method.

- `ORT/TSA`. Schwarzenberg-Czerny's (1996) extension of `aov`. The light curve is fitted with a multi-harmonic Fourier series using an efficient algorithm employing orthogonal multi-harmonic sine waves. The `aov` analysis is then applied to this fit, as opposed to the original data. The result is a smoother power spectrum than produced by `aov`. The technique improves the sensitivity of period detections and dampens the alias periods, allowing successful time-series analysis of data with relatively low S/N. The `ort` method

has the advantages of being sensitive to both sinusoidal and sharp and rapid variations from pulsating and/or eclipsing sources. Using harmonics of width comparable to that of sharp or rapidly varying features will boost sensitivity above that attainable with the Scargle method.

The following pages show a sample lightcurves of two systems SDSS J0854+3905 (Figure 3.2) and SDSS J1244+6135 (Figure 3.3), which are discussed in further detail in Chapter 4. I have provided the periodograms calculated from the four techniques to emphasis the differences between them. It can be seen that for SDSS J0854+3905 which is a lightcurve displaying non-sinusoidal variations, the phase-folding methods of `aov` and `ort` are much better suited to providing a better resolved periodogram than the Fourier type methods of `scargle`. For SDSS J1244+6135, a lightcurve displaying much more of a sinusoidal variation, the Fourier type method of `scargle` provides a much 'cleaner' periodogram without the peaks corresponding to power at the lower frequencies which are a side-effect of the phase folding techniques of `ort` and `aov`.

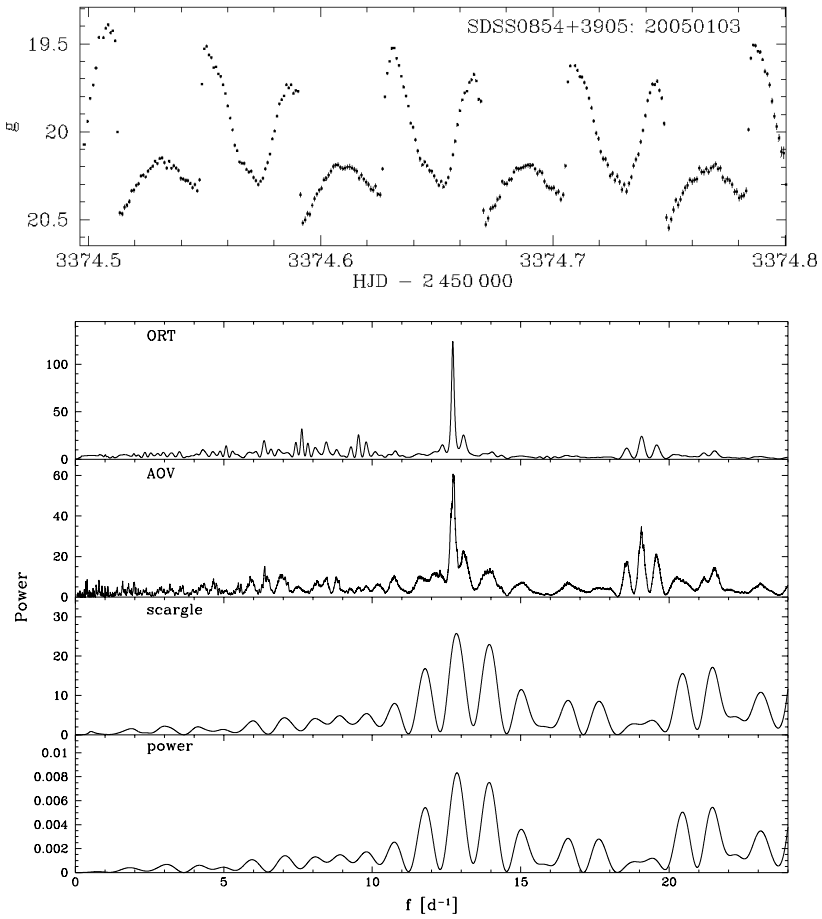

Figure 3.2: *Top plot*: the highly modulated lightcurve of SDSS J0854+3905. *Bottom plot*: composed of four periodograms computed from two nights of observations. The `ort` and `aov` periodograms are the phase folded methods, produce better resolved periodograms due to the greater sensitivity to the non-sinusoidal variations compared to Fourier type periodograms of `scargle` and `power`.

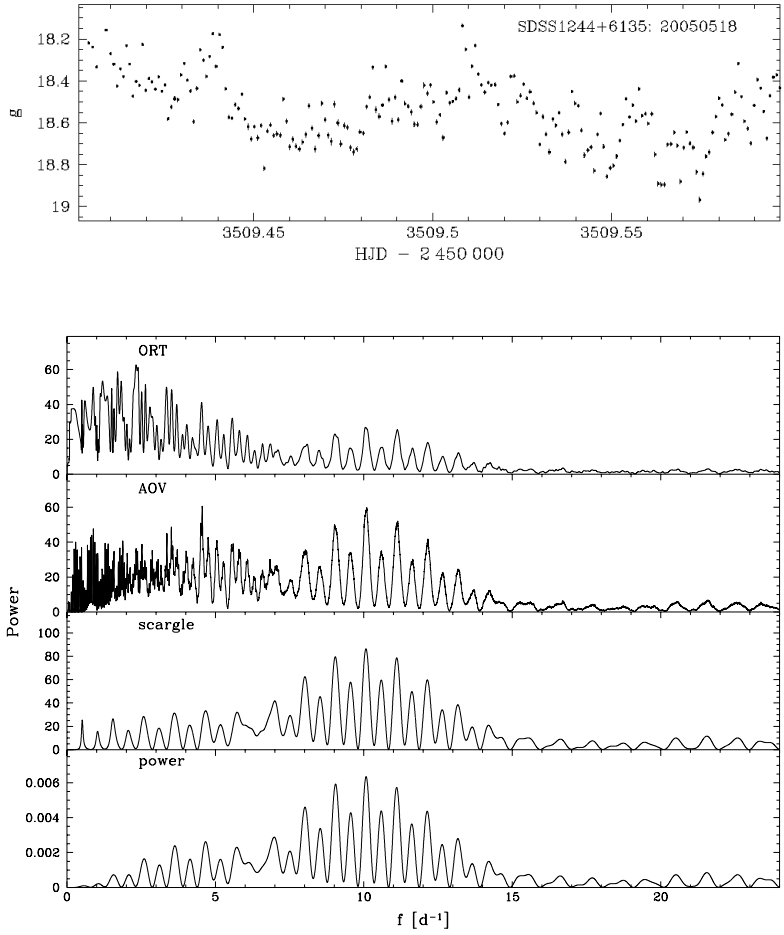

Figure 3.3: *Top plot*: the lightcurve of SDSS J1244+6135. *Bottom plot*: the four periodograms computed from the three nights of observations. The more sinusoidal variation of lightcurve of this system lends itself to better analysis using `scargle`. The stronger peaks at lower frequencies in the `ort` and `aov` periodograms result from the sub-harmonics of the orbital frequency, which these two methods of time-series analysis are sensitive to.

3.6 Analysis of Photometric Data

Photometric data reduction was carried out using the pipeline described by Gänsicke et al. (2004), which employs `MIDAS` for bias, dark-subtraction and flat-fielding, and aperture photometry for all objects in the field of view using `SExtractor` (Bertin & Arnouts, 1996). Differential magnitudes were measured relative to a comparison star close to each target object and converted to apparent magnitudes using the *g'* magnitude of the comparison star obtained from the SDSS. While data obtained in the V-band can be calibrated using the colour transformations available on the SDSS website, some systematic uncertainty of the apparent magnitudes of the systems observed in white light or with a non-standard filter remains.

Details pertaining to the acquisition of data, instrumental configuration and reduction of data have already been discussed in this chapter. Three of the time-series analysis methods provided in the `MIDAS/TSA` context (`scargle`, `ort` and `aov`) were used to calculate periodograms for each individual lightcurve, as well as for each system combining all available data. All light curves had their nightly mean subtracted before the analysis. Where the time-series analysis revealed the presence of a periodic signal in the photometric data, these signals were interpreted as the orbital periods of the systems. The periodograms calculated for those objects from their combined photometric data sets are shown in Figure 4.2 and Figure 5.3, along with phase-folded light curves.

For eclipsing systems (see Table 3.1 and Table 3.2), while the above methods were carried out for completeness, more accurate orbital periods can be determined from the analysis of the mid-eclipse times. In order to measure those times (Table 4.1 and Table 5.1) the original lightcurve was plotted with a copy mirrored in time. The copy was shifted until the bottom of the eclipse in both light curves showed the closest agreement, which was determined by eye. Orbital phases are then computed for the mid-eclipse times for a set of test periods. The most likely period (and cycle count) is determined by the minimum difference. The periodogram for eclipsing systems is thus $(\phi_0^{\rm fit} - \phi_0^{\rm observed})^{-2}$ vs frequency. Next a least-squares fits to the mid-eclipse times versus the cycle count number is done, which provides the coefficients for the eclipse ephemeris (as shown in the form below) as well as the errors on the zero point and on the period (see Tables 4.1 and 5.1).

$$\mathrm{HJD}(\Phi = 0) = \mathrm{ZERO} + \mathrm{E} * \mathrm{PERIOD}$$

The periods and errors reported in Table 3.1 and Table 3.2 were determined using the `SINEFIT/TSA` context. The utility in `MIDAS` carries out a least-squares sine wave fitting found by minimising the χ^2. The error on the period is derived by considering the pertubation necessary to increase χ^2 by 1, i.e. $\chi^2 - \chi^2_{min} = \Delta\chi^2 = 1$. The difference between the perturbed and best fitting (minimum) values of the parameter gave the relevant 1σ error (Press et al., 1992). `SINEFIT/TSA` is also used to remove a trend or to detrend data. This is a process by which fixed frequencies are manually removed from observations by fitting a sine of a desired frequency to the observations and subtracting the oscillation. The remaining residuals can be analysed again using any desired method of time-series analysis available in the `TSA` context within `MIDAS`.

All times and dates are given on the UTC (Universal Timescale Co-ordinated) time system (including leap seconds).

3.7 Analysis of Spectroscopic Data

The reduction of the spectroscopic data was carried out by P.Rodríguez-Gil and consisted of de–biasing, flat–fielding, optimal extraction and wavelength and flux calibration, using `IRAF` as well as the `PAMELA` and `MOLLY` codes created by Marsh (1989).

For spectroscopic data (see Chapter 5), radial velocities were determined from the hydrogen emission lines in the spectra of the targets by cross-correlation against single and double Gaussian functions, using the `MOLLY` code. The single-Gaussian method is sensitive to the peak of the emission line, which represents the motion of features at the outer regions/edge of the accretion disc (such as the bright spot). The double-Gaussian method (Schneider & Young, 1980) can be used to measure the wings of the emission lines, the flux of which originates from material close to the inner regions of the accretion disc which is often interpreted as representing the motion of the white dwarf.

A variety of values for the full width at half maximum (FWHM) for the single Gaussian method were used. For the double-Gaussian technique, results for a variety of FWHMs and separations between the two Gaussians were calculated, in order to confirm the robustness of the

results. The choice of single or double-Gaussian methods were dependent on the line profile. Single or a double Gaussian fits were practical for lines displaying a single line profile. Both methods were carried out for comparison to see which was most sensitive for determining the motion in the spectral lines. However, double-Gaussian fits are better suited for radial velocity measurements for lines displaying a double peaked profile, this is due to a lack of a singular central peak to cross-correlate a single-Gaussian against.

The measured radial velocities for each CV were searched for periods using the methods provided by the `MIDAS/TSA` context, as discussed in Section 3.5.

3.8 Bootstrapping

In order to assess the likelihood that the strongest peak represents the true orbital period in a periodogram, for systems with ambiguous orbital periods, a test based on bootstrapping simulations was applied (see Press et al. 1992, section 15.6), following the approach described in Southworth et al. (2006, 2007b).

Bootstrapping has also been referred to as the 'quick-and-dirty Monte-Carlo' technique, and is used when there is insufficient information on the nature of the errors within a data set to do a true Monte-Carlo simulation. The method provides a quick estimate of the bias, variation and errors within a simulated data set by using the actual data set D_0 with its N points to simulate any number of new data sets $D_1, D_2, ...$, also with N data points. The procedure draws N points at a time with replacement from the set D_0. Due to the replacement process the original data set is not returned but a simulated data set with random fraction of the original points ($\sim 1/e \approx 37\%$; see Press et al. 1992). These sets are then subjected to the same analytical procedures as the actual data.

In the context of determining the likelihood of a calculated orbital period being the correct one, bootstrapping simulations were performed by randomly re-sampling the data with replacement, and calculating new periodograms. The fraction of periodograms in which the highest peak fell close to a particular alias can be interpreted as the likelihood of that alias being correct. However, the probabilities determined from this bootstrapping procedure are slightly on the pessimistic side. This is due to the fact that each simulation is using only a subset of

the entire available data. The random sampling with replacement means the simulated data set contains fewer unique epochs and as a result, there is some loss in the temporal definition. Additionally when picking out the best aliases interactively, rejection is based not only on the periodogram, but on aliases which result in the most meaningful phase folded light-curves or phased radial velocity curves, when analysing the periodograms of the actual observational data for each system.

3.9 Monte Carlo Simulations

Noise in data will manifest itself in a periodogram, and it is well known that sometimes noise can result in large spurious peaks in a periodogram which look like a real periodic signal. It is therefore important to carry out tests or develop a means by which signal which is simply an artifact of the noise can be separated from one created from a real periodic phenomena.

Monte Carlo simulations require some knowledge/assumption of the distribution of errors in a data set and the underlying process which created them so that synthetic data sets can be simulated. The procedure involves drawing random numbers from appropriate distributions to construct data sets with exactly the same number of measured points and precisely the same values of all control (independant) variables as the original data set D_0. The simulated data sets $D_1, D_2, ...$, are by construct supposed to have exactly the same statistical relationship in the simulated/estimated parameters as the original measured parameters in the original data set.

Monte Carlo simulations can be used to determine the significance of periods (Frescura et al. 2007; Horne & Baliunas 1986) and also provide a means of determining detection limits.The significance of periodogram peaks were determined for systems SDSS J0904+4402 and SDSS J0919+0857, and detection limits are discussed for SDSSJ 1711+3013 in Chapter 4 of this thesis.

Monte Carlo simulations were carried out using the data for each system. The process involved shuffling the original data, with each point having the same error as the original data set. This method implies that the 'model' is one which contains no periodic variation. The obvious result of the re-shuffling is that the temporal definition changes and the original 'signal' is lost. The re-sequencing of observations means that a new data set has been created. For each new

shuffled lightcurve a periodogram is produced, and since any coherent modulation in the data is missing the data looks more like white noise, any large spikes or periodicities are now due to random chance from the reshuffling. The highest peak of each periodogram is stored in a file and the process is carried out several hundred time and a distribution of the highest peaks is plotted. This plot represents the probability distribution of the peaks from all the periodograms. The significance the peaks is determined by over-plotting lines corresponding to the following sigma values, 1σ = 68%, 2σ = 95.4% and 3σ = 99.7%, this means that at 68% of the periodograms of simulated data have a peak at least as high as the signal in the original periodogram whose significance you want to test. Any peaks in the distribution which exceed the 3σ threshold are considered significant, while those that exceed the 2.5σ threshold but below the 3σ threshold are considered marginally significant.

Detection limits are determined by first detrending the data, i.e. by removing all frequencies related to the orbital period and the observing run. This is achieved using the `SINEFIT/TSA` context in `MIDAS`. Next a sine wave with an arbitrary frequency is 'injected' or the added to the lightcurve, and Monte Carlo simulations are carried out to see if it manifests itself as a significant (3σ) spike in the probability distribution. By varying the amplitude of the added sine until it falls below the 3σ line or indeed any desired threshold value one can determine the detection limit of a signal.

Chapter 4

Time-Series Photometric Observations of 15 CVs Identified by the SDSS

The Sloan Digital Sky Survey (SDSS; York et al. 2000) has the potential to dramatically improve the observational side of CV population studies. Sampling a large volume in *ugriz* colour space and extending deeper than any previous large-scale survey, SDSS provides the most homogeneous and complete sample of CVs to date. At the time of writing, the sample of definite SDSS CVs contains 213 systems, of which 177 are new discoveries (Szkody et al. 2002b, 2003a, 2004, 2005, 2006, 2007a **[henceforth PSI–PSVI]** Roelofs et al. 2004; Anderson et al. 2005; Schmidt et al. 2007, Groot et al. 2007, submitted). The newly identified CVs have been followed-up by a number of groups (e.g. Wolfe et al., 2003; Pretorius et al., 2004; Woudt & Warner, 2004; Peters & Thorstensen, 2005; Roelofs et al., 2005; Tramposch et al., 2005; Gänsicke et al., 2006; Southworth et al., 2006, 2007a,b; Littlefair et al., 2006a,b).

Our group was awarded the 2004/05 International Time Programme on La Palma and the following chapters report on the time-series photometric and spectroscopic observations which were carried out as part of the follow-up observations of the SDSS CVs.

4.1 Introduction

In this chapter, I present time-resolved CCD photometry of 15 CVs[1]. I provide a discussion of the morphology of the lightcurves and the CV subtypes and accurate orbital periods for 11 systems.

Sample light curves for each object are shown in Figure 4.1, where the SDSS identification spectra from PSI–V are also displayed for convenience. At a first visual inspection, the light curves of the observed systems display a wide variety of morphologies, including apparently non-periodic flickering (SDSS J0018+3454), deep eclipses (SDSS J1250+6655, SDSS J0901+4809), periodic double-humps (e.g. SDSS J0151+1400), double-peaked flare-like events (SDSS J0854+3905), or the absence of significant variability altogether (SDSS J1514+4549 and SDSS J0904+4402). The lightcurves obtained on different nights for an individual system are rather similar in all cases, except for SDSS J0901+4801 and SDSS J2116+1134, which were observed both in quiescence and in outburst. Objects of particular interest are SDSS J0901+4809 and SDSS J1250+6655 which are deeply eclipsing. SDSS J0854+3905 is a polar with an extremely modulated light curve, which is likely due to a mixture of cyclotron beaming and eclipses of the accretion region by the white dwarf. One out of the five systems with white-dwarf dominated optical spectra exhibits non-radial pulsations.

The choice of periodogram for each system in this chapter was dependant on the time series analysis which was most appropriate for each light-curve and provided the cleanest periodogram. As discussed in Section 3.5, Fourier type analysis are most appropriate for light-curves which display sinusoidal variations, whilst phase folding techniques are most appropriate for non-sinusoidally varying lightcurves and those with sharp variations such as eclipses.

The `scargle` periodogram was most appropriate for SDSS J1244+6135 as it displayed the strongest power corresponding to the orbital period compared to the `ort` and `aov` phase folding techniques, which displayed noise at lower frequencies corresponding to the sub harmonics of the orbital frequency. SDSS J1250+6655 was used as an example in Figure 3.3 Section 3.5 to show the different methods which can be used for time series analysis in `MIDAS TSA` context. The periodograms for SDSS J0901+4809 and SDSS J1250+6655, were produced by the method described in Section 3.6. For the rest of the CVs, the `ort` periodogram is shown. This phase

[1] As published in Dillon et al. (2008)

folding technique is not just better suited for these non-sinusoidal varying systems but due to the combined method of using a Fourier type analysis with a phase folding technique (as described in Section 3.5), the algorithm produces a much smoother periodogram than `aov`, by suppressing the alias periods and reducing the power/signals at lower frequencies.

4.2 Results on Individual Systems

4.2.1 SDSS J00183454.

The SDSS identification spectrum in Figure 4.1 displays strong narrow emission lines. While the strength of He II λ4686 is suggestive of a magnetic CV nature, the absence of noticeable polarisation ($< 0.2\%$) argues against SDSS J0018+3454 being a polar (PSIV). According to Szkody et al. (2005) time-series spectroscopy with 3 Å resolution obtained over a 2 h period failed to detect a significant radial velocity variation. Our photometry obtained over four nights shows non-periodic flickering activity with an amplitude of ~ 0.1 mag on time scales of $\sim 20 - 40$ min and night-to-night variations of ~ 0.3 mag. Close inspection of the SDSS spectrum of SDSS J0018+3454 reveals a broad absorption dip centred on 5150 Å, along with a host of narrow absorption lines in that range (see insert in Figure 4.1), typical of a mid-K main sequence star, strongly suggesting an early-type donor star. In fact, the continuum spectrum of SDSS J0018+3454 resembles closely that of SDSS J204448.92–045928.8, for which Peters & Thorstensen (2005) determined a donor star spectral type of K4–5 and an orbital period of 2419 min. The contribution of the donor star in SDSS J0018+3454 is weaker than in SDSS J2044–0459, indicating a relatively larger contribution of the accretion luminosity in SDSS J0018+3454. Combining the spectroscopic appearance with the absence of noticeable radial velocity variations over short time scales (PSIV), it appears likely that SDSS J0018+3454 is a long-period CV, and phase-resolved spectroscopy spanning a sufficiently long time should easily provide the radial velocity variation of the donor star from its absorption lines. The strong He II λ4686 emission line in a presumably long-period system is very untypical, and unravelling the nature of this object should be high-priority task.

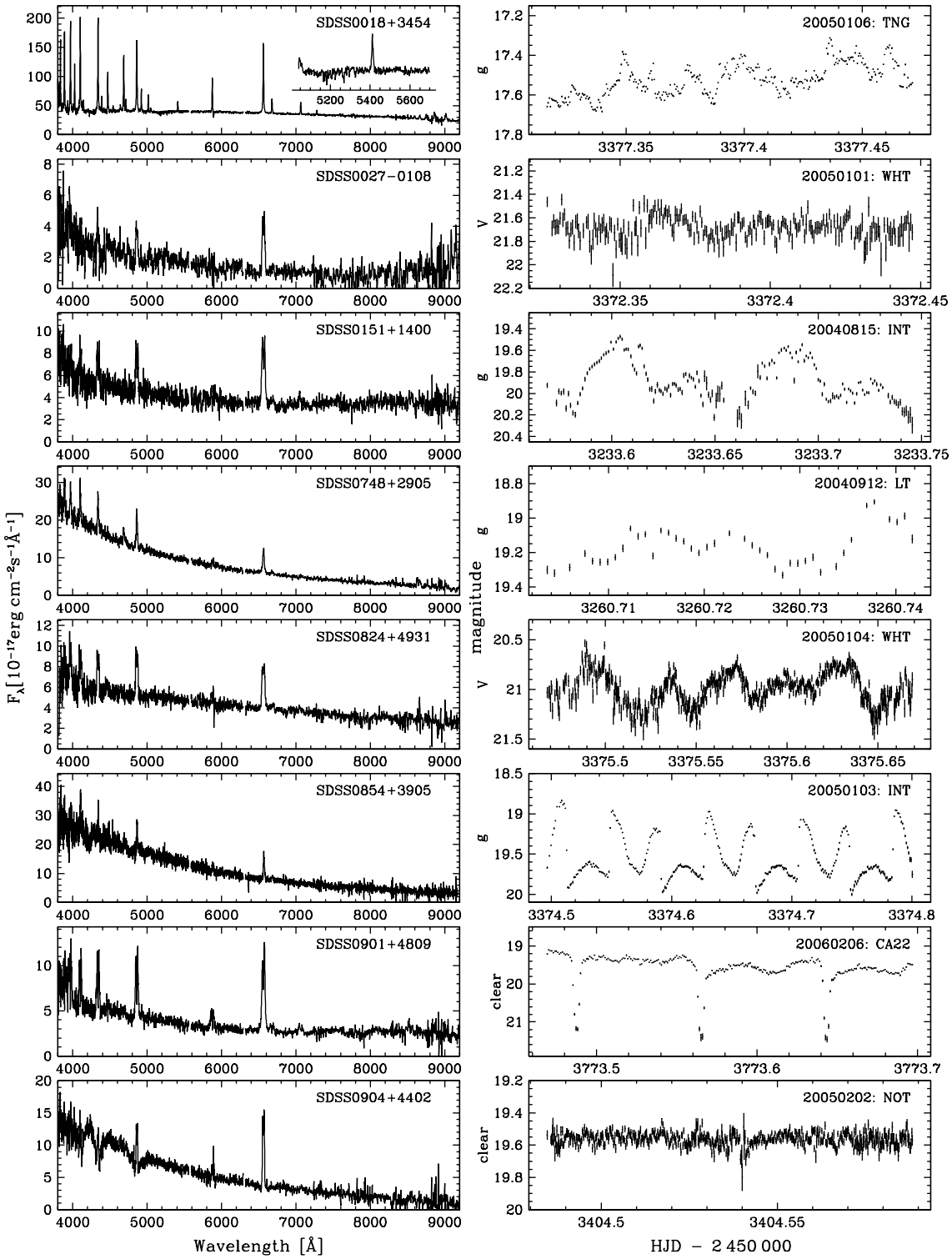

Figure 4.1: Sample lightcurves for all objects observed (Table 3.1) along with their SDSS identification spectra from PSI–V.

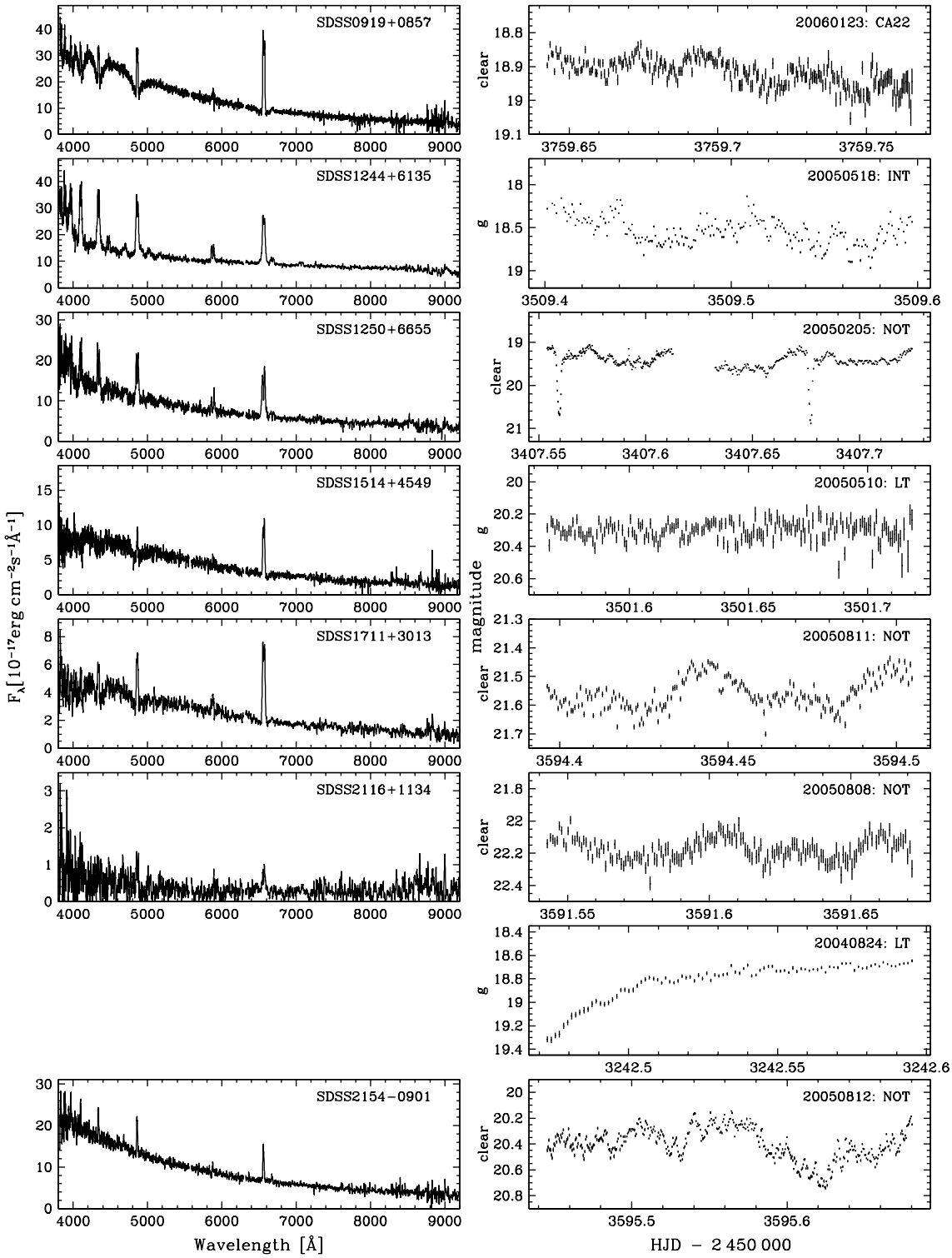

Figure 4.1 continued. Photometry of SDSS 2116+1134 was obtained both in quiescence and in outburst.

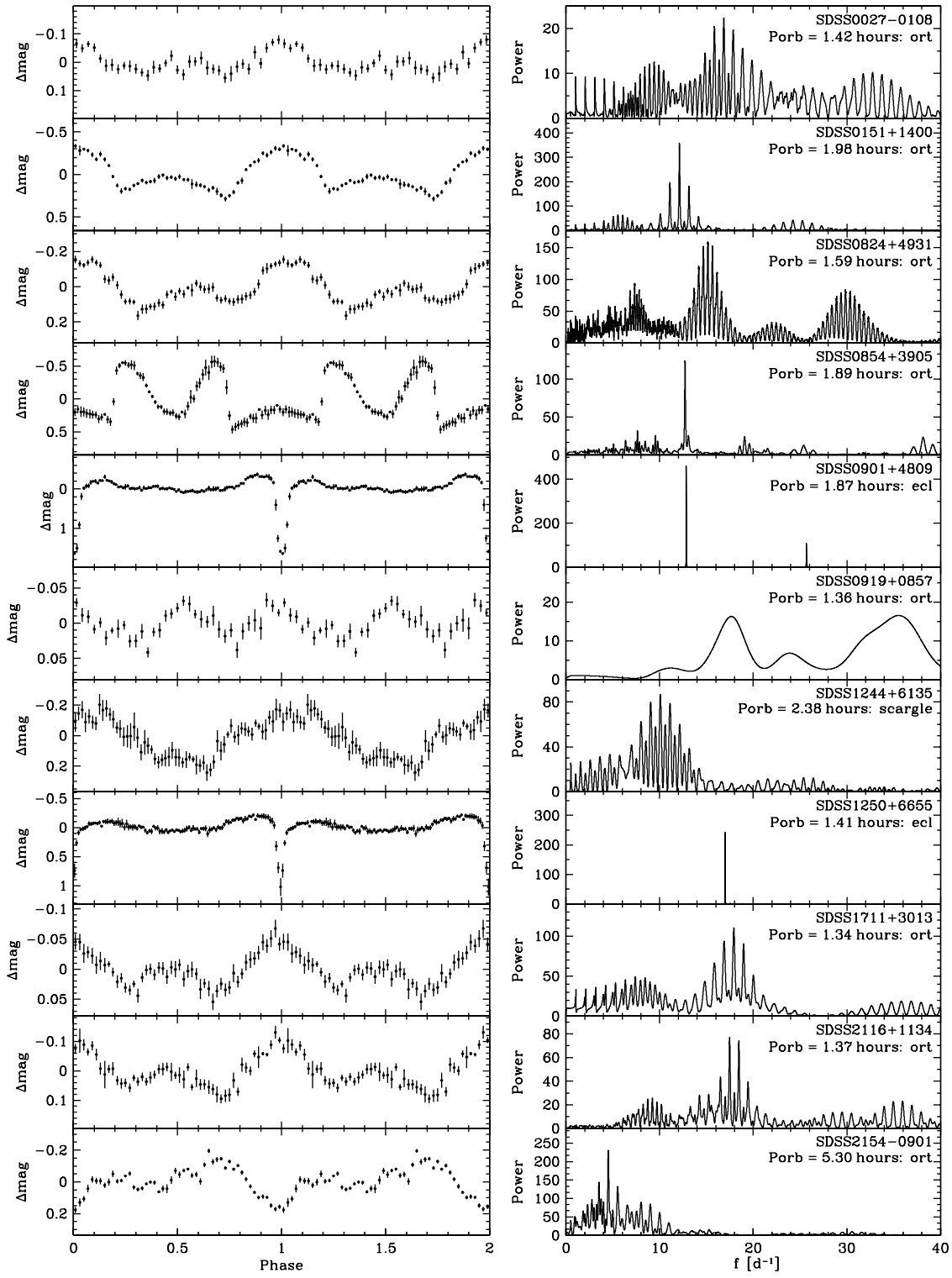

Figure 4.2: Periodograms (right panels) and phase-folded lightcurves (left panels) of the 11 SDSS CVs for which we could determine an orbital period from our photometry The method indicated to compute the individual periodograms (`scargle`, `aov`, `ort`) is indicated.

4.2.2 SDSS J0027−0108 (EN Cet).

This object has been identified as a dwarf nova in outburst and spectroscopically confirmed as a cataclysmic variable by Esamdin et al. (1997). The SDSS spectrum of EN Cet (Figure 4.1, PSIV) is of rather poor quality, containing a double-peaked Hα emission line. The observed flux upturn at the red end of the spectrum is interesting, as it could represent the donor star in this object. However, it appears more likely that it is an artifact from the night sky calibration, which is problematic in fibre spectroscopy at such low flux levels. The `ort` analysis of our *V*-band photometry obtained over three consecutive nights reveals a periodic signal at $16.9\mathrm{d}^{-1}$ (85.4 min) and contains power at the second harmonic as well (Figure 4.2). The `ort` periodogram was chosen for this system as phase-folding method of time-series analysis was better suited for a light-curve with a non-sinusoidal variation. The `aov` periodogram, provided the same value for the orbital period but displayed more power at the lower frequencies corresponding to the length of the run, than that for the peak corresponding to the orbital period. bootstrap simulation (Section 3.8) suggests a $\sim$ 73% probability for the choice of the strongest alias in the periodogram corresponding to the intrinsic period of the data, the flanking $1\mathrm{d}^{-1}$ aliases having likelihoods of $\sim$ 10%. Phase-folding the data using this period results in a light curve with a double-hump morphology (Figure 4.2). Such a light curve shape is observed in a number of ultrashort-period CVs, such as e.g. WZ Sge (Patterson et al., 1998a), RZ Leo, BC UMa, MM Hya, HV Vir (Patterson et al., 2003), WX Cet (Mennickent, 1994; Rogoziecki & Schwarzenberg-Czerny, 2001), and HS 2331+3905 (Araujo-Betancor et al., 2005c). The 85.4 min signal is interpreted as the orbital period of the system. From a sine-fit to the data, $P_{\mathrm{orb}} = 85.44 \pm 0.07$ min.

4.2.3 SDSS J0151+1400.

The SDSS spectrum of this object (Figure 4.1, PSI) contains double-peaked Balmer emission lines, suggesting a moderately high inclination. The He I lines are very weak, and the slope of the spectrum has a break near 6500 Å, suggesting that the secondary star may contribute to the observed flux in the red part of the SDSS spectrum. To explore this possibility, a three-component model was applied, consisting of a blackbody (to represent the blue continuum), an isothermal/isobaric hydrogen slab (Gänsicke et al. 1999, to represent the accretion disc), and an M-star template (Rebassa-Mansergas et al. 2007, to represent the secondary star). A reason-

able fit to the SDSS spectrum of SDSS J0151+1400 is achieved for a blackbody temperature of 8500 K, and a radius of the blue component of 1.4×10^9 cm, a slab temperature and column density of 5800 K and 2×10^{-2} g cm^{-2}, and a spectral type of the donor of M6, with all three components scaled to a distance of 480 pc (see Gänsicke et al. 2006; Rodríguez-Gil et al. 2005a; Southworth et al. 2006 for more details on this type of spectral modelling). These parameters should be considered with some caution, as the SDSS spectrum is of rather poor quality and covers an unknown orbital phase. Nevertheless, the spectral type suggested by the fit is consistent with the donor stars that are typically observed in this orbital period range (e.g. Silber et al., 1994; Remillard et al., 1994; Mennickent & Diaz, 2002). The geometric extension and temperature of the blue continuum component, combined with the absence of broad Balmer absorption lines, argues against an origin on the white dwarf but rather for an origin from the accretion disc edge and/or bright spot. A single outburst of SDSS J0151+1400 has been detected by Hiroyuki Maehara in January 2007 (vsnet-alert 9139).

The *g*-band lightcurves obtained on three consecutive nights display a double-humped morphology with an amplitude of ~ 0.3 mag. The strongest signal in an `ort` periodogram is detected at a frequency of $12.1\mathrm{d}^{-1}$ (118.8 min), with some power at the second harmonic (Figure 4.2). A bootstrap simulation shows that the alias choice is unambiguous for SDSS J0151+1400. In analogy to SDSS J0027–0108, we interpret the strongest signal as the orbital period of the system, and obtain from a sine-fit to the data $P_{\rm orb} = 118.68 \pm 0.04$ min.

4.2.4 SDSS J0748+2905.

While the identification spectrum displays He II emission (Figure 4.1, PSIII) the absence of noticeable polarisation ruled out a polar nature for this object (PSIII). An orbital period of 2.5 h was estimated by PSIII from radial velocity variations, though this must be considered no more than a rough estimate, as the system was observed only for $\simeq 2.6$ h. Our single *g*-band light curve covering ~ 1 h shows variability on time scales of 15–20 min with an amplitude of $\simeq 0.2$ mag. The system was found at a mean magnitude of $g \simeq 19.2$, whereas the light curve in PSIII showed the system at $V \simeq 18.3$, indicating long-term variability of the object (the nearby companion unresolved in the photometry reported in PSIII has $g = 22.5$ and can safely be neglected). No coherent periodicity was detected from our data, unsurprising since we were only able to ac-

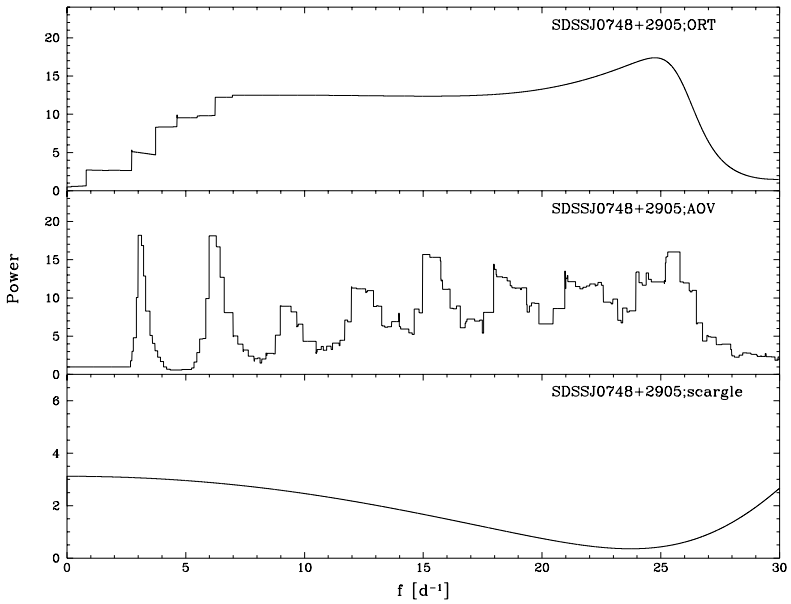

Figure 4.3: `ORT`, `AOV`, `scargle` periodograms for SDSS J0748+2905, from 55 min of photometric data. There is lack of structure and coherence in the periodograms which show nothing which could be attributed to the orbital period of the system.

quire 55 min of data. To illustrate this, I have provided the `scargle`, `ort`, `aov` periodograms for this system in figure 4.3. The peak in the `ort` periodogram corresponds to the length of the observing run, whilst the peaks at lower frequencies in the `aov` correspond to the sub-harmonics of the observational run.

4.2.5 SDSS J0824+4931.

The SDSS spectrum of SDSS J0824+4931 (Figure 4.1, PSI) broadly resembles that of SDSS J0027–0108 and SDSS J0151+1400 with slightly double-peaked Balmer emission lines along with very weak He I lines. The secondary star does not noticeably contribute at red wavelengths. The *V*-band lightcurves are of a double-humped shape with a ~ 0.5 mag amplitude. SDSS J0824+4931 was observed on three consecutive nights (Table 3.1), with very poor conditions in the second night. During the observations, SDSS J0824+4931 was substantially fainter than the magnitude reported from the SDSS imaging data. Using only the data from the first and the third night, an `ort` analysis results in an unambiguous signal at $15.16\mathrm{d}^{-1}$ (Figure 4.2), and a sine-fit to the data gives $P_{\mathrm{orb}} = 94.99 \pm 0.02$ min. In contrast, an `ort` analysis of the combined data from all three

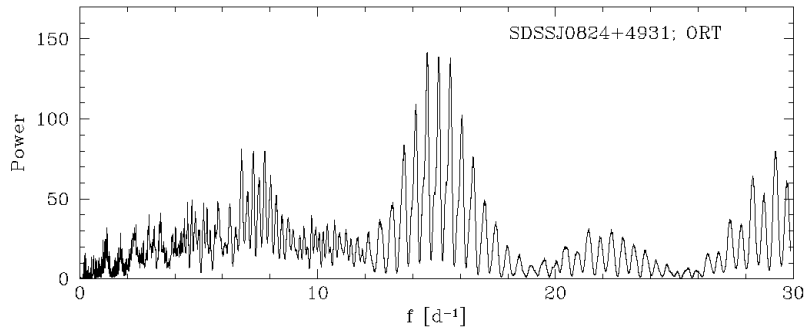

Figure 4.4: ORT periodogram for SDSS J0824+4931, using three nights of observations, showing equal power at three frequencies: 14.67d^{-1} (98.1 min), 15.16d^{-1} (95.0 min), and 15.65d^{-1} (92.0 min).

nights (shown in Figure 4.4) gives three possible frequencies: 14.67d^{-1} (98.1 min), 15.16d^{-1} (95.0 min), and 15.65d^{-1} (92.0 min). These three signals have roughly equal strength in the power spectrum, and similar probabilities in a bootstrap simulation.

Boyd et al. (2007) recently performed the first photometric study of SDSS J0824+4931 during a superoutburst, detecting superhumps with a period of 100.14±0.07 min and an underlying weak signal at 98.9±0.9 min, which they interpreted as the orbital period of the system, suggesting a superhump excess of $\epsilon = 0.13$. Using the superhump period from Boyd et al. (2007), our three possible orbital period aliases, 98.1 min, 95.0 min, and 92.0 min, result in $\epsilon = 0.021$, 0.054, 0.088, respectively. Based on Patterson's (2005) compilation of known superhump excesses, the 98.1 min alias seems most probable, as it implies a low, but not unusual superhump excess, similar to KV And (Patterson et al., 2003) and HS 0417+7445 (Aungwerojwit et al., 2006). The 95.0 min and 98.1 min periods are less likely and implausible respectively, as no dwarf novae with $\epsilon > 0.05$ are found below the period gap (e.g. Nogami et al., 2001; Patterson et al., 2003, 2005).

The exact value of the orbital period of SDSS J0824+4931 remains somewhat debatable. Erring on the conservative side, the value reported in Table 3.1 gives an error including the two flanking aliases in the photometry, hence $P_{\rm orb} = 95 \pm 3$ min.

4.2.6 SDSS J0854+3905 (EUVE J0854+390).

This system was identified as a possible magnetic CV by Christian et al. (2001). Their optical spectra displayed large radial velocity variations suggesting a period of < 0.2 d. The SDSS

spectrum (Figure 4.1, PSIV) shows the system fainter by a factor ~ 10 with much weaker He II emission. Spectropolarimetric observations of SDSS J0854+3905 confirm the magnetic nature of the system, displaying circular polarisation levels of up to -30% with cyclotron harmonic humps clearly visible in the spectrum (PSIV).

Two *g*-band lightcurves of SDSS J0854+3905 show a strong periodic double-peaked flare-like morphology with a peak-to-peak amplitude of ~ 1 mag with a period of ~ 2 h. An `ort` periodogram calculated from the data gives an unambiguous signal at $12.7\mathrm{d}^{-1}$ (113 min), and a sine-fit (including four harmonics because of the sharply modulated light curve morphology) results in $P_{\mathrm{orb}} = 113.26 \pm 0.03$ min (Figure 4.2).

The extreme shape of the modulation can be understood in terms of a combination of cyclotron beaming from the accretion column near the white dwarf and the accretion region being eclipsed by the white dwarf for parts of the spin cycle, similar to the geometry in AM Her (Gänsicke et al., 2001). Maximum flux occurs near the orbital phases $\varphi \simeq 0.26$ and $\varphi \simeq 0.68$ (Figure 4.2, where the zero-point of the phase is arbitrary), where the line-of-sight must be closest to being perpendicular to the magnetic field lines in the accretion column. The sharp rise and drop in flux observed near phases $\phi \simeq 0.2$ and $\phi \simeq 0.75$ recurs with high precision in both nights, and suggests that the accretion column/region is self-eclipsed by the body of the white dwarf. The drop in flux centred on $\phi \simeq 0.5$ occurs when the magnetic pole rotates into view, and the angle between the line-of-sight and the magnetic field lines in the accretion region reaches a minimum value. The modulation observed between $\phi \simeq 0.75 - 0.20$ could be related to accretion onto the second pole, or a geometric projection effect of the accretion stream. Given that the white dwarf spin in polars is magnetically locked to the orbital period, a period of $P_{\mathrm{orb}} = 113.26$ min is deduced. SDSS J0854+3905 appears to be a promising object for (spectro)polarimetric follow-up observations, which will allow a precise reconstruction of the accretion geometry.

4.2.7 SDSS J0901+4809.

The SDSS spectrum (Figure 4.1, PSII) shows deep central absorption structures in the Balmer and He I emission lines, suggesting a high inclination of the system. The slope of the spectrum displays a break near 6500 Å, similar to SDSS J0151+1400. Applying the same type of three-

component model as for SDSS J0151+1400, it is found that rather similar parameters provide a satisfactory fit to the SDSS spectrum of SDSS J0901+4809, i.e. a blackbody temperature and radius of 9500 K and 1.2×10^9 cm, respectively, a slab temperature and column density of 6100 K and 2×10^{-2} g cm^{-2}, respectively, and a donor star spectral type of M6, all scaled to a distance of 520 pc. All in all SDSS J0151+1400 and SDSS J0901+4809 seem to be very similar in their parameters, with the latter having a slightly higher inclination.

A single unfiltered light curve of SDSS J0901+4809 (Table 3.1) identifies the system as deeply eclipsing one. On 6 Oct 2007, one of our observers (SB), detected the first outburst of SDSS J0901+4809, finding the object at an unfiltered magnitude of ~ 16.2. Over the course of 5 days, it faded to an unfiltered magnitude of ~ 18.1, after which it was too faint for the equipment available at that time. The eclipse centres were measured by mirroring eclipse profiles and shifting them in time until the best overlap was achieved. The eclipse timings are reported in Table 4.1. A linear fit to the eclipse times results in the eclipse ephemeris:

$$T_{\rm eclipse}\,({\rm UTC}) = 2\,453\,773.48752(3) + 0.077880505(35) \times E \qquad (4.1)$$

i.e. an orbital period of 112.15 min (12.84d^{-1}). The corresponding cycle numbers and observed-minus-computed (O-C) eclipse times are reported in Table 4.1. There is a small chance for a cycle miscount, which would result in a somewhat shorter period of 0.077870588(50) d (112.13 min), however, the O-C values prefer the period given in Equation 4.1. SDSS J0901+4809 is a prime candidate for high time resolution eclipse studies to measure accurate binary parameters (see e.g. Feline et al., 2004a; Littlefair et al., 2006a).

4.2.8 SDSS J0904+4402.

The identification spectrum of SDSS J0904+4402 (Figure 4.1, PSIII) shows that the white dwarf is the dominant source of light in this system. No trace of the donor star is detected in the red part of the spectrum. Mildly double-peaked Balmer emission lines are superimposed on the broad absorption lines from the white dwarf. *g*-band and filterless photometry of SDSS J0904+4402 does not contain any periodicity that could be identified as the orbital period.

Inspired by the identification of a number of accreting white dwarfs among the SDSS

Table 4.1: Eclipse timings, cycle number, and the difference in observed minus computed eclipse times using the ephemerides in Equations (4.1) and (4.2).

Object	$T_{eclipse}$ (UTC)	O − C]] (s)	Cycle
SDSS J0901+4801	2453773.48757	4	0
	2453773.56532	-7	1
	2453773.64332	4	2
	2454379.78725	-1	7785
	2454379.86519	4	7786
	2454382.90215	-28	7825
	2454382.98060	21	7826
	2454383.36973	-2	7831
	2454383.44766	2	7832
	2454384.84940	-8	7850
	2454384.92749	11	7851
SDSS J1250+6655	2453407.55964	-1	0
	2453407.67713	1	2
	2453445.67918	5	649
	2453445.73774	-10	650
	2453447.49997	4	680
	2453447.55857	-9	681
	2453447.61750	9	682
	2454494.58109	6	18507
	2454494.63971	-4	18508
	2454494.69853	3	18509
	2454494.75714	-8	18510
	2454494.81597	1	18511
	2454496.57856	46	18541
	2454496.63684	7	18542
	2454496.69558	7	18543
	2454496.75419	-4	18544
	2454496.81320	20	18545
	2454496.93046	1	18547
	2454500.68934	-17	18611
	2454500.74828	2	18612

CVs which exhibit non-radial pulsations (Woudt & Warner, 2004; Warner & Woudt, 2004; Gänsicke et al., 2006; Nilsson et al., 2006), the periodogram of SDSS J0904+4402 were inspected for the presence of short-period signals. The INT *g*-band data shows (by means of a Monte-Carlo simulation as discussed in Section 3.9) a significant signal (3σ) at 8.678(34) min (165.94(65)d^{-1}) with an amplitude of 26 mmag (Figure 4.5). The NOT data shows two significant (3σ) level signals at 7.678(40) min (187.53(99)d^{-1}) and 12.16(11) min (118.8(1.1)d^{-1}), with amplitudes of 12.5 mmag and 11.3 mmag, respectively (Figure 4.6). However, given the fact that the two runs yield different periods, SDSS J0904+4402 would only be considered as a pulsating WD candidate, as accretion-related flickering could easily mimic such a putative pulsation signal. Additional time-series photometry is encouraged to test whether or not the periods detected at the INT and NOT are detected again.

4.2.9 SDSS J0919+0857.

The SDSS spectrum of SDSS J0919+0857 (Figure 4.1, PSIV) is dominated by the white dwarf with no signature from the donor star. PSIV estimated $P_{\mathrm{orb}} \simeq 1.4\,\mathrm{h}$ from 2 h of time-resolved spectroscopy, and compared the system to GW Lib, the first ZZ Ceti star found in a CV (van Zyl et al., 2000).

Our single filterless light curve shows humps with a period of ~ 40 min superimposed on a downward trend in the system brightness. Detrending the overall trend by subtracting from the light curve a copy of the data smoothed with an 80-point box car, an `ort` periodogram was computed from the detrended light curve containing broad peaks centred at a frequency of 17.7d^{-1} and its harmonic (Figure 4.2). This suggests that the actual morphology of the light curve is double-humped, similar to SDSS J0027–0108, SDSS J0151+1400, and SDSS J0824+4931. A sine-fit to the data results in $P_{\mathrm{orb}} = 81.6 \pm 1.2$ min.

The power spectrum at shorter periods reveals a marginally significant signal (2σ level) at 259.93 ± 0.94 s (332.41d^{-1}), which is interpreted as a possible non-radial pulsation mode (Figure 4.7). Based on the detection of that signal in additional data, Mukadam et al. (2007) confirmed SDSS J0919+5028 as a white dwarf pulsator.

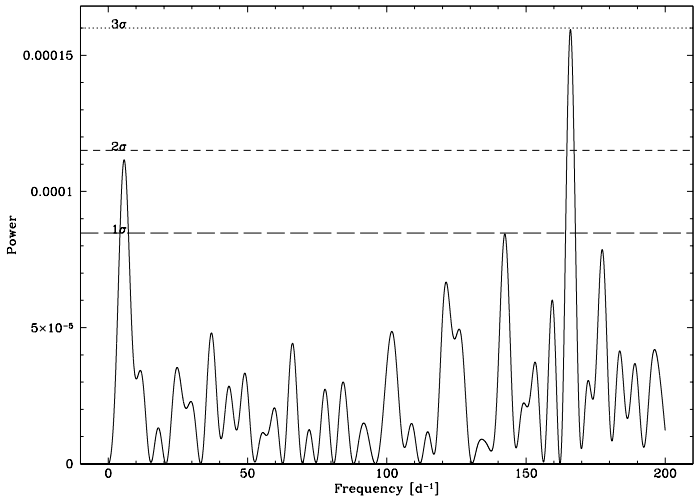

Figure 4.5: Monte Carlo simulation of SDSS J0904+4402 INT data. Significant signal at 8.678(34) min (165.94(65)d^{-1}) with an amplitude of 26 mmag

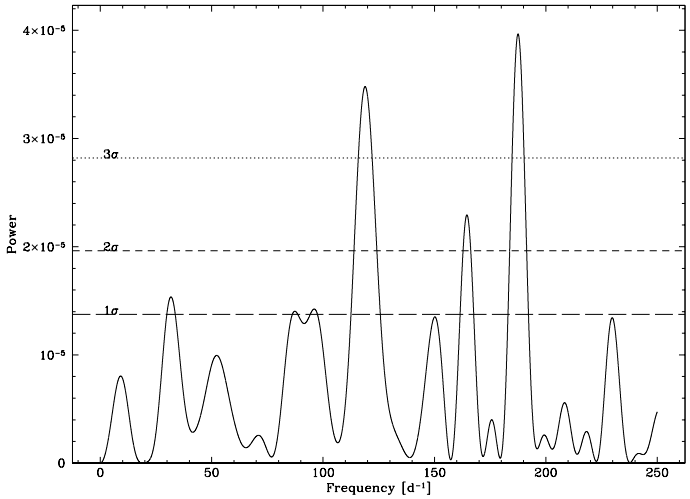

Figure 4.6: Monte Carlo simulation of SDSS J0904+4402 NOT data. Two significant signals at 7.678(40) min (187.53(99)d^{-1}) and 12.16(11) min (118.8(1.1)d^{-1}), with amplitudes of 12.5 mmag and 11.3 mmag,

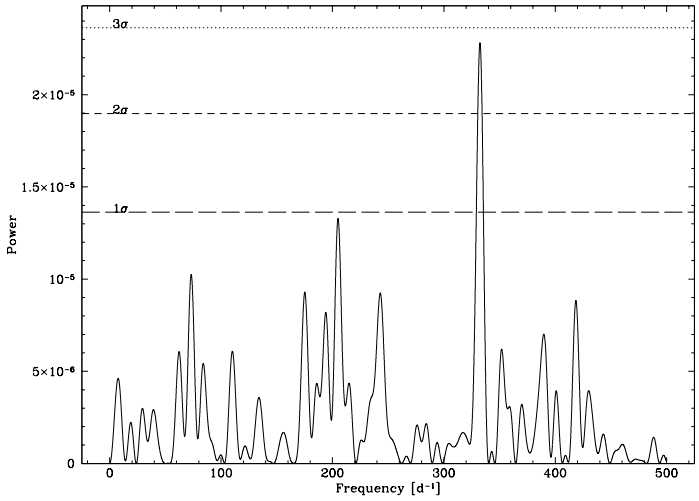

Figure 4.7: Monte Carlo simulation of SDSS J0919+0857 using Cafos data. A marginally significant signal at 259.93 ± 0.94 s ($332.41 \mathrm{d}^{-1}$), which is interpreted as a possible non-radial pulsation mode

4.2.10 SDSS J1244+6135.

The SDSS spectrum (Figure 4.1, PSII) displays strong double-peaked Balmer and He I emission lines, suggesting a high inclination. Our *g*-band data obtained over three consecutive nights reveals a periodic modulation with an amplitude of $\simeq 0.2$ mag. The `scargle` periodogram contains a cluster of aliases with the strongest signal at $10.0 \mathrm{d}^{-1}$ (144 min) (Figure 4.2). The absence of power at the second harmonic indicates that the light curve morphology of SDSS J1244+6135 is not, as in e.g. SDSS J0027–0108 or SDSS J0151+1400, double-humped. A bootstrap simulation shows that the alias choice is unambiguous with a likelihood of 97.2%. The observed modulation is interpreted as the orbital period, and determined as $P_{\mathrm{orb}} = 142.9 \pm 0.2$ min.

4.2.11 SDSS J1250+6655.

The identification spectrum of SDSS J1250+6655 (Figure 4.1, PSII) contains broad double-peaked Balmer emission lines with deep central absorption, typical of high-inclination systems. No spectroscopic feature from the donor star is detected in the red part of the spectrum. PSII suggested an orbital period of 5.6 h on the basis of a short (2.3 h) set of time-resolved spectroscopy, but the long (15 min) integration times could not resolve eclipses. The NOT light curve of SDSS J1250+6655 revealed the occurrence of deep (~ 2 mag) eclipses. A first outburst

of this CV was detected by one of our observers (SB) on 29th January 2008.

The mid-eclipse times (Table 4.1) were determined in an analogous way as for SDSS J0901+4809, and a linear fit to those times gives the following eclipse ephemeris:

$$T_{\rm eclipse}\,({\rm UTC}) = 24\,534\,07.55966(7) + 0.0587356870(43) \times E \qquad (4.2)$$

i.e. an orbital period of 84.57941(16) min ($\simeq 17.0{\rm d}^{-1}$). With SDSS J1250+6655 being close to the observed minimum orbital period for hydrogen CVs, eclipse studies appear especially worthwhile to determine accurate masses and radii for the stellar components in this system – lying between the eclipsing XZ Eri ($P_{\rm orb} = 88.0$ min, $M_2 = 0.0842 \pm 0.0024\,M_\odot$, Feline et al. 2004a) and SDSS J1035+0551 ($P_{\rm orb} = 82.1$ min, $M_2 = 0.052 \pm 0.002\,M_\odot$, Littlefair et al. 2006b; Southworth et al. 2006).

4.2.12 SDSS J1514+4549.

This is another white dwarf dominated CV, with no noticeable contribution from the donor star (Figure 4.1, PSIV). Our two *g*-band lightcurves reveal very little variability, and no periodicity that could be ascribed to the orbital period is detected in the periodograms calculated from the data. Our two observations found the object at a constant mean brightness of $g \simeq 20.2$. The periodograms created from the observations are shown in Figure 4.8. There is little power at all frequencies and no peak which could be ascribed to the orbital period. Nilsson et al. (2006) reported the detection of non-radial pulsations with a period of 559.3 s in two observations, and the absence of this signal in a third observation. The non-detection of this period in our two observing runs suggests that SDSS J1514+4559, if it is a pulsator, has a rather unstable pulsation spectrum.

4.2.13 SDSS J1711+3013.

Very similar to SDSS J1514+4549, the SDSS spectrum of SDSS J1711+3013 clearly reveals the white dwarf (Figure 4.1, PSIII) but no evidence for the secondary star. A total of 5 light curves were obtained on three consecutive nights in August 2004 and on two consecutive nights in August 2005. All lightcurves reveal a double-humped morphology. An `ort` periodogram of the

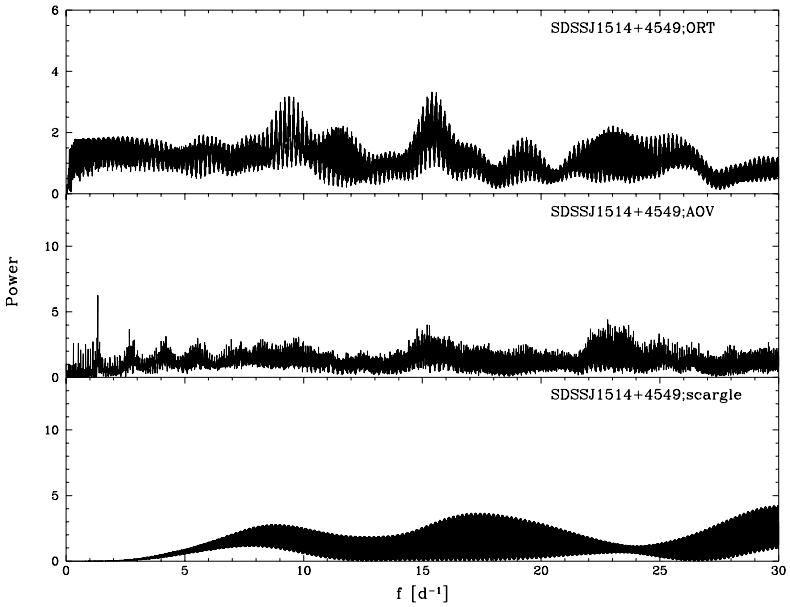

Figure 4.8: Periodograms for SDSS J1514+4549 from two nights of observations. There is very little power at all frequencies and hardly any variation within the periodograms.

2005 data, which is of better quality than the 2004 data, contains the strongest peak at $17.9\mathrm{d}^{-1}$ (80.4 min), which is interpreted as the orbital period (Figure 4.2). A bootstrap simulation shows that the choice of this alias is unambiguous (99.6% likelihood). A sine-fit to the data results in $P_{\mathrm{orb}} = 80.35 \pm 0.05$ min. Combining the data from both years confirms this result, but does not allow a more accurate period determination as the periodogram suffers from strong 1-year aliases (Figure 4.9). It is noted that no significant signal at shorter periods is found in any of the observations (Figure 4.10), with a detection limit of 12 mmag (see Section 3.9), which is consistent with the non-detection of ZZ Ceti pulsations in this object by Mukadam et al. (2007).

4.2.14 SDSS J2116+1134.

The SDSS spectrum of SDSS J2116+1134 (Figure 4.1, PSIII) shows double-peaked Balmer emission lines on a very weak continuum. The object was found in the SDSS imaging data at $g = 15.3$, whereas we measured $g = 21.8$ from the SDSS spectrum, clearly showing that SDSS J2116+1134 is a dwarf nova. In August 2004, photometry obtained with the LT found the object rising in magnitude from $g = 19.4$ to 18.6 over the course of a 3 h-long observing run, indicating another outburst of the system. In August 2005, filterless photometry obtained

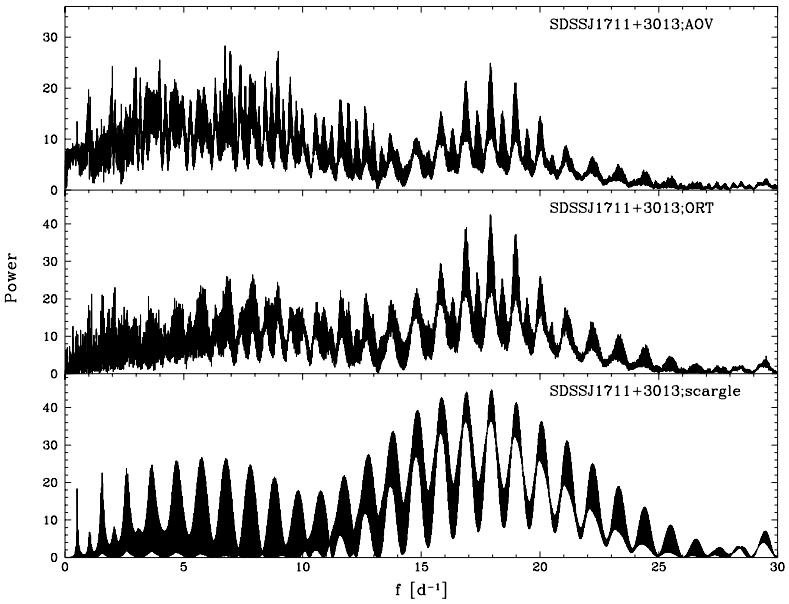

Figure 4.9: `AOV`, `ORT` and `scargle` periodograms for SDSS J1711+3013, created from 2004 and 2005 data, one can see the strong 1-year aliases in all periodograms.

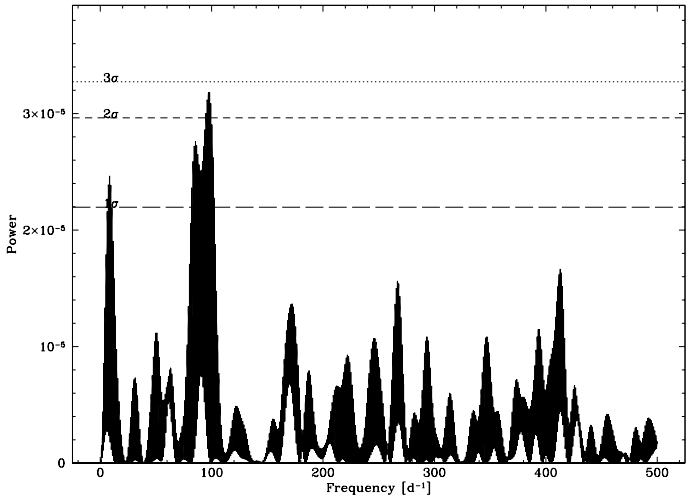

Figure 4.10: Monte Carlo simulation of SDSS J1711+3013. A sine with an amplitude of 12mmag was injected at $100\mathrm{d}^{-1}$ in the data, the signal falls just under the 3σ level detection limit.

over three consecutive nights showed the system at a mean magnitude of $g \simeq 22.2$, displaying a double-humped light curve. An `ort` periodogram contains two strong aliases at $17.5\mathrm{d}^{-1}$, (82.3 min) and $18.5\mathrm{d}^{-1}$, (77.8 min) (Figure 4.2), with the bootstrap test giving a 66% preference for the lower frequency alias. Sine fits to both aliases determine the two periods to ± 0.03 min, however, given the ambiguous choice of the correct alias, $P_{\mathrm{orb}} = 80.2 \pm 2.2$ min is adopted as a conservative value.

4.2.15 SDSS J2154−0901.

The identification spectrum of SDSS J2154–0901 (Figure 4.1, PSII) shows a blue continuum superimposed by relatively weak and narrow Balmer and HeI lines, as well as weak He II λ4686.

The lightcurves of SDSS J2154–0901 obtained over three consecutive nights show substantial flickering activity and a long-term modulation with a broad minimum and a steep decline. An `ort` periodogram contains a strong signal at $4.5\mathrm{d}^{-1}$, (320 min), and a sine fit to the data gives $P_{\mathrm{orb}} = 319 \pm 0.7$ min. SDSS J2154–0901 is the only system above the $2-3$ h period gap among the 11 systems for which a period could be determined.

4.3 Discussion

Our photometric study of 15 CVs contained within the SDSS spectroscopic data base has led to the determination of 11 orbital periods, along with additional information on CV subtypes (Table 3.1). In summary, the sample contains 1 system above the gap, 1 system within the gap, and 9 systems periods below the 2–3 h period gap.

A plot of the orbital period distribution of the 11 CVs discussed in this chapter is shown in Figure 4.11. The sample has been superimposed on the orbital period distribution of 455 CVs identified before the Sloan Digital Sky survey from V7.6 of the Ritter & Kolb 2003 catalogue. These systems are henceforth considered as the **non-SDSS** CV sample, referred to throughout this thesis. The CVs in the *non-SDSS* sample, have *no* spectrum in SDSS Data Release 6 (DR6, Adelman-McCarthy et al. 2007), and exclude all systems which were flagged as having an uncertain orbital period value. A further detailed discussion of this sample can be found in Section 6.3.

The orbital periods for four systems could not be determined, the main reason due to the lack of sufficient observational data both in quality and quantity. For all these systems further intensive follow-up i.e. a longer observations over consecutive nights with better signal-to-noise ratio will be an effective means for determining their orbital periods.

Based on their spectroscopic appearance the white-dwarf dominated SDSS J0904+4402 and SDSS J1514+4549 are likely to have periods below the gap. However for SDSS J0904+4402 only 6.74 hr of photometric data were acquired on two observations (NOT and INT) separated by a month, as was also the case for SDSS J1514+4549, where 5.6 hr of photometric observations were carried out on the LT over the course of a month. Clearly this tactic is not an effective means for determining the orbital period for these types of systems which have low luminosity accretion discs and probably low amplitude orbital modulations which have not been detected in our data. With regards to SDSS J0748+2905 and SDSS J0018+3454 their spectroscopic appearance seems to suggest that these systems are likely to have periods above the gap. It is therefore not surprising that a period could not be determined for SDSS J0748+2905 with only 55 min of photometric data! In the case of SDSS J0018+3454, this system shows little radial velocity variation (PSIV) and spectroscopic characteristics of CV with a mid-K sequence donor. It has also been compared to a similar CV; SDSS J204448.92−045928.8 for which Peters & Thorstensen (2005) determined an orbital period of 2419 min. For this system, a long sustained photometric campaign is the only means of determining the orbital period (Thorstensen, priv. comm) since a long orbital period implies a large orbital separation which would result in very low amplitude radial velocity variations already been confirmed by Szkody et al. (2005).

Thus far the results corroborate the findings of Szkody et al. (2003a, 2007a) and Southworth et al. (2006, 2007b), who noticed a larger fraction of short-period systems among the SDSS CVs compared to the previously known CVs (see e.g. Aungwerojwit et al. 2006 for CVs from the Hamburg Quasar Survey or Pretorius et al. 2007a for CVs from the Palomar Green Survey, which did not find more CVs below the period gap than above). In particular, five systems have periods within $\sim$ 5 min of the $\sim$ 80 min orbital minimum which constitutes the theoretical and now observed period minimum spike (Gänsicke et al. 2008 in prep), which is discussed in detail in Chapter 6. Three of those have optical spectra dominated by the white dwarf (SDSS J0027–0108, SDSS J0919+0857, and SDSS J1711+3013), with no signature from

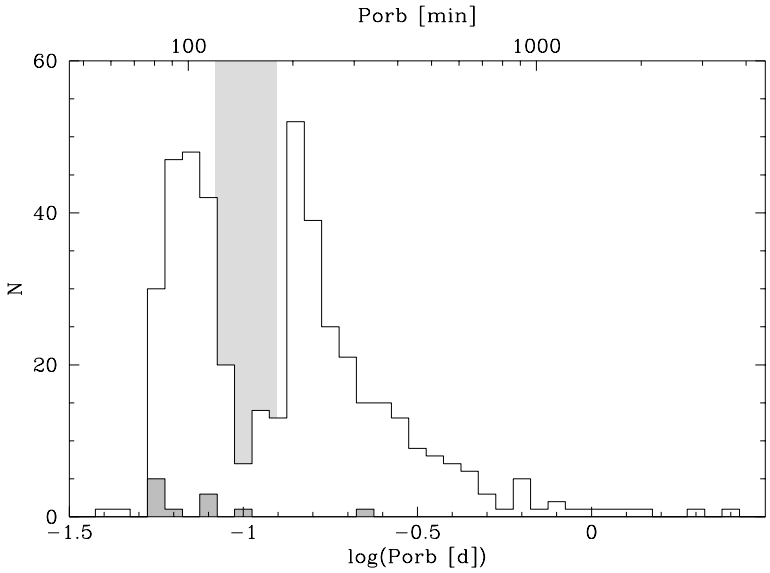

Figure 4.11: The orbital period distribution of the 11 CVs calculated from photometric observations in this chapter (*grey*). The location of the 2-3 hr period gap is highlighted by the grey region. The sample contains, 1 system above the gap, 1 system within, and 9 systems below. The photometric sample has been superimposed on the orbital period distribution of 455 CVs from V7.6 of the Ritter & Kolb 2003 catalogue (*white*) – *non-SDSS* CVs which have *no* spectroscopy in SDSS Data Release 6 excluding all systems which were flagged as having an uncertain orbital period value.

the mass donor, indicating both very low mass transfer rates and a very late spectral type of the companion star. All three closely resemble SDSS J1035+0551, an eclipsing white-dwarf dominated CV (Southworth et al., 2006) with a low-mass brown dwarf donor (Littlefair et al., 2006b). About ~ 20% of the CVs identified by SDSS have white-dwarf dominated spectra (PSI–VI), similar to SDSS J1035+0551 and the systems studied here, and orbital period measurements are available for ~ 20 of these systems, with the majority being found near the minimum period (e.g. Woudt & Warner, 2004; Pretorius et al., 2004; Zharikov et al., 2006; Gänsicke et al., 2006; Southworth et al., 2006, 2007b). Hence, it appears likely that complete follow-up of the SDSS CV sample will lead to a substantial increase of CVs with extremely short orbital periods.

Having discussed some of the intrinsic properties of the systems within the sample, and taking into consideration that SDSS seems to be picking up a larger fraction of shorter period systems, further analysis could help to determine whether or not the methods of identification of CVs in SDSS differs from the 'average' CV discovery method in the previously known sample.

Figure 4.12 shows the cumulative period distribution of the *non-SDSS* CVs and the *new-*

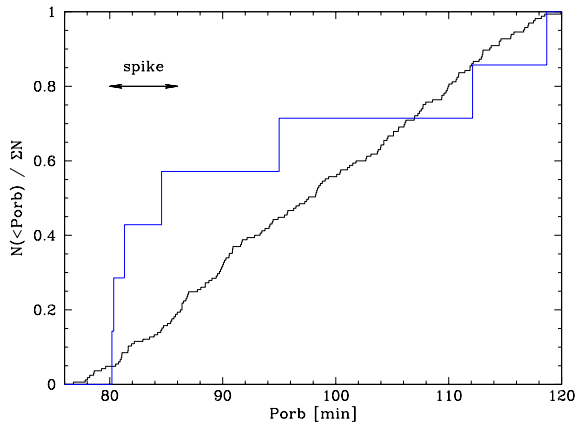

Figure 4.12: Normalised cumulative period distributions in the range $P_{\rm orb}$ = 76 – 120 min of (a) 455 CVs from Ritter & Kolb (2003; V7.6) – excluding systems with spectroscopy in SDSS DR6 and systems whose periods are marked as uncertain (*black*), (b) 7 of the newly CVs (see text) identified from SDSS (*blue*). A two-sided Kolmogorov-Smirnov comparing the distributions of the *non-SDSS* CVs and the sample of *new-SDSS* CVs in this chapter results in a 12.8% probability that the two distributions being drawn from the same parent population.

SDSS CVs on a linear scale in orbital period. A two-sided Kolmogorov-Smirnov (KS) test was applied in an attempt to determine whether or not the two distributions deviate from each other in a statistically significant way. The period range over which the limits[2] of the test were carried on, were set as 76.78 min, corresponding to the shortest-period "standard" hydrogen-rich CV, GW Lib, to 120 min, corresponding to the lower edge of the period gap. Consequently this means that CV sample is reduced to 7 *new-SDSS* CVs and 2 previously confirmed systems – *old-SDSS* CVs.

The KS test comparing the cumulative distributions of the *non-SDSS* CVs and the *new-SDSS* CVs in this sample, results in a 12.8% probability of the two distributions being drawn from the same parent population. This result shows that the period distribution of short period systems (<120 min) of the non-SDSS and new-SDSS CVs are not statistically different, although we do note the samples are small. On a positive note though, the above result might be further enhanced by the addition of the orbital periods of two systems – SDSS J0904+4402 and SDSS J1514+4549, if our hypothesis of them being short period systems were correct, which could not be determined this time around.

[2]Further detailed discussion of the limits chosen for the KS test are to be found in Section 6.3 as part of the discussion of the orbital period distribution of all CVs from SDSS.

A final note concerns the detection of non-radial pulsations in a number of SDSS CVs (Woudt & Warner, 2004; Gänsicke et al., 2006; Nilsson et al., 2006; Mukadam et al., 2007). While all of the confirmed pulsators have white-dwarf dominated spectra, it does not appear possible to predict the presence of pulsations in a given system just on the base of its optical spectrum. Among the CVs studied here, five exhibit the white dwarf in the SDSS spectrum, but only one system appears to be a non-radial pulsator (SDSS J0919+0857). Ultraviolet observations show that pulsations can appear over a wide range of white dwarf effective temperatures (Szkody et al., 2002a; Araujo-Betancor et al., 2005c; Szkody et al., 2007b), and hence the "instability strip" is apparently less well-defined than for single white dwarfs (Mukadam et al., 2004; Gianninas et al., 2006). This difference may be related to the contamination of the envelope by accreted helium in the CV white dwarfs (Arras et al., 2006).

4.4 Conclusions

In this chapter, time-series photometric observations of 15 CVs were presented from the SDSS spectroscopic database. Orbital periods could be determined for 11 of these systems. An overview of the properties of the CVs within this sample gives the following: two of the new CVs are eclipsing, SDSS J0901+4809 and SDSS J1250+6655, and are prime targets for detailed binary parameter studies. One polar, SDSS J0854+3905, exhibits a sharply modulated light curve and warrants polarimetric follow-up in order to establish the accretion geometry. Finally, only one out of five CVs having white-dwarf dominated spectra displays non-radial pulsations.

The results of this chapter corroborate the findings of Szkody et al. (2003a, 2007a) and Southworth et al. (2006, 2007b), who noticed a larger fraction of short-period systems among the SDSS CVs compared to the previously known CVs from the from the Hamburg Quasar Survey (Aungwerojwit et al. 2006) or the Palomar Green Survey (Pretorius et al. 2007a).

In order to determine whether or not this new sample differs from the Ritter & Kolb distribution in a statistically significant way, a KS test comparing the cumulative distributions of the *non-SDSS* CVs and the *new-SDSS* CVs in this sample was carried out. The results show 12.8% probability of the two distributions being drawn from the same parent population. This result is motivating but inconclusive since the sample is too small. However it is rapidly becom-

ing apparent that this is likely to change, since current investigations of SDSS CVs show that a complete follow-up of the SDSS CV sample will lead to a substantial increase in the number of CVs with short orbital periods (Szkody et al. 2003a, 2007a).

Chapter 5

Time-Series Spectroscopic and Photometric Observations of 14 CVs Identified by the SDSS.

5.1 Introduction

In this chapter I present the results of time-series spectroscopic and photometric follow-up observations of 14 SDSS CVs[1] . The SDSS identification spectrum of each object is shown in Figure 5.1. Systems of particular interest are SDSS J0903+3300 and SDSS J0932+4725 which are deeply eclipsing; SDSS J1249+0357, which shows no evidence of mass transfer and is a pre-CV candidate, and SDSS J2101+1052, which shows no variation or modulation in its spectroscopic properties, defying spectroscopic analysis. The periods with some accompanying details of each system are given in Table 3.2.

[1] Dillon et al. in prep (to be submitted)

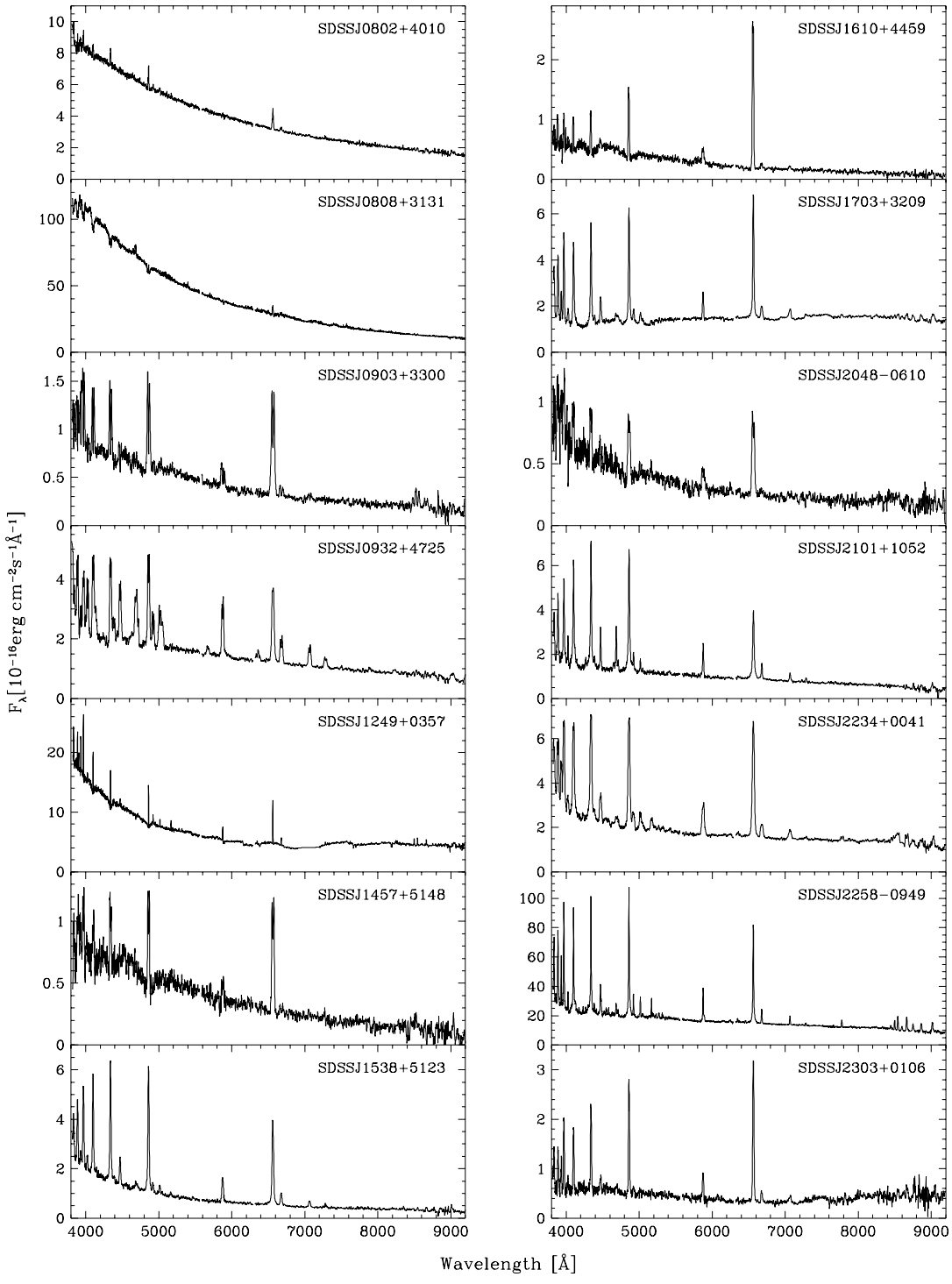

Figure 5.1: The SDSS identification spectra of all objects observed shown in Table 3.2 which are discussed in this chapter.

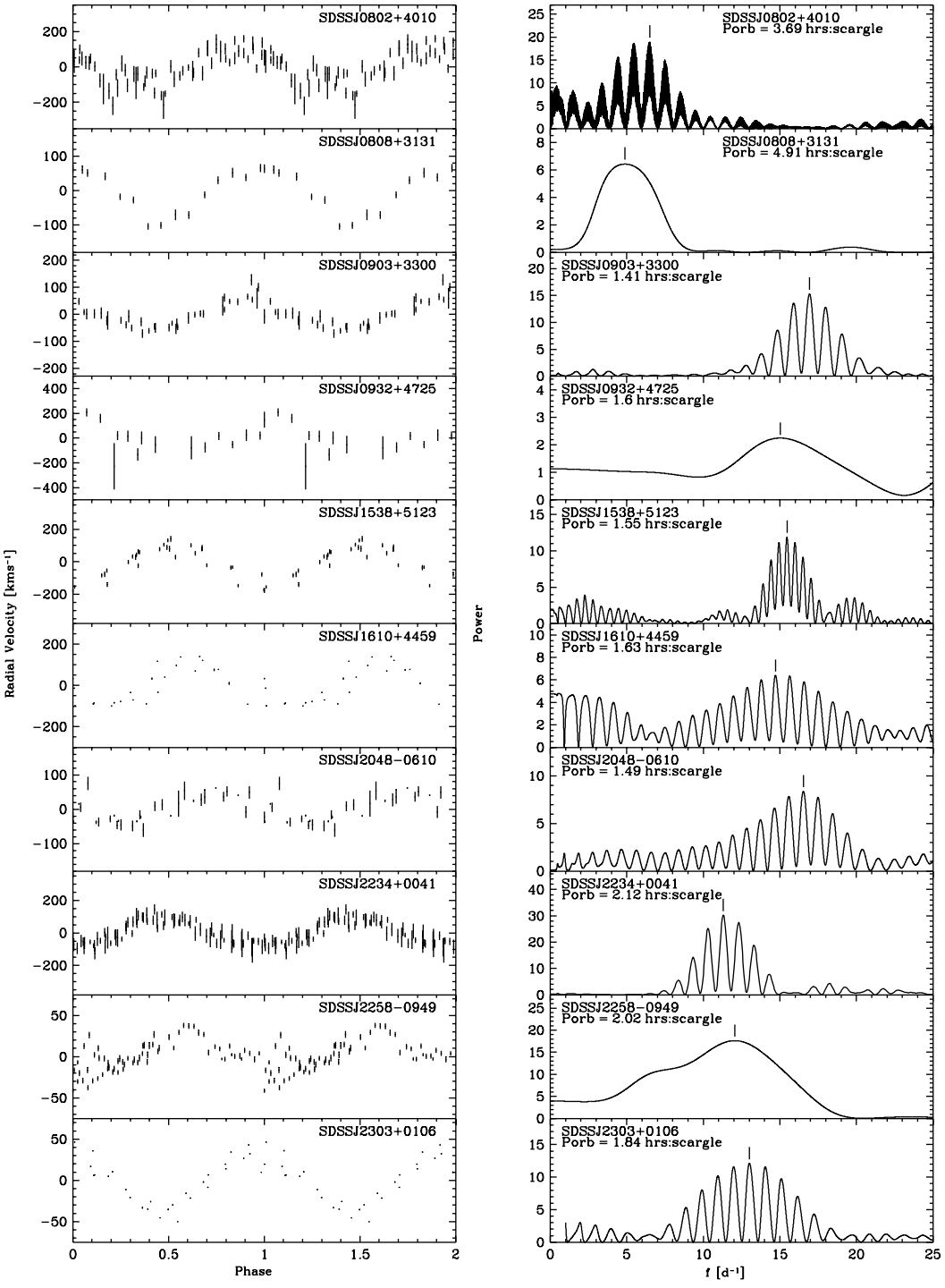

Figure 5.2: *Left panel*: Phased radial velocity curves for the CVs which the orbital period could be determined. *Right panel*: `Scargle` periodograms computed from Hα line radial velocity measurements. The frequencies corresponding to the orbital period (Table 3.2) have been highlighted with tick marks.

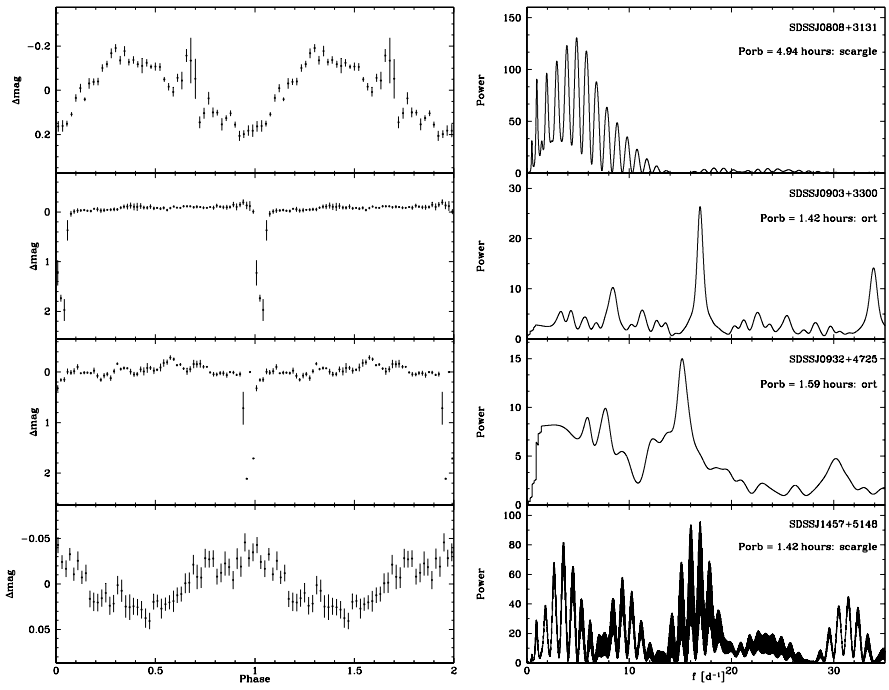

Figure 5.3: Phase-folded lightcurves of CVs with accompanying photometric data and the associated periodograms (Table 3.2).

5.2 Results on Individual Systems

5.2.1 SDSS J0802+4010

Also known by the designation KUV 07589+4019, this object was originally identified as an sdB star (Wegner & Boley, 1993) and is the northeastern component of a close pair of objects on the sky. The discovery spectra lacked the signal-to-noise ratio to detect Balmer emission lines. The SDSS spectrum (PSII) shows Balmer and weak He I emission lines, as confirmed by the three nights of spectroscopic observations at the NOT in 2004 November and December. PSII speculated that this CV is likely a low-inclination system with a high mass transfer rate – a typical novalike with a bright accretion disc.

The three nights of spectroscopic data were analysed using the double Gaussian technique with FWHM = 250km s^{-1} and a separation of 1300km s^{-1}. The resulting radial velocities give a period of $P_{\rm orb}$ = 221.62 ± 0.04 min (3.69 hr). Bootstrapping simulations using the `scargle` periodogram method give a 57% probability that this is the correct period.

5.2.2 SDSS J0808+3131.

The SDSS spectrum of this CV was taken during outburst. PSIII acquired a single 20 min APO[2] (Apache Point Observatory) spectrum in 2003 November and 9 hr of NOFS[3] (US Naval Observatory Flagstaff) photometry in 2004 January as part of follow-up observations for this system. The APO spectra displayed a dwarf nova-type CV in quiescence with strong emission lines, whilst photometric observations indicated a system in outburst at $V = 14.5$. The outbursts were considered to be lengthy as a week later the system was observed to be still at magnitude $V = 14.7$. The photometric observations at the time showed a modulation with an amplitude of 0.04 mag on a timescale of 6 hr, superimposed on a declining brightness trend throughout the observations.

Two nights of LT photometry show a variation with a peak-to-peak amplitude of 0.4 mag and low-amplitude short-term variability. The scargle periodogram computed from the photometry gives an orbital period of $P_{\rm orb} = 296.45 \pm 0.75$ min (4.94 hr) (Figure 5.2). Bootstrapping simulations indicate a 97% probability that this is the correct period.

By analysing the 5.3 hr of spectroscopic WHT observations using the double Gaussian technique on the Hα emission lines, with a Gaussian of FWHM = 100km s^{-1} and a separation of FWHM = 1100km s^{-1}, a period of $P_{\rm orb} = 301.41 \pm 11.12$ min (5.02 hr) is deduced.

As the time coverage of the photometric data acquired for this system is greater than that for the spectroscopic data, the resulting periodogram has a greater temporal resolution (compare Figure 5.2 and Figure 5.3). As a result, the orbital period calculated from the photometry is more precise, so it is adopted as the final value (Table 3.2).

5.2.3 SDSS J0903+3300.

The SDSS spectrum of this object (PSIV) displays strong double-peaked hydrogen Balmer emission lines with additional emission from He I, (strongest in the 5876 Å line) indicating a system with a high orbital inclination. There also seems to be some indication of flux coming from the

[2]Time-resolved spectroscopy was done at the 3.5m telescope in New Mexico at Apache Point Observatory (APO) equipped with a Double Imaging Spectrograph. The spectrograph was used in high-resolution mode (resolution about 3Å) with a 1.5" slit covering the wavelength regions of 4200 – 5000Å in the blue and 6300 – 7300Å in the red.

[3]Photometry was accomplished using with the US Naval Observatory Flagstaff Station (NOFS) 1m telescope, using a 2048x2048 SITe/Tektronix CCD, with no filter in order maximise the signal-to-noise ratio (S/N).

white dwarf. PSIV presented 2.4 hr of APO spectra with exposure times 900–1200 s, and from a double-Gaussian analysis found a period of roughly 1.3 hr (78 min).

A single night of INT photometry spanning 7 hr shows five eclipses with depths of 2.0 mag. An analysis of these eclipses gives an orbital period of $P_{\rm orb} = 85.22 \pm 0.14$ min. The full orbital ephemeris measured from the eclipses is:

$$\mathrm{T_{eclipse}\,(UTC)} = 2453371.5199(2) + 0.05918(9) \times E \tag{5.1}$$

where the figures in parentheses give the uncertainties in the last decimal place of the preceding numbers. See Table 5.1 for details of eclipse times.

In addition to the photometric observations, spectroscopic observations of this system using WHT/ISIS were carried out. A double-Gaussian analysis of the Hα line (FWHM = 200km s^{-1} and separation 2500km s^{-1}) gives a period of 84.99 ± 0.16 min (1.42 hr), which tallies very well with the orbital period determined from the photometry. Bootstrapping simulations of the radial velocity measurements provide a 87% probability that this is the correct period, the second-highest probability being assigned to the 1d^{-1} alias at 90.53 min. The period calculated from the eclipse fitting is quoted in Table 3.2.

5.2.4 SDSS J0932+4725.

The SDSS spectrum of this system (PSIII) shows double-peaked Balmer lines and strong emission of He II 4686 Å. This system was originally identified as US 691 in the Usher survey of faint objects at high galactic latitudes (Usher et al., 1982), and has been compared to SDSS J102347.67+003841.2 (Bond et al., 2002; Szkody et al., 2003a). PSIII were unable to establish the nature of the system, noting that neither SW Sex stars or polars show the strong double-peaked emission lines which imply an origin in an accretion disc. PSIII presented APO spectroscopy which suggests a period of 102 min (1.7 hr). The long integration times (900 s) used meant that the eclipsing nature of this system was not noticed. The overall errors were also stated to be large for the brightness level of the system (PSIII). Further studies of SDSS J0932+4725 (and SDSS J102347.67+003841.2) were carried out by Homer et al. (2006a).

SDSS J0932+4725 was considered to be a candidate intermediate polar (IP): strong He II

4686 Å emission is a telltale signature of magnetic systems but its emission lines lack the large equivalent widths and narrow components that are observed in polars. Homer et al. acquired two nights of photometry, covering seven deep eclipses. Four of the eclipses had sufficient time resolution to be used in the calculation of an ephemeris, resulting in an orbital period of 95.27 ± 0.20 min. With regards to X-ray data, the count rate was too low to construct an X-ray lightcurve of the system or even to constrain the emission model, although the X-ray-to-optical flux ratio was found to be fully consistent with known intermediate polars.

The single night of TNG photometry of SDSS J0932+4725 shows three eclipses with depths of 2.0 mag over the course of 6 hr. Using the eclipse fitting technique an orbital period of $P_{\rm orb} = 95.28 \pm 0.10$ min was calculated. Combining these eclipse timings with those of Homer et al. (2006a), a more accurate period of $P_{\rm orb} = 95.476 \pm 0.0001$ min can be determined. The full eclipse ephemeris is:

$$\mathrm{T_{eclipse}\,(UTC)} = 2453106.68432(8) + 0.06630326(8) \times E \tag{5.2}$$

In addition to the photometry, just over two hours of WHT spectroscopy was also acquired. A double-Gaussian analysis of the Hα emission line (using FWHM = 200km s^{-1} and a separation of 2100km s^{-1}) results in a period of approximately 90 min. This shows that the system exhibits velocity variations, but is not sufficient to improve the orbital period calculated from the eclipses, therefore the photometric period is adopted as the final value for the orbital period of SDSS J0932+4725. See Table 5.1 for details of eclipse times.

5.2.5 SDSS J1249+0357.

The SDSS spectrum of this system (PSIII) shows strong narrow Balmer lines and spectral signatures of a white dwarf and a M dwarf. There is no evidence of mass transfer as would be indicated by strong Balmer emission lines from an accretion disc, so the system is therefore likely to be a pre-CV. Only six 600 s spectra were taken for this system, and are shown in Figure 5.4. Radial velocity measurements (Table 5.2) of these spectra show only a small variation of around -20km s^{-1}, but differ from the velocity of the SDSS spectrum by as much as $\sim$30km s^{-1}. The radial velocity measurements of this system are around -15 ± 5km s^{-1}. This system is likely

Table 5.1: Measured eclipse timings for SDSS J0903+3300 and SDSS J0932+4725. The residuals of the linear fit, relative to the ephemerides in Equation 5.1 Equation 5.2 are given in the column marked $O - C$.

Object	$T_{eclipse}$ (UTC)	O − C (s)	Cycle
SDSS J0903+3300	2453371.52008	13	0
	2453371.57913	2	1
	2453371.63810	−16	2
	2453371.69714	−29	3
	2453371.75698		
SDSS J0932+4725	2453106.68445	11	0
Homer et al. (2006a)	2453106.75044	−16	1
	2453106.81690	−2	2
	2453137.64816	19	467
	2453137.71423	−1	468
	2453137.78013	−36	469
	2453137.84700	13	470
TNG Observations	2453378.66037	7	4102
	2453378.72665	5	4103
	2453378.79282	−7	4104

Table 5.2: Radial velocity measurements from the SDSS spectrum and the six WHT spectra of SDSS J1249+0357.

HJD	Radial Velocity (km/s)
2452426.666651	22.2 ± 10.7
2453371.745401	−10.6 ± 5.6
2453371.752491	−16.9 ± 4.9
2453371.759575	−18.7 ± 5.3
2453371.766660	−9.9 ± 5.1
2453371.776005	−20.5 ± 4.7

to be a system with a relatively long period.

5.2.6 SDSS J1457+5148.

The SDSS identification spectrum of this system shows the underlying white dwarf, with the deep central absorption features in the hydrogen Balmer lines that indicate a high-inclination system. The white dwarf is also likely to be pulsating (PSIV).

Our photometric observations seem to show small-amplitude short-period fluctuations,

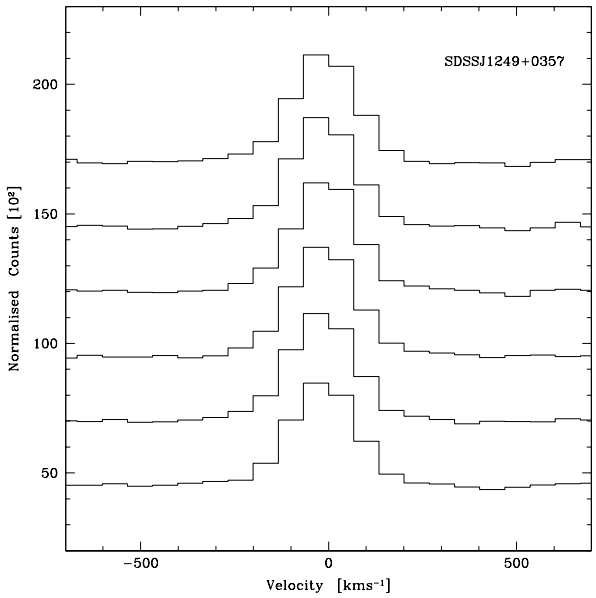

Figure 5.4: The Hα emission line in the six WHT spectra of SDSS J1249+0357. The spectra have been offset by arbitrary amounts for clarity.

which may be linked to the white dwarf pulsations. The `scargle` periodogram computed from the LT and NOT photometry gives a period of $P_{\rm orb} = 84.93 \pm 0.01$ min. Unfortunately there is a strong alias at 89.82 min. Bootstrapping simulations give a probability of 44% that the period is 84.93 min and 34% for the 89.82 min alias. The spectrum of this system was unfortunately too noisy which meant the quality was too low to ascertain any structure let alone measure any variation related to the radial velocity of the system (Figure 5.5). It is very apparent that further observations of this system are necessary to either reduce the power in the aliases of the photometric observations or to start spectroscopic observations from scratch.

5.2.7 SDSS J1538+5123

The SDSS spectrum of this system was presented by PSIII, as well as APO spectroscopy which indicates a period of 1.6 hr. The SDSS spectrum shows strong hydrogen Balmer emission, with additional He I emission. 31 spectra were obtained using the TNG over two nights in 2004 August. A double-Gaussian analysis of the Hα emission line (FWHM = 100km s^{-1} and a separation of 2100km s^{-1}) gives a period of $P_{\rm orb} = 93.11 \pm 0.09$ min (1.55 hr). Bootstrap simulations give a 100% probability that this is the correct period.

5.2.8 SDSS J1610+4459.

The SDSS spectrum of this system (PSIII) shows strong emission and absorption features in the Balmer lines and wide absorption due to the white dwarf component. There is some He I emission.

Our WHT spectra of this system shows strong Balmer emission which is clearly double-peaked. A single Gaussian analysis with FWHM = 800km s^{-1} gives a period of $P_{\rm orb}$ = 97.94 ± 0.42 min (1.63 hr) with very strong aliases at 104.52 min and 92.12 min. Bootstrapping simulations give a probability of 20% that this is the correct period, and the aliases have probabilities of 18% and 7%, respectively, giving a 45% probability, that the period of this system lies within an orbital period range 91.12 $\leq P_{\rm orb} \leq$ 104.52 min. This result means that this system has an orbital period shorter than the 2–3 hr period gap, but our observations are not able to provide an unambiguous period measurement. As a result, the period for this system has not been included in table 3.2. Further observations of this systems are necessary to reduce the power at the aliases, and provide a precise orbital period.

5.2.9 SDSS J1703+3209.

The SDSS spectrum of this system (PSIII) shows narrow Balmer emission lines accompanied with a signature of a secondary star. Closer inspection of the spectra reveals the presence of an absorption dip centred on 5150Å, along with numerous absorption lines in that range (see Figure 5.1). These features are typical of a mid-K main sequence star, which strongly suggests an early type donor. Spectroscopically this system is very similar to SDSS J0018+3454 (Dillon et al. (2008), also previous Chapter 4) and SDSS J204448.92-045928.8 for which (Peters & Thorstensen, 2005) determined a spectral type of K4-5 and an orbital period of 2419min. The trailed TNG spectra are shown in Figure 5.5 and also display no variation.

5.2.10 SDSS J2048−0610.

This system shows double-peaked hydrogen Balmer and He I emission lines, indicating a high-inclination system (PSII). The white dwarf component is also visible in the SDSS spectrum. 31 WHT spectra were obtained over two nights in 2005 July, and a double-Gaussian analysis

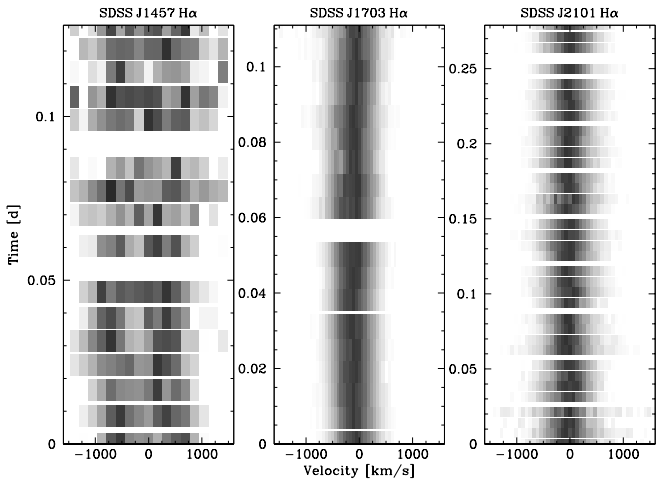

Figure 5.5: Trailed spectra of SDSSJ 1457+5148 (NOT), SDSS J1703+3209 (TNG) and SDSS J2101+1052 (WHT). No modulation or structure is apparent in any of the trail spectra constructed from any of the observations of these systems.

of these data (FWHM = 100km s^{-1} and separation 1800km s^{-1}) results in an orbital period of $P_{\rm orb}$ = 87.49 ± 0.32 min (1.46 hr). Bootstrapping simulations provide an 80% probability that this is the correct period, and low probabilities for the aliases at 82.67 min (11%) and 92.88 min (9%).

5.2.11 SDSS J2101+1052.

This system shows Balmer emission lines, with accompanying He I and strong He II emission indicative of a magnetic nature. PSII presented 1.3 hr of APO spectra which showed no velocity variation to a limit of 30km s^{-1}. The system was fainter in the Digitised Sky Survey *(DSS)* plates than in the SDSS observations, indicating that it has high and low states.

Further studies were carried out by Homer et al. (2006b), include 3.5 hr of NOFS photometry which were obtained 5.5 hr prior to 1.2 hr of XMM-Newton coverage. Spectra taken five days before these observations confirm that the Balmer and He II emission strengths were similar to that in the SDSS spectrum. Spectropolarimetric observations (see Homer et al. 2006b and references therein) yielded average polarisation values $|v| = |V/I| < 0.4\%$, ruling out a polarised nature for this system.

The XMM-Newton observations failed to detect any strong X-ray modulations. In fact,

the X-ray spectra indicated a cool thermal plasma ($\sim$ 10 keV) inconsistent with an IP, but more typical of a disc–accreting system and an obscured line of sight, leading to the conclusion that this is likely a low-inclination SW Sex star. Considering the NOFS lightcurve, Homer et al. speculated that the period of this system is approximately 107 min. According to PSII, further inspection of the lightcurve however did not seem to portray a clear-cut periodic modulation which could be attributed to the orbital period, although the system does fluctuate by 1.0 mag on a quasi-periodic timescale during the course of the photometry.

The data (Table 3.2), constitutes two consecutive nights of spectroscopic observations on the TNG in 2004 August (totalling 7 hr) and a further night of WHT spectroscopy in 2005 July lasting over 6 hr. The results from these observations are not very telling. Figure 5.5 shows trailed spectra from observations taken at the WHT, which is representative of all the data which were acquired. The data fail to show any variation in radial velocity and show no structure in the trailed spectra.

Further photometry covering more than 2 hr may shed some light on the nature of this system, and possibly provide some indication of its orbital period. For now, however, this system has remained stubborn in the face of both spectroscopic and X-ray analysis.

5.2.12 SDSS J2234+0041.

The SDSS identification spectrum of this object was presented by PSII, and shows a system with narrow hydrogen Balmer emission accompanied by He I emission lines. According to Szkody et al. (2003a), their 2 hr of APO spectroscopy indicates that this system has an orbital modulation at a period of 2 hr. They also say that this system was somewhat brighter in the SDSS spectroscopic observation, implying that it is likely a dwarf nova. In total 79 spectra over two nights were obtained with the TNG. A double Gaussian analysis (FWHM = 100km s^{-1} and a separation of 2000km s^{-1}) of the Hα emission yields radial velocities which give a period of $P_{\rm orb} = 127.29 \pm 0.25$ min (2.12 hr). Bootstrapping simulations give a 91% probability that this is the correct period. If this is an dwarf nova, further observations are necessary to determine the frequency and amplitude of the outbursts.

5.2.13 SDSS J2258−0949.

The SDSS spectrum of this system (PSII) shows strong narrow Balmer, He I and He II emission. This system was first identified as PB 7412, a blue star in the BF84 survey[4] (Berger & Fringant, 1984), and then classified as an emission-line object in the HK Survey[5] (Beers et al., 1996). This system is a dwarf nova which has been detected in outburst twice (vsnet-alert 8257, vsnet-campaign-dn 4366) in 2004 July and August and there have been indications of superhump modulations.

The NOT spectra did not provide any clear modulation for this system, possibly due to insufficient resolution, although it was once again caught in outburst on the final night of the run on the 2004 November 5th. However, this time the TNG observations proved to be more fruitful in determining a period, but unfortunately, the quality of the data had insufficient signal-to-noise to produces a clear concise folded radial velocity curve (Figure 5.2).

A double Gaussian analysis of the Hα emission line (FWHM = 100km s^{-1}and a separation of 900km s^{-1}) gave a period of $P_{\rm orb}$ = 119.45 ± 3.92 min (1.99 hr). Further observations of this system are necessary to reduce the error.

5.2.14 SDSS J2303+0106.

This is a dwarf nova system in which the secondary component can be identified in the SDSS spectrum (PSI). The system shows strong narrow hydrogen Balmer lines, accompanied with He I emission. APO spectra were obtained for this object both in quiescence and in outburst. In outburst, the system is brighter by a factor of 120 in the blue and 60 in the red with broad absorption features surrounding the Hβ and Hγ emission lines. Doppler tomography of the system indicated a low mass transfer rate and minimal disc emission, without evidence for a luminous hotspot near the mass transfer stream from the secondary star. A period of 100 min was determined from radial velocities of the Hα and Hβ emission lines.

Two nights of data were obtained at the WHT. A single Gaussian analysis of the Hα line (FWHM = 500km s^{-1}) gave a period $P_{\rm orb}$ = 110.51 ± 0.24 min (1.84 hr). Bootstrapping

[4]The BF84 Survey: a search for faint blue stars at high galactic latitudes near the South galactic pole.

[5]The HK Survey: northern and southern interference-filter/objective prism survey of Beers and collaborators. The HK refer to the H and K Ca II absorption features of target objects.

simulations give a 63% probability that this is the correct period. The next most likely alternative (31%) is an alias at 102.33 min.

5.3 Discussion

Time-series spectroscopic and photometric observations of 14 CVs has led to the determination of orbital periods for 9 systems identified from the SDSS spectroscopic data base, shown in Table 3.2. The orbital period distribution of these systems is shown in Figure 5.6. The sample contains 2 systems above the gap, 1 system within the gap, and 6 systems below the gap. Only one of these systems, SDSS J0903+3300 ($P_{\rm orb}$ = 85.22 ± 0.14 min), has a period within the 80-86 min period range which constitutes the theoretical and now observed period minimum spike (Gänsicke et al. 2008 in prep, Chapter 6).

The new sample has been superimposed on the orbital period distribution of 455 CVs from V7.6 of the Ritter & Kolb 2003 catalogue – also known as *non-SDSS* CVs which have *no* spectroscopy in SDSS Data Release 6 (DR 6 Adelman-McCarthy et al. 2007), and excluding all systems flagged as having an uncertain orbital period.

There were five systems for which definitive orbital periods could not be determined – SDSS J1249+0357, which is not a CV but a pre-CV candidate. SDSS J1457+5148, SDSS J1610 +4490, SDSS J1703+3209 and SDSS J2101+1052 are discussed in further detail below. As with systems from the previous chapter, recommendations for further observations are made in order to pinpoint the orbital periods of these systems.

The spectroscopic characteristics of SDSS J1457+5148 and SDSS J1610+4490 indicate that they are likely to reside below the period gap. The spectrum of SDSS J1457+5148 shows the presence of the WD with some contribution from the secondary star. Our photometric evidence suggests the presence of non-radial pulsations of the WD, although further observations are necessary to confirm the pulsations and determine the modes and frequencies. Unfortunately our data for this system was insufficient to provide an unambiguous orbital period, bootstrapping simulations gave a probability of 44% for an orbital period of $P_{\rm orb}$ = 84.93 ± 0.01 min and a 34% probability for a period of $P_{\rm orb}$ = 89.82 min. The results however, are sufficient enough to say that SDSS J1457+5148 resides below the period gap. This system can be compared

to previous CVs confirmed as containing a pulsating white dwarf, such as SDSS J1339+4847; $P_{\rm orb}$ = 82.52 min (Gänsicke et al., 2006), SDSS J0131-0901; $P_{\rm orb}$ = 81.54 min (Southworth et al., 2007b) and SDSS J0919+0857; $P_{\rm orb}$ = 81.60 min (Dillon et al., 2008; Mukadam et al., 2007). All these systems have periods very close to the 80 min period minimum. Additional photometric observations may be sufficient to accurately pin down the orbital period of this system or even better quality spectroscopy will help to determine whether or not SDSS J1457+5148 is another member of this group. With respect to SDSS J1610+4490, the presence of strong aliases in the periodogram proved a hinderance for unambiguous orbital period determination. The cause of this is due to the two very short spectroscopic observing runs 3.0 hr and 1.83 hr only separated by two nights at the WHT. Longer observations over consecutive nights will help reduce the power at the aliases and give an accurate orbital period. The spectrum of this system shows the presence of a WD but no signature from the secondary, indicating an evolved donor star and a low mass transfer rate.

The last two systems SDSS J1703+3209 and SDSS J2101+1052 are most likely long period systems residing above the period gap. The spectra of SDSS J1703+3209 shows the presence of a secondary component most likely a mid-K main sequence star. This system is comparable to SDSS J0018+3454 (Dillon et al. (2008), also see Chapter 4) which is speculated to have a long orbital period and SDSS J204448.92-045928.8 (Peters & Thorstensen, 2005) which has a K4-5 donor star and an orbital period of 2419 min (1.68 d). An extensive photometric or spectroscopic campaign would be ideal to determine the orbital period of this system.

Finally, SDSS J2101+1052, although previous studies by Homer et al. (2006b) were unable to constrain the X-ray properties of this system, whether or not it is an intermediate polar remains unconfirmed, the system shows similar properties to a confirmed IP HS 0943+1404 (Rodríguez-Gil et al., 2005b). Unfortunately spectroscopic analysis of this system was not able to provide further insight. The presence of strong He II line, and a doubling of the spectral lines, suggests the presence of a disc. It is likely that this CV is a high-mass accreting system, possibly a novalike. As previously stated, photometry covering more than the 2 hr acquired by Homer et al. (2006b) may shed some light on the nature of this system, an extensive photometric campaign could give an indication of its orbital period. For now, however, this system has remained stubborn in the face of both spectroscopic and X-ray analysis.

Table 5.3: Comparisons of Sample Properties.

Sample	Σ	80-86	< 2 h	2–3 h	> 3 h	$< g >$
Photometry	15	5	9	1	1	19.14
Photometric and Spectroscopic	14	1	6	1	2	18.26

A table comparing the number of CVs from the two samples of discussed in this thesis at the 80 – 86 min period minimum, below the period gap, within the 2–3 h period gap and above the gap. Note that the average magnitude of the mainly spectroscopic sample is 0.88 magnitude brighter than the photometric sample.

One can compare the orbital period distribution of the mainly spectroscopic sample of CVs to that of the *purely* photometric sample in Chapter 4 (as published in Dillon et al. 2008). Table 5.3 provides a breakdown. 6/14 (43%) systems in the mainly spectroscopic sample lie below the period gap, whilst only 1/15 (6.6%) of systems lie within the spike. The orbital period distribution has a tendency towards longer periods. In the photometric sample 9/15 (60%) of systems lie below the gap, whilst 5/15 (33%) of systems lie within the spike. In this sample the orbital period distribution has a definite tendency towards shorter orbital periods.

This characteristic is easily explained through the bias that arises when interactively determining candidates for spectroscopic observations. Since higher signal-to-noise is necessary for workable spectroscopic data, intrinsically brighter CVs are chosen (Table 5.3). Inherently these systems are likely to have higher mass transfer rates, driven by magnetic braking at longer orbital periods. As already discussed in Chapter 3, the average *g*-magnitude for the photometric sample is $< g_{phot} >= 19.14$ and the mainly spectroscopic sample $< g_{spec} >= 18.26$. The average magnitude of the mainly spectroscopic sample is 0.88 magnitude brighter than the photometric sample.

As with the photometric sample of CVs, a KS test was carried out to see if any difference between this sample of CVs varied from the previously known, *non-SDSS* sample.

Figure 5.7, shows the cumulative period distribution of the *non-SDSS* CVs and the *new-SDSS* CVs on a linear scale in orbital period. Using the same limits for a two-sided Kolmogorov-Smirnov test as in Chapter 4, (discussed in further detail in Section 6.3). Using the lower limit at the orbital period minimum at 76.78 min and the upper limit to the lower edge of the period gap at 120 min, the CV sample is reduced to 5 *new-SDSS* CVs and 1 previously confirmed system,

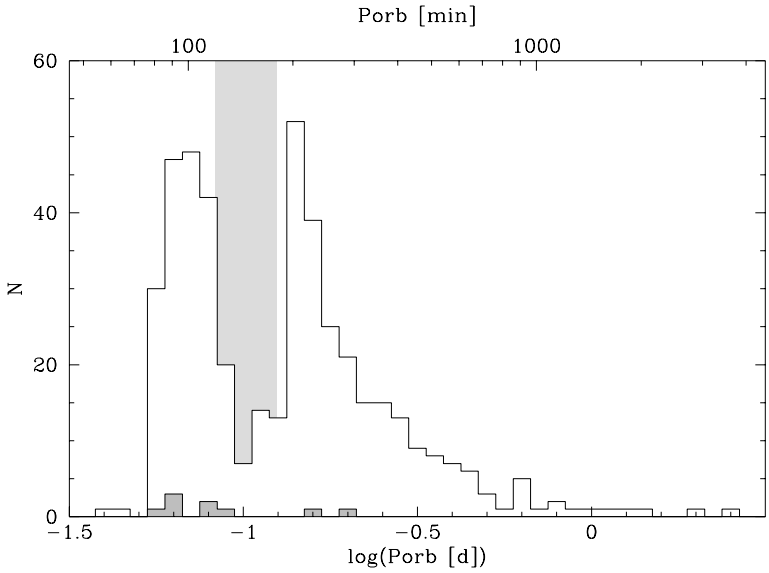

Figure 5.6: The orbital period distribution of the 9 CVs calculated from spectroscopic and photometric observations in this chapter (*grey*). The grey region shows the location of the 2-3 hr period gap. The sample contains, 2 system above the gap, 1 system within, and 6 below. The sample has been superimposed on the orbital period distribution of 455 CVs from V7.6 of the Ritter & Kolb 2003 catalogue (*white*) – *non-SDSS* CVs which have *no* spectroscopy in SDSS Data Release 6 and exclude all systems which were flagged as having an uncertain orbital period value.

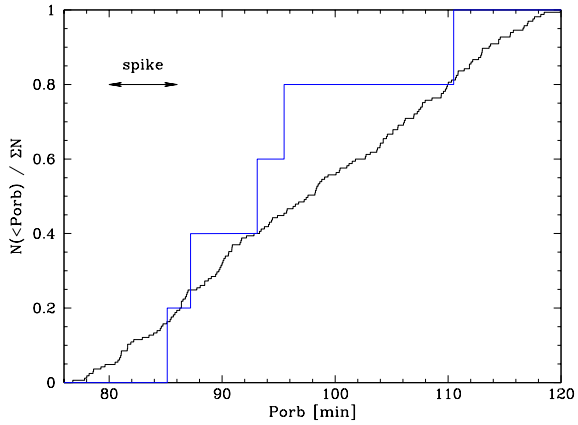

Figure 5.7: Normalised cumulative period distributions in the range $P_{\rm orb} = 76 - 120$ min of (a) 455 CVs from Ritter & Kolb (2003; V7.6) – excluding systems with spectroscopy in SDSS DR6 and systems whose periods are marked as uncertain (*black*), (b) 5 new CVs identified from SDSS (*blue*). A two-sided Kolmogorov-Smirnov comparing the distributions of the *non-SDSS* CVs and the sample of SDSS CVs in this chapter results in a 51.2% probability for the two distributions being drawn from the same parent population.

even smaller than the photometric sample discussed in Chapter 4.

The KS test comparing the cumulative distributions of the *non-SDSS* CVs and the *new-SDSS* CVs in this sample, results in a 51.2% probability of the two distributions being drawn from the same parent population, the two samples do not even differ at 1σ level. The result is interesting since by design, the spectroscopic sample is brighter, and this implies that the sample is likely to contain systems with higher mass transfer rates and hence longer orbital periods similar to the *non-SDSS* CVs.

5.4 Conclusions

Time-series spectroscopy was obtained for 14 systems contained in the SDSS database, with additional time-series photometric observations for five of the systems. 9 orbital periods have been established for the 13 CVs. For the remaining 5 systems orbital periods could not be determined, 4 are CVs and one system; SDSS J1249+0357, is a pre-CV candidate. Of the remaining CVs, two are speculated to reside below the gap. One of these systems, SDSS J1457+5148, may contain a pulsating white dwarf, but requires further time-series photometric observations to confirm this hypothesis.

A two-sided Kolmogorov-Smirnov test on the small sample of CVs did not provide evidence that it was statistically different to the previously known sample of CVs. Even though in this group of 13 CVs, 6 systems have periods below the gap – only one system has a period within the 80-86 min period range which constitutes the period minimum spike (Gänsicke et al. 2008 in prep). This can be compared to the five systems mentioned in the previous chapter. Indeed it could be the deviation towards longer periods expected to be found in a dominantly spectroscopic sample that has also contributed to such a inconclusive result.

Chapter 6

The Period Minimum Spike

This chapter has been adapted from a paper due for submission May 2008[1], of which I am named second author and is still undergoing review from associated collaborators. I inform the reader that sole contribution has been made by Boris T. Gänsicke in Sections 6.4, 6.5, 6.6 as stated in the declarations of this thesis.

6.1 Introduction

CVs with main-sequence or slightly evolved donors evolve towards lower mass transfer rates, longer evolutionary timescales and shorter orbital periods, via angular momentum loss through gravitational radiation (Faulkner, 1971; Paczynski & Sienkiewicz, 1981) and/or magnetic braking (Verbunt & Zwaan, 1981; Rappaport et al., 1983). This process continues until the mass of the donor is too low to sustain hydrogen burning and starts to become degenerate. At this point, the evolution of the binary orbit reverses towards longer orbital periods, providing a strong premise for the existence of a minimum orbital period (Rappaport et al., 1982; Paczyński & Sienkiewicz, 1983). Since the probability of detecting a system at a given range in orbital period is proportional to the time it requires to evolve through that range, $N(P) \propto 1/|\dot{P}|$, a significant accumulation of CVs at the minimum period is expected, often dubbed *the period minimum spike* (Kolb & Baraffe, 1999).

While a sharp minimum orbital period is found in the observed sample (e.g. Knigge,

[1] At the time of corrections of this thesis in February 2009, the afore mentioned paper still awaiting submission.

2006), no accumulation of systems at that period has yet been detected. This absence of the predicted pile-up of systems near the minimum period among the observed CVs has been one of the most intensively debated discrepancies between CV evolution theory and observations (Patterson, 1998; Kolb & Baraffe, 1999; King et al., 2002; Barker & Kolb, 2003; Willems et al., 2005), casting doubts on our understanding of compact binary evolution in general.

The following chapter contains a compilation of orbital period measurements for 116 SDSS CVs, and shows that the period distribution of these systems differs dramatically from all previously examined samples [2]. In particular, a clear accumulation of systems in the period range 80–86 min is observed, consistent with the prediction of a period minimum spike made by the population models. Furthermore it is also shown that the bulk of the systems in this spike display distinctly different properties from the average short-period ($\lesssim 120$ min) CV.

6.2 Orbital Period Measurements

For the purposes of quantitative comparison between the original orbital period distribution of an observed sample of CVs and that of a population model, some care has to be taken concerning the actual period measurements included in the observed distribution.

Given that CV periods are in the range from 80 min to about a day, a single night of data will hence cover at most a few orbital cycles, and the typical lower limit on the error of orbital periods from such data is $\sim 10\%$. More accurate period determinations are obtained by combining data obtained over a number of nights. However, this potential for an improved period measurement comes at the price of an additional uncertainty. As the CV orbital periods are often much shorter than a day, the number of orbital cycles in between the two or more observing nights may be ambiguous, which is known as cycle-count uncertainty, or aliasing. Section 3.8 discusses the methods used to establish the probability of different cycle-count aliases.

An additional note concerns the indirect orbital period determination for CVs exhibiting photometric variability in the form of superhumps, which are thought to be related to tidal interactions between the donor star and the accretion disc. Stolz & Schoembs (1984) published an empirical relation between the superhump period and the orbital period, that has been used

[2] AM CVn stars are excluded from the analysis. These are ultrashort helium-rich double-degenerate binaries that are not included in the standard CV population models.

to estimate $P_{\rm orb}$ for a number of CVs. In order to assess the error of these orbital period estimates, an up-to-date compilation on superhumping systems by Patterson et al. (2005) was used. A linear relation to the superhump excess (ϵ) and orbital period data provided by Patterson et al. (2005) was fitted. Systems above $P_{\rm orb} = 0.1\,{\rm d}$, where the scatter in the relation becomes large were excluded, as well as EG Cnc, WZ Sge, AL Com and DI UMa which have unusually small values of ϵ. The result of this fit shows that the 1σ error on orbital periods determined from a superhump period is $\sim 7 - 10\,{\rm min}$ for systems with $P_{\rm orb} \lesssim 2.5\,{\rm h}$, and hence rather crude (see also Schreiber 2007).

In order to fulfill the scientific motivation of producing an orbital period distribution, the published orbital period measurements of every individual SDSS CV were inspected. Systems where the relative error on the orbital period measurement exceeded 3% were excluded, along with those where there was substantial doubt on the correct choice of cycle count alias.

The SDSS CVs that passed that scrutiny are listed in Table 6.1 for CVs that were identified from SDSS spectroscopy, and in Table 6.2 for those CVs which were previously known, and re-identified among the SDSS spectra.

Table 6.1: CVs identified by the SDSS (*new SDSS CVs*) with reliable orbital period determinations. The CV type is given as DN = dwarf nova, i.e. at least one optical outburst has been detected; AM = AM Her star, i.e. the system shows characteristics of a strongly magnetic CV, IP = intermediate polar, i.e. coherent short-period variability related to the white dwarf spin is detected; NL = novalike variable, i.e. the system is in a persistent state of high mass transfer; EC = eclipsing. Two additional flags are given, WD = the SDSS spectrum is dominated by the white dwarf, RASS = the system has been detected in the ROSAT All Sky Survey. ‡ on the $P_{\rm orb}$ of some systems indicates systems for which the orbital period is known to a high-degree of accuracy.

SDSSJ	g	$P_{\rm orb}$ [min]	Type	WD	RASS	Reference
003941.06+005427.5	20.6	91.50±0.16	CV	Y	N	IV,1
004335.14-003729.8	19.8	83.39±0.08	CV	Y	N	III,2
005050.88+000912.7	20.4	80.3±2.2	CV	Y	N	IV,3
013132.39-090122.3	18.3	81.54±0.13	CV	Y	N	II,3
013701.06-091234.9	18.7	79.71±0.01	DN	Y	N	II,4
015151.87+140047.2	20.3	118.68±0.04	DN	N	N	I,5
015543.40+002807.2	15.4	87.14‡	AM/EC	N	Y	I,6,7,8
023322.6+005059.50	19.9	96.08±0.09	IP:	N	N	I,9
032855.00+052254.2	18.0	121.97±0.25	AM	N	N	VI
040714.78-064425.1	17.8	245.04±0.04	DN/EC	N	N	II,10
075240.45+362823.2	17.7	164.4±3.0	AM	N	N	II,11
075443.01+500729.2	17.3	205.965±0.014	NL/EC	N	N	V,3
080215.38+401047.1	16.7	221.62±0.04	NL	N	N	II,12
080434.20+510349.2	17.9	84.96±30.04	DN	Y	N	V,13,14,15
080846.19+313106.0	19.4	294.45±0.75	DN	N	N	III,12
080908.39+381406.2	15.6	193.014±0.012	NL/EC	N	N	II,16
081256.85+191157.8	15.8	230.5	NL	N	N	V,17
081321.91+452809.4	18.3	416.2±0.6	DN	N	N	I,18
081352.02+281317.3	17.1	175	CV	N	N	IV,17
082409.72+493124.4	19.3	95±3	DN	N	N	I,5,19
084400.10+023919.3	18.3	298.1±0.7	CV	N	N	II,17
090103.93+480911.1	19.3	112.14±0.01	DN/EC	N	N	II,5
090350.73+330036.1	18.8	85.065‡	CV/EC	N	N	IV,12,20
090403.48+035501.2	19.2	86.0	CV	Y	N	III,21
091127.36+084140.7	19.7	295.74±0.22	CV	N	N	IV,9
091945.11+085710.0	18.2	81.3±0.2	CV	Y	N	IV,5,17
092009.54+004244.9	17.5	212.94±0.01	CV/EC	N	N	II,22
093249.56+472523.0	17.8	95.476‡	CV/EC	N	N	III,12,23
103100.55+202832.2	18.3	83.2±2.3	AM	N	N	24
103533.02+055158.3	18.8	82.090‡	CV/EC	Y	N	V,9,20,25
121209.31+013627.7	18.0	88.428‡	AM	Y	N	26,27,28
121607.03+052013.9	20.1	98.82±0.16	CV	Y	N	III,9
122740.82+513924.9	19.1	90.649‡	DN/EC	Y	N	V,20,29
123813.73-033932.9	17.8	80.52±0.50	CV	Y	N	II,30
124426.25+613514.5	18.8	142.9±0.2	CV	N	Y	III,5
125023.84+665525.4	18.7	84.579‡	CV/EC	N	N	II,5

...continued on next page.

Table 6.1 continued.

SDSSJ	g	$P_{\rm orb}$ [min]	Type	WD	RASS	Reference
132723.38+652854.3	17.8	196.772±0.089	NL/EC	N	N	II,31
133941.11+484727.5	17.6	82.524±0.024	CV	Y	N	IV,32
143317.78+101123.3	18.6	78.107‡	CV/EC	Y	N	IV,20
150137.22+550123.3	19.4	81.851	CV/EC	Y	N	III,20
150240.97+333423.8	17.6	84.830‡	CV/EC	N	N	V,20
150722.33+523039.8	18.3	66.612‡	CV/EC	Y	N	IV,20,33
153817.35+512338.0	18.6	93.11±0.09	CV	N	N	III,12
154104.67+360252.9	19.7	84.3±0.3	AM	N	N	IV,22
155331.11+551614.4	18.5	263.48±0.06	AM	N	N	II,33
155531.99-001055.0	19.4	113.54±0.03	CV/EC	N	N	1,3
155644.23-000950.2	18.1	106.68±0.01	DN	Y	N	I,6
155656.92+352336.6	18.4	128	CV/EC	N	N	V
160745.02+362320.7	18.1	226±	NL/EC	N	N	V,12
161033.63-010223.3	19.1	80.52±0.08	CV	Y	N	I,33
162936.53+263519.5	19.3	134±2	AM	N	N	IV,22
163722.21-001957.1	20.6	96.98±0.22	DN	N	N	I,2
164248.52+134751.4	18.6	111±2	CV	N	N	VI,2
165658.13+212139.3	18.5	90.89±0.15	CV	N	Y	IV,17
165837.70+184727.4	20.1	98.06±0.06	CV	N	N	V,2
170053.29+400357.6	19.4	116.355‡	AM	N	Y	II,11
170213.25+322954.1	17.9	144.118‡	DN	N	N	III,34,35
171145.08+301319.9	20.3	80.35±0.05	CV	Y	N	III,5
173008.38+624754.7	16.3	110.22±0.12	DN	N	N	1,36
204448.91-045928.7	16.9	2420±14	CV	N	N	II,37
204817.85-061044.8	19.4	87.49±0.32	CV	Y	N	II,12,38
205017.83-053626.7	18.1	94.211‡	AM	N	Y	II,6,39,40
205914.87-061220.5	18.4	107.52±0.14	DN	N	N	II,3
210449.95+010545.9	20.4	103.62±0.12	DN	N	N	II,3
211605.43+113407.3	15.3–	80.2±2.2	DN	N	N	III,5
215411.12-090121.6	19.2	319±3	CV	N	N	II,5
220553.98+115553.7	20.1	82.81±0.09	CV	Y	N	II,41
223439.93+004127.2	18.1	127.29±0.25	CV	N	N	II,12
230351.64+010651.0	19.1	110.51±0.24	DN	N	Y	1,12
233325.92+152222.2	18.7	83.39±0.08	IP	N	N	V,42

[1] Southworth et al. 2008a in prep; [2] Southworth et al. 2008b in prep; [3] Southworth et al. (2007b); [4] Pretorius et al. (2004); [5] Dillon et al. (2008); [6] Woudt et al. (2004); [7] Schmidt et al. (2005c); [8] O'Donoghue et al. (2006); [9] Southworth et al. (2006); [10] Ak et al. (2005); [11] Homer et al. (2005); [12] Dillon et al. in prep; [13] Pavlenko et al. (2007); [14] Shears et al. (2007b); [15] Zharikov et al. (2008); [16] Rodríguez-Gil et al. (2007a); [17] Thorstensen et al. in prep; [18] Thorstensen et al. (2004); [19] Boyd et al. (2007); [20] Littlefair et al. (2008), submitted[21] Woudt et al. (2005); [22] this work; [23] Homer et al. (2006a); [24] Schmidt et al. (2007); [25] Littlefair et al. (2006b); [26] Schmidt et al. (2005b); [27] Burleigh et al. (2006); [28] Farihi et al. (2008); [29] Shears et al. (2007a); [30] Zharikov et al. (2006); [31] Wolfe et al. (2003); [32] Gänsicke et al. (2006); [33] Littlefair et al. (2007); [32] Szkody et al. (2003b); [33] Woudt & Warner (2004); [34] Littlefair et al. (2006a); [35] Boyd et al. (2006); [36] Patterson et al., in prep [37] Peters & Thorstensen (2005) [38] Woudt et al. (2005); [39] Potter et al. (2006); [40] Homer et al. (2006b); [41] Southworth et al. 2008c in press [42] Southworth et al. (2007a)

Table 6.2: Previously known CVs (*old SDSS CVs*), which were spectroscopically re-identified by SDSS. The definition of the colums are the same as in Table 6.1.

SDSSJ	Other Name	SDSS g	$P_{\rm orb}$ [min]	Type	WD	RASS	Reference
002728.01-010828.5	EN Cet	20.7	85.44±0.07	DN	Y	N	IV,1
075117.32+144423.9	PQ Gem	14.2	311.56±0.04	IP	N	Y	V,2
075853.03+161645.1	DW Cnc	15.3	86.1015±0.0003	IP	N	N	V,3,4
082236.03+510524.5	BH Lyn	15.3	224.460‡	NL/EC	N	N	I,5,6,7,8
083619.15+212105.3	CC Cnc	16.8	105.86±0.07	DN	N	Y	V,9
083642.74+532838.0	SW UMa	16.9	81.8136±0.001	DN	N	Y	I,10,11
084303.98+275149.6	EG Cnc	18.9	85.5±0.9	DN	Y	N	IV,12,13
085344.16+574840.5	BZ UMa	16.4	97.8	DN	N	Y	II,14
085414.02+390537.2	EUVE J0854+390	19.2	113.26±0.03	AM	N	Y	IV,1
085909.18+053654.5	RX J0859.1+0537	18.6	143.8	AM	N	Y	IV,16
090950.53+184947.4	GY Cnc	16.4	252.637‡	DN/EC	N	Y	VII,17,18
093214.82+495054.7	1H 0928+5004	17.5	602.4	NL/EC	N	N	V,19
093836.98+071455.0	PG 0935+075	18.3	269.0±0.4	DN	N	N	IV,20
094431.71+035805.5	RXJ 0944.5+0357	16.8	214.4±0.2	DN	N	Y	II,19,21,22
094636.59+444644.7	DV UMa	19.4	123.628‡	DN/EC	N	N	IV,23,24,25
101534.67+090442.0	GG Leo	17.2	79.790‡	AM	N	Y	IV,26
101947.26+335753.6	HS 1016+3412	18.4	92.22±0.17	DN	N	Y	VI,27
102026.52+530433.1	KS UMa	17.4	97.86±0.14	DN	N	Y	III,21,28
102320.27+440509.8	NSV 4838, UMa 8	18.8	97.6	DN	N	N	IV,19
102347.67+003841.2	FIRST J102347.6+003841	18.0	285.255±0.001	CV:	N	N	II,29,30,31
104356.72+580731.9	IY UMa	17.7	106.429‡	DN/EC	N	N	VII,32,33,34
105135.14+540436.0	EK UMa	18.4	114.5±0.2	AM	N	N	IV,35
105430.43+300610.1	SX LMi	16.8	96.72±0.16	DN	N	Y	VI,36,37
105656.99+494118.2	CY UMa	17.8	100.18±0.06	DN	N	N	IV,38,39
110425.64+450314.0	AN UMa	15.8	114.844‡	AM	N	N	V,40,41
110539.76+250628.6	ST LMi	17.6	113.8882±0.0001	AM	Y	Y	VII,42
111544.56+425822.4	AR UMa	15.6	115.921‡	AM	N	N	V,43,44

...continued on ne xt page.

Table 6.2 continued.

SDSSJ	Other Name	SDSS g	P_{orb} [min]	Type	WD	RASS	Reference
113122.39+432238.5	RX J1131.3+4322, MR UMa	16.2	91.25±0.12	DN	N	N	V,45
113722.24+014858.5	RZ Leo	18.7	109.6±0.2	DN	Y	Y	II,28
113826.82+032207.1	T Leo	14.9	84.699‡	DN	N	Y	II,46
114955.69+284507.3	EU UMa	17.9	90.14±0.02	AM	N	Y	VII,47
115215.82+491441.8	BC UMa	18.5	90.16±0.06	DN	Y	N	III,28
125637.10+263643.2	GO Com	18.3	95±1	DN	N	Y	VII,48,49,50
130753.86+535130.5	EV UMa	16.5	79.687‡	AM	N	Y	IV,51,52
134323.16+150916.8	HS 1340+1524	17.6	92.66±0.17	DN	N	Y	VII,27
143500.21-004606.3	OU Vir	18.6	104.697‡	DN/EC	N	N	I,53,54
151302.29+231508.4	NY Ser	16.4	140.4±0.3	DN	N	N	VII,28,55
152613.96+081802.3	QW Ser	18.1	107.3±0.1	DN	N	N	VII,28
155247.18+185629.1	MR Ser	17.2	113.4689±0.0001	AM	N	Y	VII,56
155412.33+272152.4	RX J1554.2+2721	17.6	151.865±0.009	AM	N	Y	VI,57,58
155654.47+210718.8	QZ Ser	17.9	119.752±0.002	DN	N	N	VI,59
161007.50+035232.7	RX J1610.1+0352	17.7	190.54±0.06	AM	N	Y	VII,60,61
162501.74+390926.3	V844 Her	17.2	78.69±0.01	DN	N	Y	IV,62
223843.84+010829.7	Aqr 1	18.3	194.30±0.16	IP	N	Y	II,29

[1] Dillon et al. (2008); [2] Hellier et al. (1994); [3] Rodríguez-Gil et al. (2004); [4] Patterson et al. (2004); [5] Thorstensen et al. (1991a); [6] Dhillon et al. (1992); [7] Hoard & Szkody (1997); [8] Stanishev et al. (2006); [9] Thorstensen (1997); [10] Howell & Szkody (1988); [11] Shafter et al. (1986); [12] Patterson et al. (1998b); [13] Kato et al. (2004); [14] Ringwald et al. (1994); [16] Reinsch, priv. comm.; [17] Gänsicke et al. (2000); [18] Feline et al. (2005); [19] Thorstensen, priv. comm.; [20] Thorstensen & Taylor (2001); [21] Jiang et al. (2000); [22] Mennickent et al. (2002); [23] Howell et al. (1988); [24] (Patterson et al., 2000b); [25] Feline et al. (2004a); [26] Burwitz et al. (1998); [27] Aungwerojwit et al. (2006); [28] Patterson et al. (2003); [29] Woudt et al. (2004); [30] Thorstensen & Armstrong (2005); [31] Homer et al. (2006a); [32] Uemura et al. (2000); [33] (Patterson et al., 2000a); [34] Steeghs et al. (2003); [35] Morris et al. (1987); [36] Nogami et al. (1997); [37] Wagner et al. (1998); [38] Martinez-Pais & Casares (1995); [39] Thorstensen et al. (1996); [40] Liebert et al. (1982); [41] Bonnet-Bidaud et al. (1996); [42] Cropper (1989); [43] Remillard et al. (1994); [44] Schmidt et al. (1999); [45] Patterson et al. (2005); [46] Shafter & Szkody (1984); [47] Howell et al. (1995a); [48] Howell et al. (1995b); [49] Howell et al. (1990); [50] Howell, priv. comm.; [51] Osborne et al. (1994); [52] Katajainen et al. (2000); [53] Vanmunster et al. (2000); [54] Feline et al. (2004b); [55] Nogami et al. (1998); [56] Schwope et al. (1991); [57] Tovmassian et al. (2001); [58] Thorstensen & Fenton (2002); [59] Thorstensen et al. (2002a); [60] Schwope et al. (2002); [61] Rodrigues et al. (2006); [62] Thorstensen et al. (2002c);

6.3 The Orbital Period Distribution of the SDSS CVs

The fibre allocation of SDSS does not make use of astronomical catalogues such as Simbad, and hence the selection of targets for spectroscopic follow-up is independent of previous knowledge. From this point forward the following nomenclature will be adopted. The term **SDSS CVs** will refer to all CVs for which an SDSS spectrum that allows their identification as a CV is available in Data Release 6 (DR6, Adelman-McCarthy et al. 2007), independently of whether they were already known before or not. **New SDSS CVs** will refer to those systems that were genuinely identified from SDSS spectroscopy, and **old SDSS CVs** those systems which were known to be CVs beforehand, and are re-found among the SDSS spectra. Finally, **non-SDSS CVs** will refer to all CVs from V7.6 of the Ritter & Kolb 2003 catalogue which have *no* spectrum in SDSS DR6, excluding the systems which were flagged as having an uncertain orbital period value. The four different samples contain 455 (non-SDSS CVs), 116 (SDSS CVs), 72 (new SDSS CVs) and 44 (old SDSS CVs) systems.

Figure 6.1 compares the orbital period distribution of 455 non-SDSS CVs and that of 116 SDSS CVs. The well-known features of the non-SDSS CV population are the deficiency of systems in the 2–3 h period gap, roughly equal numbers of systems above and below the gap, a minimum period near 80 min, and a drop-off of systems towards longer periods above the gap. In numbers, the non-SDSS CV sample contains 168, 48, and 239 systems with $P_{\rm orb} \leq 2\,{\rm h}$, $2\,{\rm h} \leq P_{\rm orb} \leq 3\,{\rm h}$, and $P_{\rm orb} > 3\,{\rm h}$, respectively.

The period distribution of the SDSS CVs looks radically different compared to that of the non-SDSS CVs. The majority of the systems are found below the period gap, with 78, 12, and 26 systems below, in, and above the 2–3 h period gap, respectively, confirming the trend already noticed by Southworth et al. (2006, 2007b); Szkody et al. (2007a). The most striking feature is an apparent accumulation of systems in the shortest-period bin. Comparing the orbital period distributions of the old SDSS CVs and the new SDSS CVs sample (Figure 6.1, lower panel) indicates that the distribution of the old SDSS CVs is flat below the period gap, and that the ”spike” at the orbital period minimum comes entirely from the new CVs identified by SDSS.

Cumulative period distributions of the non-SDSS CVs, the old SDSS CVs, and the new SDSS CVs are shown on a linear scale in orbital period in Figure 6.2. The large number of new CVs in the range $\sim 80 - 86\,{\rm min}$ is evident from the steep slope of period distribution of the new

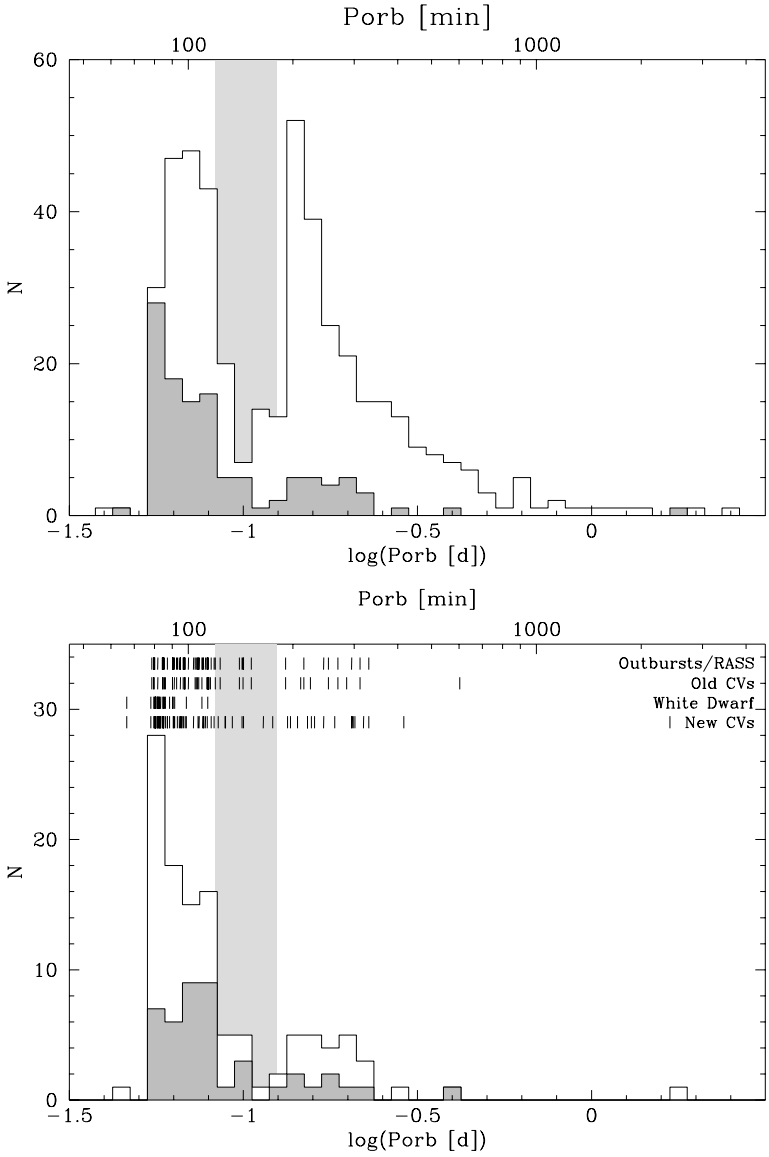

Figure 6.1: *Top panel*: The orbital period distribution of 455 CVs from Ritter & Kolb (2003), V7.6, which have no spectroscopic observation in SDSS DR6 (white) and the distribution of 116 SDSS CVs from Table 6.1 & 6.2 (*SDSS CVs*, grey). These distributions exclude the hydrogen-deficient AM CVn systems. *Bottom panel*: the period distribution of the SDSS CVs divided into 44 previously known systems (*old SDSS CVs*, grey) and 72 newly identified CVs (*new SDSS CVs*, white). Superimposed are tick marks indicating the individual orbital periods of the old and new SDSS CVs, along with the periods of SDSS CVs showing outbursts and/or being detected in the ROSAT All Sky Survey, and the distribution of the periods of the SDSS CVs which clearly reveal the white dwarf in their optical spectra.

SDSS CVs. A two-sided Kolmogorov-Smirnov (KS) test was applied in order to test whether the three cumulative distributions deviate from one another in a statistically significant way. The lower limit, was set at 76.78 min, corresponding to the shortest-period "standard" hydrogen-rich CV, GW Lib[3]. The upper period limit for the KS test was set to 120 min, corresponding to the lower edge of the period gap. The reason for this choice is that CVs with periods above the gap have substantially brighter absolute magnitudes compared to the short-period systems, and hence SDSS, sampling the sky at high galactic latitudes, $|b| > 30°$, will be biased against the detection of long-period CVs[4]. In fact, a substantial fraction of previously known CVs contained in the SDSS area are saturated in the SDSS imaging data, and consequently did not get a spectroscopic fibre for follow-up.

The KS test comparing the cumulative period distributions of the non-SDSS CVs and the new SDSS CVs results in a 0.9% probability that the two distributions are randomly drawn from an identical parent population, which shows that the period distribution of the new SDSS CVs differs significantly from that of the previously known CV sample. This clearly suggests that the CV identification within SDSS differs from the average CV discovery method in the previously known sample.

Conversely, comparing the cumulative period distributions of the non-SDSS CVs and the old SDSS CVs, the probability for both distributions emanating from the same parent sample is 63.0%, i.e. the two distributions are identical from a statistical point of view. This is little surprising, as the old SDSS CVs have been identified by the same methods as the non-SDSS CVs, i.e. primarily dwarf nova outbursts and X-ray emission.

In conclusion, the orbital period distributions of the new SDSS CVs and that of the previously known CVs (independently whether or not also selected by SDSS for spectroscopic follow-up) differ significantly, most apparently in the ratio of the number of short and long period systems, and in the appearance of a spike at $\sim 80 - 86$ min in the period distribution of the new

[3]Three hydrogen-rich CVs with orbital periods around 60 min are known: V485 Cen, EI Psc, and SDSS J1507+5230. The evolutionary state of these systems is not entirely clear; EI Psc contains an evolved donor star (Thorstensen et al., 2002b), and SDSS J1507+5230 most likely formed with a brown dwarf donor (Littlefair et al., 2007). For the discussion of the SDSS CV period distribution, these three oddball systems were excluded.

[4]Examples of luminous CVs above the period gap are TT Ari, with $P_{\rm orb} = 198.07$ min, $V \simeq 10.6$, and $d = 335 \pm 50$ pc (Thorstensen et al., 1985; Gänsicke et al., 1999), and MV Lyr with $P_{\rm orb} = 191.4$ min, $V \simeq 12.0$, and $d = 505 \pm 50$ pc (Skillman et al., 1995; Hoard et al., 2004), corresponding to absolute magnitudes of $M_V = 3.0 \pm 0.3$ and $M_V = 3.5 \pm 0.2$, respectively. At $|b| = 30°$, SDSS could detect these systems out to > 10 kpc above the galactic disc. See Section 6.5 for details on the sky volume coverage of SDSS.

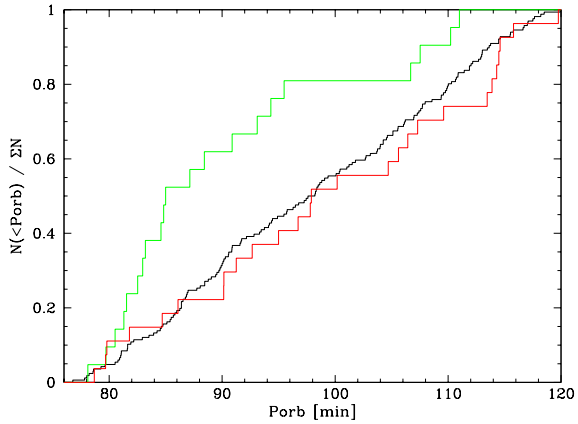

Figure 6.2: Normalised cumulative period distributions in the range $P_{\rm orb} = 76 - 120$ min of (a) 455 CVs from Ritter & Kolb (2003; V7.6), excluding systems with spectroscopy in SDSS DR6 and systems whose periods are marked as uncertain (black), (b) 44 previously known CVs recovered from SDSS spectroscopy (red, dashed), and (c) 72 new CV identified from SDSS spectroscopy (green). A two-sided Kolmogorov-Smirnov comparing the distributions of the non-SDSS CVs and the new SDSS CVs results in a 0.9% probability for the two distributions being drawn from the same parent population. In contrast, the probability that the non-SDSS CVs and the previously known SDSS CVs are drawn from the same sample is 63.0%.

SDSS CVs.

6.4 Properties of the Period-Spike CVs found by SDSS

As shown in Section 6.3, the orbital period distributions of the non-SDSS CVs and the new SDSS CVs differ at a 3-σ level. This raises the question of whether the new SDSS CVs also differ in other properties beyond their orbital period from the non-SDSS CVs. For the discussion below, the following three Boolean characteristics are defined: (a) the white dwarf is clearly visible in the SDSS identification spectrum, (b) X-ray emission has been detected in the ROSAT All Sky Survey (RASS, Voges et al. 2000)[5], and (c) an optical outburst has been observed[6]. Tables 6.1 and 6.2 list these three properties for the 116 SDSS CVs with accurate orbital period measurements. Below, the detection of the white dwarf in the optical spectrum will be interpreted as

[5]While a number of SDSS CVs have been detected in pointed ROSAT observations, we restricted our assessment of X-ray emission to a detection in the RASS, as inclusion of pointed observations would imply wildly different X-ray flux limits for random lines-of-sight.

[6]Information on large-amplitude variability has been drawn from three sources of information. (1) Brightness differences between the SDSS imaging and spectroscopic data, (2) individual follow-up observations which caught some systems in outburst (e.g. Tramposch et al., 2005; Dillon et al., 2008; Southworth et al., 2007b), and from the mailing lists of the amateur astronomers (vsnet, cvnet, baavss).

evidence for a low mass transfer rate, and the detection of X-rays/outbursts as evidence of accretion activity which may lead to the identification of a system as a CV.

In Figure 6.3, the properties of the SDSS CVs can be visualised in form of a three-set Venn-diagram, dividing them into systems with (1) $P_{\rm orb} \leq 86$ min (i.e. within the period spike), (2) systems which reveal the white dwarf in the SDSS identification spectrum, and (3) systems which were detected in X-rays and/or outburst. The numbers for the previously known systems are given in brackets. An immediate result from inspection of Figure 6.3 is that all the previously known systems show outburst activity, whereas 22 of the new SDSS CVs have not been detected in the RASS and have not been detected in outburst so far.

Figure 6.3 clearly illustrates that a large fraction (18/30) of the systems with orbital periods in the 80–86 min spike have optical spectra dominated by the white dwarf. This generally indicates that the accretion disc and secondary star are dim and hence that the donor star is of a late spectral type and that the mass transfer rate is low. Of the systems not revealing their white dwarfs, seven exhibit accretion activity, which is (on average) indicative of somewhat higher mass transfer rates than in the white-dwarf dominated systems, and result in the white dwarf being outshone by the accretion disc/stream. In fact, five of these seven systems were discovered because of their outbursts or X-ray emission (SW UMa, GG Leo, T Leo, EV UMa, and V844 Her). The remaining two are the polar SDSS J1541+2721 and the dwarf nova SDSS J2116+1134. In magnetic CVs, the white dwarf is typically not detected during states of active accretion, SDSS J1250+6655 is an eclipsing system, where the white dwarf may be veiled, and the spectrum of SDSS J2116+1134 is too poor to make a definite judgment on the presence of broad white dwarf absorption lines.

The very distinct spectral appearance between the CVs with $P_{\rm orb} \leq 86$ min which are accretion-active and those which are accreting at a much lower rate, is demonstrated in Figure 6.4, where four representative spectra from each group are shown. Clearly, the four old (accretion-active) SDSS CVs EV UMa, SW UMa, T Leo, and V884 Her have strong Balmer and He I emission lines, or He II in the case of the polar EV UMa. These four systems have been identified as an X-ray emitter (EV UMa) and outbursting dwarf novae (SW UMa, T Leo, V884 Her). The four white-dwarf dominated new SDSS CVs (SDSS J1501+5501, SDSS J1238–0339, SDSS J1610–0102, and SDSS J1035+0551) have moderate to weak Balmer emission lines

with a steep decrement, and hardly any He I line, indicating lower temperatures and emission measures in their accretion flows than in the accretion-active CVs. SDSS J1501+5501 and SDSS J1035+0551 have extremely low-mass brown dwarf donor stars (Littlefair et al., 2006b, 2008), indicating that they are probably highly evolved CVs, and the white dwarf in SDSS J1610–0102 exhibits ZZ Ceti pulsations (Woudt & Warner, 2004), which implies a relatively cool white dwarf and a low secular mean accretion rate (Townsley & Bildsten, 2003; Arras et al., 2006).

In addition to the eight accretion-active CVs where the white dwarf cannot be detected in their SDSS spectra, there are another four systems that fail to reveal the white dwarf and have also not been detected in X-rays and/or outburst. Two of these systems are eclipsing (SDSS J0903+3300, and SDSS J1502+3334). Given that the strength of emission lines correlates with the inclination (Warner, 1986), the white dwarf Balmer absorption lines are likely to be filled in by emission from the optically thin accretion flow and/or the white dwarf might be veiled by the accretion disc altogether (Horne et al., 1994; Knigge et al., 2000). The other two systems are magnetic CVs (SDSS J1031+2028 and SDSS J2333+1522), where the white dwarf is typically not seen during accretion-active phases.

Of particular interest are the four systems with $P_{\rm orb} \leq 86$ min which are accretion-active, and do reveal the white dwarf in their optical spectra: the two previously known systems EG Cnc (a well-studied WZ Sge-type dwarf nova) and EN Cet (a poorly studied dwarf nova), and the two new SDSS dwarf novae SDSS J0137-0912 (with a single observed superoutburst) and SDSS J0804+5103 (a WZ Sge dwarf novae with the first outburst observed in March 2005). All four systems are characterised by long outburst recurrence times, which is a signature of CVs with low mass transfer rates, and consistent with the detection of their white dwarfs in the SDSS spectra.

A final note on Figure 6.3 is that only 7 out of 86 SDSS CVs with $P_{\rm orb} > 86$ min have white-dwarf dominated optical spectra, confirming that the detection of the white dwarf is indeed a spectroscopic fingerprint of the shortest period CVs.

In summary, it appears that nearly half of the 30 SDSS CVs in the 80–86 min period spike are newly discovered systems with white-dwarf dominated optical spectra and no easily noticeable accretion activity. These systems are most likely all WZ Sge-type dwarf novae with

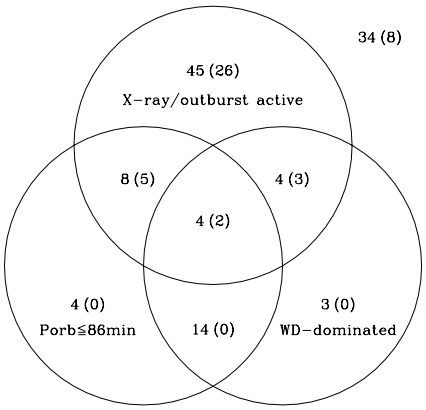

Figure 6.3: Venn diagram showing the distribution of 82 SDSS CVs with accurate orbital periods (Tables 6.1 & 6.2) into the following three categories: '$P_{\rm orb} \leq 86$ min', 'has outbursts and/or has been detected in the ROSAT All Sky Survey', and 'its optical spectrum is dominated by the white dwarf'. The numbers in brackets refer to the properties of the previously known CVs that were re-identified by SDSS. Not all the systems from Tables 6.1 are represented in this diagram: 34 additional SDSS CVs from Tables 6.1 & 6.2 have $P_{\rm orb} > 86$ min, do not exhibit the white dwarf in their SDSS spectra, and not been detected in the RASS, and have not been seen in outburst.

extremely long recurrence times, with SDSS J0804+5103 being so far the only white-dwarf SDSS CV outing itself as a WZ Sge type system.

For completeness, two additional properties of SDSS CVs with periods below 86 min should be mentioned: (1) All of the confirmed non-radial white dwarf pulsators identified by SDSS for which orbital periods have been measured reside within the 80–86 min period spike (Woudt & Warner, 2004; Woudt et al., 2005; Gänsicke et al., 2006; Nilsson et al., 2006; Mukadam et al., 2007), which suggests rather low mass transfer rates, as the white dwarfs have to be cool enough to drive pulsations (Townsley & Bildsten, 2003; Arras et al., 2006). (2) Three of the four SDSS CVs with a confirmed brown-dwarf donor are located within the period spike (SDSS J1035+0551, SDSS J1433+1011, and SDSS J1501+5501, Littlefair et al. 2006b, 2008)[7]; these are probably CVs that have evolved past the period minimum.

[7]The fourth confirmed brown dwarf donor has been found in SDSS J1507+5230 (Littlefair et al., 2007), which has been excluded from the discussion in this paper as it has an orbital period of 66.6 min, way below the period minimum for 'standard' hydrogen-rich CVs.

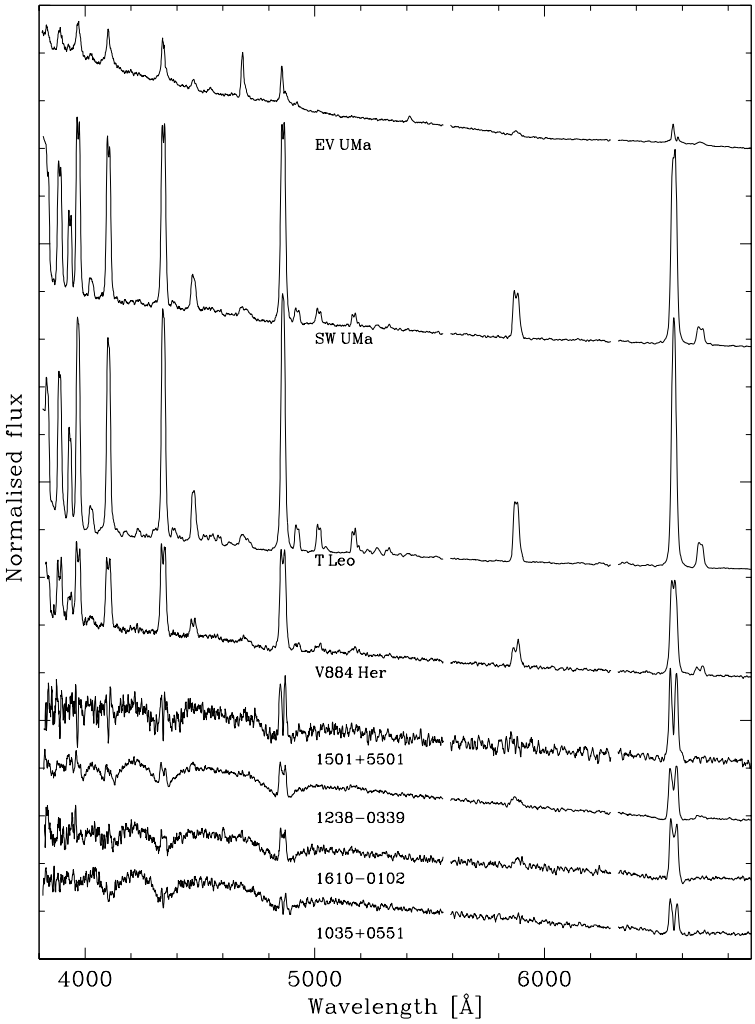

Figure 6.4: SDSS CVs with periods below 86 min. The top four objects are previously known systems re-identified by SDSS (*old SDSS CVs*, Table 6.2), the bottom four spectra are new identifications (*new SDSS CVs*, Table 6.1).

6.5 Discussion

In Section 6.3, it was shown that the period distribution of the SDSS CVs differs dramatically from that of the previously known CVs, with a substantially larger fraction of below-the-gap to above-the-gap systems, and a significant accumulation of CVs at the orbital period minimum. More specifically, the origin of the 80–86 min period spike is entirely due to the new CVs identified in SDSS, and, as outlined in 6.4, the systems in the period spike differ also in spectral morphology and accretion activity from the longer period CVs. The following section provides a brief discussion as to why the CVs in the SDSS sample differs so clearly from the previously known systems, in particular the effects of survey depth and CV candidate selection.

6.5.1 Deep, Deeper, the Deepest

One very obvious difference between the SDSS CVs and CV samples from previous surveys is the unrivalled depth of Sloan. Hence, SDSS should be able to identify systems that were intrinsically too faint, or at too large a distance, for the previous surveys. This raises the question *does SDSS find more short period CVs than previous surveys, such as the Palomar Green (PG) Survey or the Hamburg Quasar Survey, just because of its depth?* A full treatment of this question would require the computation of a galactic model of the CV population, and fold that through the details of the sky coverage, magnitude limit, and colour cuts of the considered surveys (see Pretorius et al. 2007a for an analysis of this kind for the Palomar Green survey). Given the intricate allocation algorithms for spectroscopic fibres within SDSS, this task is beyond the scope of the present work. For simplicity, we develop here an empirical comparison between SDSS, the Hamburg Quasar Survey (HQS), and the PG survey, using their *effective survey volumes* for the white-dwarf dominated systems near the period minimum. The effective survey volume is calculated by integrating over a spherical cap in galactic coordinates covering galactic latitudes higher than $|b_{\rm lim}|$, weighting the volume by an exponential drop-off in the space density of CVs along the z-axis, with a scale height H_z. We assume radial symmetry around the z-axis in both the distribution of CVs and the coverage of the survey. More realistic work would need to account for the dependence of the CV space density on galactic longitude, plus the exact tiling of the different surveys, as none of them covers the full spherical cap. Finally, the effective

Table 6.3: Comparison of the SDSS, HQS, and Palomar Green Survey in terms of their potential for discovering period-minimum CVs. The first three columns give the magnitude limit, sky coverage, and galactic latitude range for the three surveys. For SDSS, we defined sub-samples with different limiting magnitudes. $g_{\rm lim} = 22.5$ corresponds to the full CV sample, $g_{\rm lim} = 19.0$ includes all CVs within the magnitude limit of the low-redshift quasar survey, and $g_{\rm lim} = 17.4$ and $g_{\rm lim} = 16.1$ are selected to compare SDSS like-for-like with the HQS and the PG survey. From these characteristics, we calculated an effective survey volume for white-dwarf dominated CVs as outlined in Section 6.5. The survey volumes were calculated for two different assumptions of the scale height, H_z, of the CV population, and normalised to the volume of the SDSS low-redshift quasar survey ($g_{\rm lim} = 19.0$). The last two columns give the number of all CVs with $P_{\rm orb} \leq 86$ min found in the three surveys, and the number of period-minimum CVs with white-dwarf dominated spectra. Numbers following a "/" are normalised to the SDSS values for $g_{\rm lim} = 19.0$. Sixteen white-dwarf dominated CVs from SDSS have no orbital period measurement yet. From Figure 6.3, there is a $\sim 80\%$ chance that they have periods $P_{\rm orb} \leq 86$ min. We include below in brackets the numbers obtained under the most extreme assumption, i.e. that all 16 are period-minimum CVs.

Survey	$g_{\rm lim}$	$d_{\rm lim}$	Area	$\|b\|$	$V_{\rm norm}$		$N_{\rm CV}(P_{\rm orb} \leq 86\,{\rm min})$	
		[pc]	[deg^2]		$H_z = 190$ pc	$H_z = 260$ pc	all CVs	wd-dominated
SDSS	22.5	1514	6400	$> 30°$	1.36	4.11	30/1.50 (46/2.09)	18/1.80 (34/2.83)
	19.0	302			1.00	1.00	20/1.00 (22/1.00)	10/1.00 (12/1.00)
	17.4	145			0.24	0.20	5/0.20	0/0.00
	16.1	79			0.05	0.04	1/0.0	0/0.00
HQS	17.4	145	13600	$> 20°$	0.50	0.40	6/0.27	1/0.08
PG	16.1	79	10714	$> 30°$	0.08	0.05	3/0.14	1:/0.08

volume is weighted by the survey area. The scale height is a poorly determined parameter, and we will assume two different values, $H_z = 190$ pc and $H_z = 260$ pc (Patterson, 1984; Pretorius et al., 2007a). We start with an estimate of the absolute magnitudes of the period minimum CVs, which we need to turn the magnitude limits of the surveys into distance limits, followed by a brief summary of the survey characteristics, and then delve into the actual comparison of their results in terms of CV discoveries.

Absolute magnitudes of the period minimum CVs

Unfortunately, the absolute magnitudes of CVs are notoriously poorly determined, as there are too few systems with accurate distance determinations to carry out a reliable bolometric calibration. With this caveat in mind, we will now compare the absolute magnitudes of the white-dwarf dominated CVs found by SDSS to those of the previously known systems with $P_{\rm orb} \leq 86$ min.

Among the 7 old SDSS CVs with $P_{\rm orb} \leq 86$ min (Table 6.2), there is just one system with a trigonometric parallax, the dwarf novae T Leo (Thorstensen, 2003). From $d = 101^{+13}_{-11}$ pc and $g = 14.9$ we find $M_g = 9.9 \pm 0.3$. For SW UMa and EG Cnc spectral modelling of the white

dwarf in ultraviolet *HST*/STIS spectra resulted in distance estimates of $d = 159 \pm 22$ pc and $d = 420 \pm 65$ pc, respectively, which results in $M_g = 10.9$ and $M_g = 10.8$, respectively. Taking the average over these three systems, we find $M_g = 10.5 \pm 0.5$[8].

Distance estimates are available for 13 of white-dwarf dominated new SDSS CVs in the period-minimum spike: six from modelling high-speed light curves (Littlefair et al., 2008), four from modelling the optical SDSS spectra (Gänsicke et al., 2006; Mukadam et al., 2007), and three from modelling combined optical SDSS plus ultraviolet *HST*/ACS spectra (Szkody et al., 2007b). The resulting absolute magnitudes range from $M_g = 10.5 - 13.1$, with an average of $< M_g >= 11.6 \pm 0.7$. The large spread is likely to be caused by the systematic uncertainties inherent to the distance determinations, rather than substantial intrinsic differences in the system properties. An independent check on these values can be obtained by considering that the white dwarfs in these systems have typically $T_{\rm eff} \simeq 12000 - 15000$ K (Gänsicke et al., 2006; Mukadam et al., 2007; Littlefair et al., 2008). Assuming an average mass of $0.85\,M_\odot$ (Littlefair et al., 2008), and using an updated version of the photometric white dwarf calibrations by Bergeron et al. 1995), we obtain $M_g = 11.8 - 12.2$ for the white dwarfs alone. Given that, by definition, the white dwarf is dominating the optical spectrum in these systems, adding a maximum of 50% accretion luminosity to the brightness results in $M_g = 11.7 - 11.3$ for the bulk of the new SDSS CVs in the period minimum spike, entirely consistent with our estimate of $< M_g >= 11.6 \pm 0.7$.

While not statistically significant, the absolute magnitudes derived above suggest that the new SDSS CVs are on average intrinsically fainter than the old SDSS CVs, which is not too surprising as the mere fact that the white dwarf is the dominant source of light implies that the accretion luminosity is low. It is interesting to compare our numbers here with the work of Patterson (1998), who estimated time-averaged absolute magnitudes for a large number of CVs, finding a nearly flat distribution between $M_V = 4 - 11$, with a sharp cut-off for fainter systems. The faintest bin in Patterson's (1998) Figure 2 is populated only by a handful of WZ Sge type dwarf novae, and it is in that bin that the white dwarf dominated CVs (which are presumably all WZ Sge type dwarf novae) will slot in. However, Patterson's (1998) statement *"...with not a single star fainter than* $< M_v >= 11.6$*"* still holds, as no system significantly fainter than that

[8]For completeness, the polars EV UMa and GG Leo have lower limits on their distances, $d \gtrsim 705$ pc and $d > 100$ pc (Osborne et al., 1994; Burwitz et al., 1998), which give $M_g \lesssim 7.3$ and $M_g \lesssim 12.2$, respectively. However, such lower limits on distances are very uncertain due to the possible contamination by cyclotron emission, and we do not include these two systems into our consideration above.

limit has been found by SDSS.

Sloan Digital Sky Survey

SDSS covers high galactic latitudes, $|b| > 30°$ (York et al., 2000). Within the main quasar search, spectroscopic follow-up is carried out on point-sources with non-stellar colours and a limiting magnitude of a (galactic column) dereddend $i = 19.1$ for ultraviolet excess / low-redshift quasars and of a dereddened $i = 20.2$ for high-redshift ($z \gtrsim 3$) quasars (Richards et al., 2002). The detailed fibre allocation algorithm is complex (see Section 6.5.3 below), and we will assume for the moment that the completeness in the follow-up of blueish CVs within the magnitude limits is as high as that for the targeted ultraviolet excess quasars ($\sim 90\%$, Schneider et al. 2007). Further, we assume a typical galactic reddening of $E(B-V) = 0.05$, which translates into a reddening correction in i of 0.1 mag, increasing the observed magnitude limited of the low-redshift quasar survey to $i = 19.2$. The white-dwarf dominated CVs have on average $< g - i > \simeq -0.2$, which leads to a limiting magnitude for such systems within the main quasar survey of $g \simeq 19.0$. Using $< M_g >= 11.6$ as determined above, this implies that SDSS should be able to serendipitously identify white-dwarf dominated systems out to $d = 302$ pc. Given that Szkody et al. (2007a) published some CVs beyond DR5, and we include here in addition to her lists (Szkody et al. 2002b to Szkody et al. 2007a) the previously known CVs within DR6, we assume 6400 deg^2 as the survey area for the spectroscopic SDSS data base , which is in between the official DR5 and DR6 areas.

Hamburg Quasar Survey

The Hamburg Quasar Survey (HQS) is another high-galactic latitude ($|b| > 20°$) survey covering 13 600 deg^2 with a typical limiting magnitude of $B = 17.5$. Using the colour transformations of Jester et al. (2005), the HQS had a limiting magnitude of $g \simeq 17.4$ for blue objects. Spectroscopic follow-up over the wavelength range 3400–5400 Å was obtained by means of Schmidt prism spectroscopy, which is hence complete except for plate artifacts or blends. About 50000 blue objects with $U - B \lesssim -0.5$ were extracted from the photographic plates and visually classified. Objects with Balmer emission lines were selected as CV candidates for detailed follow up (Gänsicke et al., 2002c; Aungwerojwit et al., 2006). Given the average colour of the white-dwarf

dominated CVs found in SDSS of $< u - g > \simeq 0.15$, the HQS should be able to identify such systems out to $d = 145$ pc.

Palomar Green Survey

The Palomar Green Survey (PG) extended over 10 714 deg^2 at galactic latitudes $|b| > 30°$ with spectroscopic follow-up for 1874 objects (Green et al., 1986). The survey design was a blue-cut of $U - B < -0.46$ and a typical limiting magnitude of $B < 16.1$. Comparison with SDSS data in overlapping areas showed however that the PG survey had a rather bluer cut of $U - B < 0.71$ (Jester et al., 2005). Using the colour transformation from Jester et al. (2005), the PG colour cut and limiting magnitude are $u - g < 0.3$ and $g = 16.1$. Hence the PG survey should be able to identify short-period CVs out to $d = 78$ pc.

Finding period-minimum CVs: A comparison of SDSS, HQS, and PG

Using the survey characteristics summarised above, we calculated the effective survey volumes for finding period-minimum CVs, as outlined in Section 6.5, for the SDSS, HQS, and PG survey. As we are only interested in the relative 'catchment area', we normalise all numbers to the effective volume of the main quasar survey within SDSS, i.e. to SDSS with a limiting magnitude of $g = 19.0$, and report the resulting numbers in Table 6.3. Along with the normalised effective volumes, we list in Table 6.3 the number of CVs with $P_{\rm orb} \leq 86$ min identified by each survey, and in a separate column the number of those period-minimum CVs in which the white dwarf is detected in their optical spectra. For the case of SDSS, we give three additional subsamples with the following limiting magnitudes: (a) $g_{\rm lim} = 22.5$, which is the magnitude of the faintest SDSS CV, resulting in the most inclusive sample of systems, and (b) $g_{\rm lim} = 17.5$ and $g_{\rm lim} = 16.1$, which will allow us to investigate how SDSS compares with the HQS and the PG survey if operating at the same limiting magnitude.

The first thing to note is that the difference in effective survey volumes depends only mildly on the different assumption for the scale height, the reason being that both HQS and PG are so shallow that they do not even extend beyond one scale height, and hence do not feel much of the exponential drop-off in the CV space density.

SDSS beats the HQS in terms of survey volume only by about a factor two, which is due

to the HQS covering more than twice the area on the sky, and extending down to lower galactic latitudes. While the number of period-minimum CVs found in the HQS is only slightly below the expectation from simply scaling the survey volume, it has only produced one white-dwarf dominated CV (V445 And, Araujo-Betancor et al. 2005c), which is far below the expectations from its survey volume, suggesting a selection effect against the detection of such systems. Gänsicke et al. (2002c) showed that the HQS is very efficient in finding short period CVs similar to those known in the late 1990s, if they had Hβ equivalent widths in excess of $\sim$ 10 Å. Those were mostly CVs with substantial accretion luminosity, such as SW UMa or T Leo, as only very few white-dwarf dominated CVs were known at that time then. However, Gänsicke et al. (2002c) noted that the results from the HQS *"...exclude the presence of a large population of nearby infrequently outbursting X-ray faint short-period CVs unless they have significantly weaker emission lines than, e.g., WZ Sge"* . It turns out that those types of systems, short-period CVs with no or very rare outbursts, no or very weak X-ray emission, and weak Hβ equivalent widths are frequent among the CV catch of the SDSS (Figure 6.4). The difficulty in finding that type of system in HQS was exacerbated by the low spectral resolution, averaging over the broad white dwarf absorption lines and the weak emission lines, and thus even further decreasing the net equivalent widths of the Balmer emission.

Comparing SDSS and the PG survey, the numbers of short-period CVs found are roughly in line with the expectations from the scaled survey volumes – only three CVs with $P_{\rm orb} \leq 86$ min were found, of which one may be white-dwarf dominated.

A final point of our comparison is to inspect whether, with regard to finding CVs near the period-minimum, SDSS is a super-set of the three surveys under inspection. The six CVs with $P_{\rm orb} \leq 86$ min in the HQS are SW UMa, T Leo, and DW Cnc and HT Cam, all of which were previously known CVs with substantial accretion activity (outbursts/X-ray emission), and the two new discoveries KV Dra (HS1449+6415), an SU UMa type dwarf nova with rare outbursts and weak X-ray emission (Jiang et al., 2000; Nogami et al., 2000), and V455 And (HS2331+3905), the only white-dwarf dominated period-minimum CV in the HQS (Araujo-Betancor et al., 2005c). The first superoutburst of V455 And was observed in September 2007, confirming it as a WZ Sge type dwarf nova with a superoutburst cycle $>$ 5 years. Of those six period-minimum systems in the HQS only T Leo, SW UMa, DW Cnc are in the footprint of SDSS DR6, and all were

spectroscopically followed-up by SDSS and, hence, (re-)identified as CVs.

The PG Survey contains three systems with $P_{\rm orb} \leq 86$ min: the previously known T Leo, and the PG discoveries RZ LMi and MM Hya (Green et al., 1982). RZ LMi is an SU UMa star with an ultra-short outburst cycle (Robertson et al., 1995; Nogami et al., 1995), which is thought to reflect an unusually high mass transfer rate for its orbital period (Osaki, 1995a,b). MM Hya is a relatively poorly studied dwarf nova with rather rare outbursts (Ringwald, 1993; Misselt & Shafter, 1995). The spectrum published by Zwitter & Munari (1996) is of low quality, but suggests that MM Hya may be a white-dwarf dominated CV similar to those discovered in large numbers by the SDSS. T Leo and RZ LMi are in the footprint of SDSS DR6, but only T Leo has been followed up spectroscopically. RZ LMi was found in the SDSS imaging at $g = 14.6$, close to the bright end where SDSS does follow-up observations, and was rejected by the quasar target selection.

In summary, comparing the numbers of period-minimum CVs found in the SDSS, HQS, and PG surveys with the normalised effective survey volumes shows that the three surveys produce broadly consistent results. The main gain that the SDSS brings over the previous surveys comes from its depth, and the massive spectroscopic follow-up of CV (and quasar) candidates.

The scale height of CVs

A simple statement on the scale height of CVs can be made simply from comparing the SDSS subsamples for $g_{\rm lim} = 19.0$, i.e. the CVs from the main quasar sample (which we have assumed to be approximately complete due to the colour-overlap between CVs and quasars), and the full sample with $g_{\rm lim} = 22.5$ (where SDSS makes no attempt to achieve any level of completeness, but merely allocates spare fibres to faint quasar candidates). Simple scaling of the survey volumes predicts an increase in the number of CVs by ~ 1.4 for an assumed $H_z = 190$ pc. This modest gain comes from the fact that, with a limiting distance of 302 pc, the main quasar survey at $g_{\rm lim} = 19.0$ already extends out to ~ 1.6 scale heights, and not many more CVs are found by going further into the halo. However, for an assumed $H_z = 260$ pc, the increase to $g_{\rm lim}$ is expected to be ~ 4. Going to $g_{\rm lim} = 22.5$ boosts the number of CVs actually found by SDSS by ~ 1.5, which exceeds the prediction for H_z. This is a very conservative lower limit, as (a) the spectroscopic follow-up of faint quasar candidates is by far not complete down to $g_{\rm lim} = 22.5$,

and (b) there are 16 more published WD-dominated systems without orbital period determination, of which 14 have $g > 19.0$. Given the properties of the systems shown in Figure 6.3, there is a $\sim 80\%$ probability that those 16 systems will have periods $P_{\rm orb} \leq 86$ min as well. We conclude from this empirical study that the scale height of CVs is very likely larger than the 190 pc used by Patterson (1984), and larger scale heights such as used by Pretorius et al. (2007a) should be more realistic.

6.5.2 Caveats?

An obvious question is *have we biased our follow-up in a way that would favour observations of short-period CVs*? If such a bias existed, the orbital period distribution resulting from the follow-up work would be skewed even within the SDSS CV sample, irrespective of the question of how representative this sample is of the true galactic CV population. As shown in Section 6.4, a large fraction of the systems in the period spike have white-dwarf dominated optical spectra. Among the remaining $\sim$ 130 SDSS CVs with no accurate period determination, the fraction of white-dwarf dominated systems is similar to that within the sample of well-studied systems discussed here, suggesting that the period distribution of these remaining systems should be overall similar to the one shown here. In addition, at least the earlier follow-up studies of SDSS CVs focused on brighter systems, for the obvious reason of them being easier observational targets. Hence, the early follow-up was more likely to target intrinsically bright systems, which implies relatively high accretion rates, and on average periods above the spike. Finally, as it is evident from Figure 6.1 (right panel), the 44 previously known CVs with accurate periods *do not* show a period minimum spike. Among the $\sim$ 130 SDSS CVs with no accurate period, there is only a handful of additional previously known systems, and one might expect that the fraction of systems within the period spike will be higher in the remaining new SDSS discoveries. In summary, we are confident that our follow-up strategy has not introduced a significant bias with respect to the orbital periods of the systems studied so far. However, given that the fraction of well-studied systems among the SDSS CV sample is still relatively small ($< 50\%$), further follow-up work is highly desirable.

Another caveat to bear in mind is that the intrinsic and observed CV populations may be made up of different evolutionary channels. It has been suggested that the strong magnetic

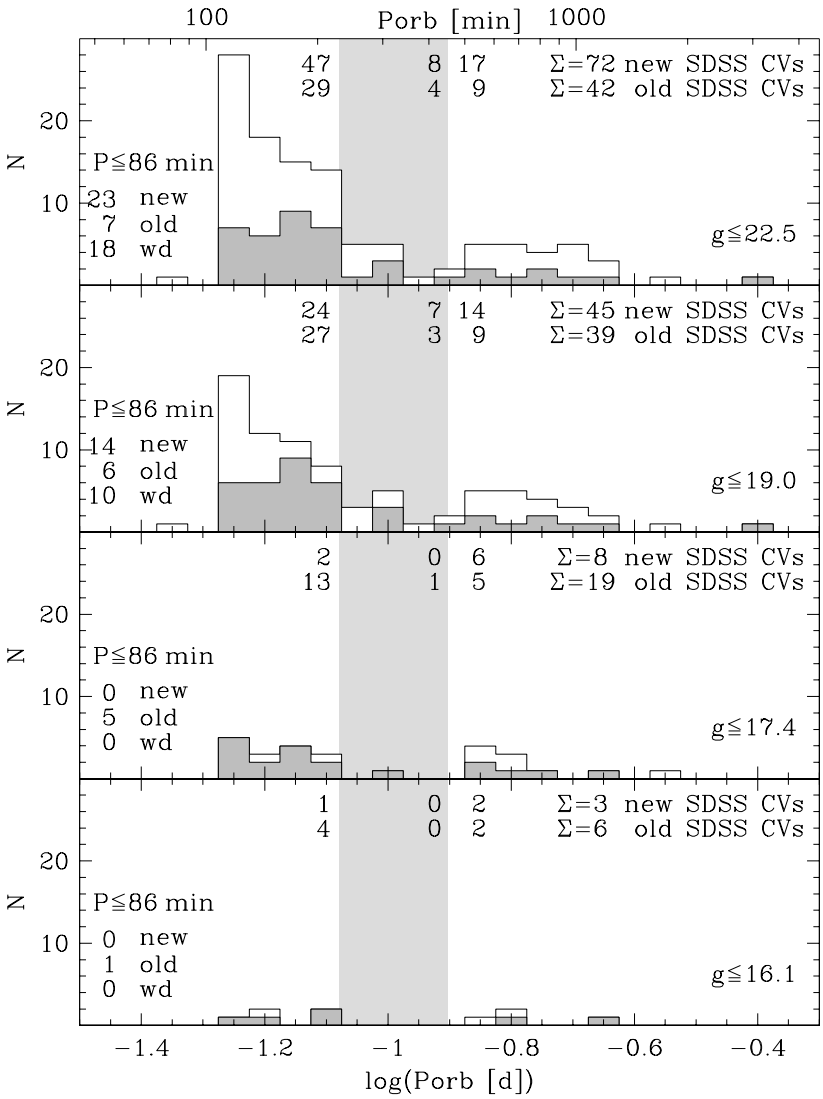

Figure 6.5: The orbital period distributions of the new SDSS CVs (Table 6.1, white histograms) and the old SDSS CVs (Table 6.2, grey) applying four different magnitude limits. From top to bottom: $g \leq 22.5$, corresponding to the faintest CV included in our sample; $g \leq 19.0$, corresponding to the magnitude limit of the low-redshift quasar survey within SDSS, $g \leq 17.5$ corresponding to the magnitude limit of the Hamburg Quasar Survey; and $g \leq 16.1$, corresponding to the magnitude limit of the Palomar Green Survey. The number of systems below, in, and above the 2–3 h period gap as well as their sum are given in each panel, with the values for the new SDSS CVs being on top of those for the old SDSS CVs. The number of new SDSS CVs, old SDSS CVs, and white-dwarf dominated CVs in the $\sim 80 - 86$ min period spike are shown on the left of the period histogram.

field in polars will reduce the rate at which magnetic braking extracts angular orbital momentum (Webbink & Wickramasinghe, 2002), which would result in different evolutionary timescales between non-magnetic and strongly magnetic CVs. Observations show that at any given orbital period the white dwarfs in polars are on average colder than those in non-magnetic CVs, with the difference being strongest above the period gap. This suggests that the secular mean of the mass transfer rates in polars is indeed lower than in non-magnetic CVs (Sion, 1991; Townsley & Bildsten, 2003; Araujo-Betancor et al., 2005b). The fraction of confirmed magnetic systems among the SDSS CVs is $\simeq 20\,\%$, very similar to the numbers found for the general CV population (Wickramasinghe & Ferrario, 2000), but their total number is yet too small to test for a difference in their period distribution compared to the non-magnetic systems.

Another channel that is likely to add noticeably to the CV population are systems which started with a mass ratio $M_{\rm donor}/M_{\rm wd} \gtrsim 1$, and underwent a phase of thermal time-scale mass transfer (TTMT) before evolving into CVs (Schenker et al., 2002; Podsiadlowski et al., 2003). A number of suspected post-TTMT systems have been found (e.g. Thorstensen et al., 2002b,a; Gänsicke et al., 2003), but again their number is too small to assess their effect on the overall orbital period distribution of CVs.

6.5.3 Implications on CV Population Models

From our follow-up studies of CVs discovered by SDSS we have identified the "spike" at the minimum period predicted by theory for two decades. Bearing in mind the caveats outlined above, what other implications can we derive from the SDSS CV sample at the current stage of follow-up, with only about half of the systems having reliable orbital periods? Assuming the standard CV evolution scenario, and a mid-plane CV space density of $5 \times 10^{-5}{\rm pc}^{-3}$, Pretorius et al. (2007a) calculated the period distributions of various magnitude-limited samples, and found that the period minimum spike decreases in prominence for brighter magnitude limits, although it was still present in a sample with $V < 14$ with a contrast of two with respect to neighbouring periods.

In Figure 6.5.1, we show the period distributions of the SDSS CVs, as before divided in new and old systems, for the four different magnitude limits used in the previous sections, $g_{\rm lim} = 22.5, 19.0, 17.4, 16.1$. The accumulation of systems at the minimum period is clearly

Table 6.4: WZ Sge candidate systems brighter than $V \simeq 17$ identified prior to SDSS, V_q = magnitude in quiescence.

System	$V_{\rm q}$	$d\,[pc]$	M_V	Ref.
WZ Sge	15.0	$43 \pm ^{1.6}_{1.5}$	11.8	1,2,3
BW Scl	16.4	131 ± 18	10.8	4,5,6
GD 552	16.5	105 ± 20	11.4	7,8
V455 And	16.5	$74 \pm ^{8}_{7}$	12.2	8,9
GW Lib	16.7	$104 \pm ^{30}_{20}$	11.6	10,11

[1]Mackie (1920), [2]Thorstensen (2003), [3]Harrison et al. (2004), [4](Augusteijn & Wisotzki, 1997), [5](Abbott et al., 1997), [6](Gänsicke et al., 2005), [7]Greenstein & Giclas (1978), [8]Unda-Sanzana et al. submitted, [9]Araujo-Betancor et al. (2005c), [10]Gänsicke et al. in prep, [11]Maza & Gonzalez (1983),

present in the full sample, and still so once a $g_{\rm lim} = 19.0$ cut is applied. At $g_{\rm lim} = 17.4$, the number of systems in shortest-period bin still exceeds all other three bins below the period gap, but numbers are too small to draw any firm conclusion. This being said, we note that a similar "accumulation" in the shortest-period bin was found in the period distribution of HQS CVs, which is an independent sample with the same magnitude limit (see Figure 18 of Aungwerojwit et al. 2006). Cutting to $g_{\rm lim} = 16.1$, the limit of the PG survey, only five systems are left below the period gap, and hence no statement with regard to a period spike can be done.

From Figure 6.5.1, it is clear that SDSS is picking up many new short-period CVs at magnitudes fainter than $g_{\rm lim} \simeq 17.5$. In particular, SDSS has found a large number of CVs that have white-dwarf dominated optical spectra, which must have very low-mass donor stars as little or not spectral features from the companions are seen, and orbital periods right at the minimum period. Taking their properties at face value, it appears likely that all these systems are WZ Sge type dwarf novae, that have very long outburst recurrence times. There is no plausible selection mechanism within the fibre allocation of SDSS that would go *against* finding this type of system at bright magnitudes $g \simeq 15 - 17.5$, but not a single bright WZ Sge candidate has been found by SDSS, which suggests that they are probably relatively rare.

This suggestion is confirmed by looking at how many bright WZ Sge (candidate) stars were known prior to SDSS. In Table 6.4, we list the WZ Sge (candidate) systems from Ritter & Kolb (2003) (V7.9) which are brighter than $V \simeq 17$ in quiescence. The absolute magnitudes for these five systems, $< M_V >= 11.6 \pm 0.5$, agree well with our estimate for the white-dwarf

dominated SDSS systems (Section 6.5.1). WZ Sge and GW Lib were discovered through their large-amplitude outbursts, and BW Scl, GD 552, and V455 And were identified through follow-up spectroscopy of ROSAT X-ray sources, high proper motion objects, and emission line stars from the HQS, respectively. With the exception of GD 552, all systems have white-dwarf dominated spectra with no spectroscopic evidence for the mass donors. Thus, it appears that no matter what selection method is used, WZ Sge stars are not very numerous.

The standard CV population models predict that $\sim$ 99% of all CVs should have periods $\lesssim$ 2 h, and $\sim$ 70 % should be post-bounce systems (Kolb, 1993; Howell et al., 2001). If we follow Pretorius et al. (2007a), and take the average of the space densities predicted by CV evolution theory, $\rho = 5 \times 10^{-5}\mathrm{pc}^{-3}$ (de Kool, 1992; Politano, 1996), we expect $\sim$ 210 CVs within a radius of 100 pc of the Earth, and practically all of them should be short-period systems, of which $\sim$ 150 post-bounce. While estimating a CV space density from the SDSS CV sample is beyond the scope of this paper, we feel confident to rule out space densities as high as $\rho = 5 \times 10^{-5}\mathrm{pc}^{-3}$, which is in line with previous observational constraints advocating lower values (e.g. Patterson, 1984; Ringwald, 1996; Patterson, 1998; Araujo-Betancor et al., 2005b; Aungwerojwit et al., 2006; Pretorius et al., 2007c)

So far, convincing observational evidence for the existence of post-bounce CVs has been meagre – primarily so because of the extreme low luminosity of very low-mass brown dwarf donor stars. SDSS has identified a large number of eclipsing CVs, among which are about half a dozen systems with $P_{\mathrm{orb}} \leq 86$ min. (Littlefair et al., 2006b, 2007, 2008) have demonstrated that precise measurements of the donor star masses in these systems can be achieved from modelling high-quality eclipse light curves, leading to the identification of 5 CVs with donor star masses below the hydrogen burning limit. Littlefair et al. (2008) show that among the eclipsing CVs near the period minimum, the number of systems with brown-dwarf donors is roughly consistent with the theoretical predictions.

6.6 Conclusions

SDSS is providing us with the largest, deepest, and most homogeneously selected CV sample so far, and holds the potential of detailed tests of the current models of compact binary evolution.

Follow-up studies are currently available for about half of the SDSS CVs, and we have analysed the global properties of this sample, with particular emphasis on the numerous short-period systems. In summary, we find that:

1. The period distribution of the SDSS CVs differs significantly from that of any previous CV sample, containing a much larger fraction of short-period CVs. Most striking is the appearance of an accumulation of CVs with $80 \lesssim P_{\rm orb} \lesssim 86$ min, which we identify as the period-minimum spike predicted for two decades by CV population models.

2. Within the period minimum spike, the majority of new CVs identified by SDSS have optical spectra dominated by the white dwarf, with very low levels of accretion luminosity. We determine an average absolute magnitude of $< M_g >= 11.6 \pm 0.7$ for these systems. The spectra are usually devoid of spectroscopic signatures from the mass donors, implying very late spectral types and low masses. Work by Littlefair et al. (2006b, 2007, 2008) confirms that a high fraction of the eclipsing systems in the period-minimum spike contain brown dwarf donors.

3. Comparison with the Hamburg Quasar Survey and the Palomar Green Survey suggests that the main advantage of SDSS is indeed its unprecedented depth. Comparing subsamples of the SDSS CVs with different magnitude limits indicates that the scale height of short-period CVs is $H_z > 190$ pc.

4. The total number of short-period CVs identified by SDSS is incompatible with a space density as high as 5×10^{-5} pc, the average predicted by different CV population models. A more precise estimate of the CV space density using the SDSS sample should await a more complete follow-up of the CV sample, and a detailed investigation of the CV completeness within the spectroscopic identification carried out by SDSS.

Chapter 7

Conclusions and Future Work

7.1 Results in Context

I started this thesis by putting into context the study of Cataclysmic Variables and how due to their large number and the relatively simple nature of their stellar components, CVs hold a great potential to test and improve our understanding of compact binary evolution, in particular that of orbital angular momentum loss and the impact of mass loss on the structure of the donor star.

A recently updated and revised edition of the Ritter & Kolb catalogue; V7.9, includes all literature published before 31 December 2007 and the catalogue is now comprised of 700 CVs with known orbital periods. All these systems have been found by a variety of different means, and as such the sample has been subject to a variety of observational selection effects and biases that are difficult to quantify.

I then discussed how, over the years, the theory of 'disrupted magnetic braking' used to explain the most prominent features of the orbital period distribution, has been subject to a number of modifications/alternatives. This has been done in a bid to counter the discrepancies between theoretical predictions and observational evidence, and to match the predicted orbital period distribution, the total space density of CVs, and the expected tight correlation between orbital period and mass transfer rate.

While these discrepancies may be partially related to shortcomings in the theories of common envelope evolution and orbital angular momentum loss, it is clear that the heterogeneous set of known CVs (Ritter & Kolb, 2003) is not well-suited for a quantitative test of the

population models.

I then introduced the Sloan Digital Sky Survey (SDSS). Seen by many as the means to solving many of these long standing problems, it has proved its potential to dramatically improve the observational side of CV population studies. Sampling a large volume in *ugriz* colour space and extending deeper than any previous large-scale survey, SDSS has delivered the most homogeneous and complete sample of CVs to date.

The work presented in this thesis is part of a larger effort on the part of our team based at Warwick to establish the properties of the intrinsic population of CVs in our Galaxy, with the aim to derive the orbital period distribution of the SDSS CV sample. In 2004/05 our group was awarded time via the International Time Programme on La Palma, to acquire time-series photometric and spectroscopic observations which were carried out as part of the follow-up observations for SDSS CVs.

The SDSS sample thus far contains 116 CVs with known orbital periods. 72 of these systems are newly identified and 44 are re-identified or previously known systems. In this thesis (Chapters 4 and 5), I presented my contribution to this project: the results of time-series photometric and time-series spectroscopic observations of 29 systems – 25% of the overall SDSS sample, from which I determined orbital periods for 20 of these systems – 28% of the newly identified systems.

Figure 7.1 shows the orbital period distribution of these 20 CVs. In summary, 3 of the systems lie above the gap, 2 within the gap, and 15 below (3/4 of the sample). Of these 15 objects, 6 are found within the 80–86 min period spike. The exact location of the orbital periods for CVs from photometric sample from Chapter 4, and the photometric and spectroscopic sample from Chapter 5 have been highlighted with tick-marks. My sample has been superimposed on the 116 *SDSS CVs* from Table 6.1 & 6.2. These systems are all CVs with an SDSS spectrum that allows their identification as a CV in Data Release 6 (DR6, Adelman-McCarthy et al. 2007), independently of whether they were already known before or not, and also on the 455 CVs from *non-SDSS* CVsRitter & Kolb (2003; V7.6) – excluding systems with spectroscopy in SDSS DR6 and systems whose periods are marked as uncertain.

In Chapter 4 and 5, I plotted the orbital period distribution for each sample , comparing it to the *non-SDSS* CV sample from the Ritter & Kolb catalogue. I also carried out a two-sided

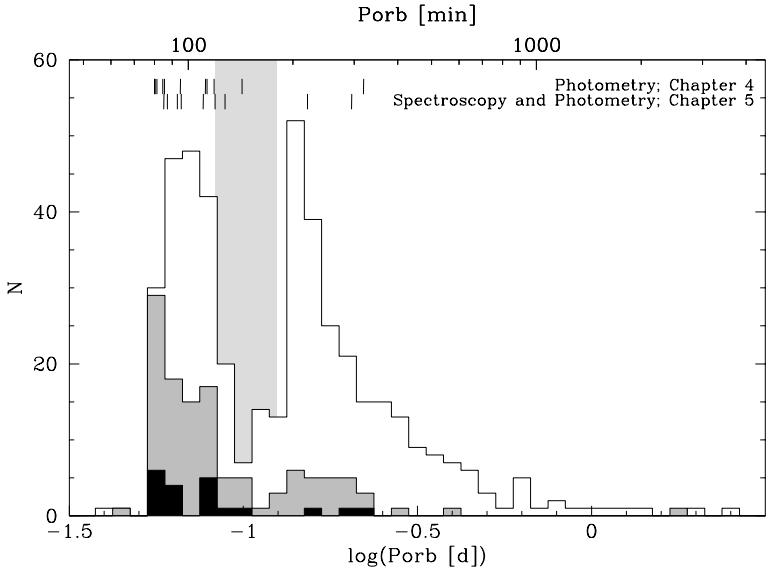

Figure 7.1: The orbital period distribution of all 20 CVs discussed in this thesis (*black*); 3 of the systems lie above the gap, 2 within the gap, and 15 below. 6 are within the 80–86 min period spike. The location of the orbital periods for CVs from photometric sample from Chapter 4, and Chapter 5 are highlighted with tick-marks. My sample has been superimposed on the 116 SDSS CVs (*grey*) and the 455 CVs from Ritter & Kolb (2003; V7.6) catalogue (*white*). The grey region corresponds to the 2-3 hr period gap. Note: The photometric sample seems to show only 10 tick marks, this is because two of the systems, SDSS J1711+3013 and SDSS J2116+1134 have very close orbital periods – $P_{\rm orb}$=80.35 min and $P_{\rm orb}$=80.2 min respectively, and so the tick marks overlap.

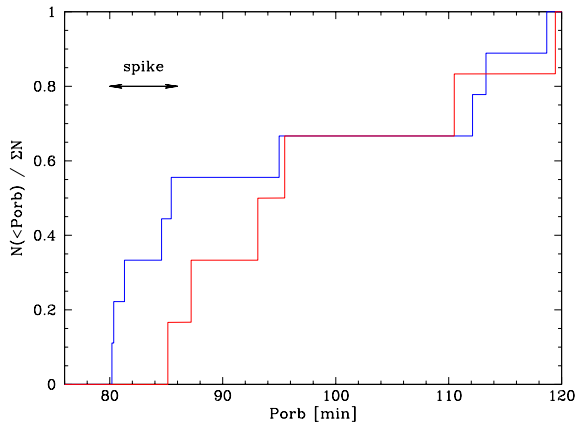

Figure 7.2: Normalised cumulative period distributions in the range $P_{\rm orb}$ = 76 – 120 min of the 9 CVs from Chapter 4; photometric sample (blue) and 6 CVs from Chapter 5; photometric and spectroscopic sample (red). A two-sided Kolmogorov-Smirnov test comparing the distributions of the two samples shows the probability that the CVs from the purely photometric sample and the combined spectroscopic and photometric sample are drawn from the same parent population is 36.3%.

Kolmogorov-Smirnov test, to see whether or not each new sample of SDSS CVs deviated from the previously known *non-SDSS* CV sample in a statistically significant way.

The result of the KS test for the photometric sample gave a 12.8% probability of the two distributions being drawn from the same parent population, whilst the same test for the mainly spectroscopic sample of CVs gave a 51.2% probability. Considering the mean *g*-magnitude for the respective samples; $< g_{phot} >= 19.14$ and $< g_{spec} >= 18.26$, the results seem to suggest that the two samples may differ from each other in their intrinsic properties. The difference of 0.88 mag implies that the photometric sample may contain systems with intrinsically lower mass transfer rates than the mainly spectroscopic sample. In order to test this supposition, I carried out a KS test to compare the two samples.

Figure 7.2 shows the cumulative distribution between the 9 CVs of photometric sample and the 6 CVs of the mainly spectroscopic sample found in the period range 76 min–120 min. A Kolmogorov-Smirnov test comparing the two samples gives a 36.3% probability of them being drawn from the same parent population. This results implies that the two samples are not statistically different, although we note that the sample sizes are small.

The orbital periods for 11 systems in my sample could not be determined. For the majority of these objects, the reason was usually a lack of sufficient quality and/or quantity of data,

due to limited amount of observing time. Other factors that can also prevent an orbital period from being determined are instrumental constraints, such as spectral resolution and insufficient signal-to-noise ratio. These effects are particularly important in spectroscopic observations due the intrinsic faintness of the target or poor weather conditions.

The interplay between these two factors are particularly important in spectroscopic observations due to the intrinsic faintness of the target or poor weather conditions. For instance even with a high signal-to-noise, low spectral resolution can prevent the determination of an accurate orbital period, this is because the motion in the line may not be resolved. An example of such a case was SDSS J2258−0949 (Figure 5.2). Here the low spectral resolution resulted in relatively large error ($P_{\rm orb}$ = 119.45 ± 3.92 min) when comparing the values to other CVs. Conversely, a low signal-to-noise ratio, even with high resolution can result in the loss of information and also prevent the accurate determination of an orbital period. Consider the case of SDSS J2048−0610 ($P_{\rm orb}$ = 87.5 ± 0.3 min). Examination of the radial velocity plot shows large error bars (Figure 5.2). A double-Gaussian analysis was used to determine the radial velocity variations. This technique is sensitive to motion in the line wings – associated with the inner regions of the accretion disc, so a high signal-to-noise is necessary in order to measure the excess flux over the continuum.

The method of observation used, i.e. photometry vs spectroscopy, can also effect whether or not variability associated with the orbital period can be discerned within the data. The main issues are the rate of change of variability within a system, its duration, whether or not it is associated with the orbital period, amplitude of the variation, and the system's inclination to the line of sight. In the latter case; in photometric observation of a low inclination system will display constant luminosity at all points during the orbital cycle and in spectroscopic observations, a low inclination system means that radial velocity variations will not be detected. As a result in both situations, an orbital period will not be deduced. In the majority of situations, these problems can be dealt with by gathering as much high quality data as possible.

Let us put some of these examples in context.

Photometry: For some systems, the variation in luminosity associated with the orbital period occurs over a timescale much longer than the observation. A number of systems display variability unrelated to the orbital period. Consider SDSS J0018+3454 (Section 4.2.1), this sys-

tem shows small scale fluctuations (0.1 mag on a timescales of 20-40 min) in its lightcurve but is suspected to have a long period (possibly > 24 h). In SDSS J2101+1052 (Section 5.2.11) the lightcurve of this system (Homer et al., 2006b) shows fluctuations of 1.0 mag. Due to the 'short' length of observations it is uncertain as to how the timescales of these variations are linked to the orbital period. However this system has been compared to HS 0943+1404 (Rodríguez-Gil et al., 2005b) a confirmed IP. This system shows a similar lightcurve and analysis has shown that the features within the light curve are a combination of the orbital and spin periods. Longer photometric observations should solve this problem. Conversely a situation can exist where the accretion disc is very bright, out–shining any other time varying component in a CV such as the accretion spot and so displaying little variation during the orbital cycle. An example of this is seen in HS 0139+0559 (Aungwerojwit et al., 2005). This system has a period of $P_{\rm orb} = 243$ min, 'displays thick disc spectra and displays no photometric variability'. A similar phenomenon of little to no photometric variability can be observed for systems with very low mass transfer rates such as SDSS J1514+4549 (Section 4.2.12). A low luminosity disc and bright spot meant that our two observations of this system showed a constant mean magnitude $g \simeq 20.2$, so no orbital period could be determined through photometry.

Spectroscopy: As with photometric observations there are a number of reasons why radial velocity variations may not be observed and are insufficient in determining an orbital period for a system. Again a fundamental reason is that the variation associated with the orbital period is not observable during the course of observation. This could be the fact that the orbital period of the system is long. Long orbital periods (which also imply lower radial velocities) means that longer observations are necessary to discern the variations associated with the orbital period. One system already discussed in this thesis is SDSS J1703+3209 (Section 5.2.9), which is suspected to have a long period, and displayed no radial velocity variations during observations.

Chapter 6 is the culmination of all the work that has been carried out on all SDSS CVs to date. Here I discussed the differences in the orbital period distribution of the 455 *non-SDSS* CV and the 116 *SDSS* CVs and 72 *new-SDSS*. As with the previous chapters I plotted orbital period distributions and carried out a KS test on the three samples. The results of the test were much more conclusive. The orbital period distribution of the 116 *SDSS* CVs display a clear accumulation of systems close to the period minimum, with a substantially larger fraction of

below-the-gap to above-the-gap systems (Gänsicke et al. 2008 in prep). These results corroborate the trend already noticed by Southworth et al. (2006, 2007b) and Szkody et al. (2007a), who noticed a larger fraction of short-period systems among the SDSS CVs compared to the previously known CVs (see e.g. Aungwerojwit et al. 2006 for CVs from the Hamburg Quasar Survey or Pretorius et al. 2007a for CVs from the Palomar Green Survey) indicating that the survey was possibly detecting candidates from a previously under-sampled population of CVs.

The KS test gave a 0.9% probability that *non-SDSS* CVs and the *SDSS CVs* sample were drawn from the same parent population, indicating that the two distributions differ at a 3σ level. In addition further analysis of the properties of the systems accumulating at the period minimum displayed distinct spectroscopic characteristics. These systems were white dwarf dominated implying extremely low accretion rates expected of old evolved CVs, further evidence that SDSS is now acquiring a very different sample of CVs.

More specifically, the origin of the 80–86 min period spike is entirely due to the new CVs identified in SDSS. The systems in the period spike differ also in spectral morphology and accretion activity from the longer-period CVs. Indeed $\sim$ 20% of the CVs identified by SDSS have white-dwarf dominated spectra (PSI–VI), the majority of which have been found close to the period minimum. In fact 18 of the 30 SDSS CVs in the 80–86 min period spike are newly discovered systems with white-dwarf dominated optical spectra; this generally indicates that the accretion disc is dim, and that the donor star is of a late spectral type and that the mass transfer rate is low. These systems are most likely all WZ Sge-type dwarf novae with extremely long recurrence times, with SDSS J0804+5103 being so far the only white-dwarf SDSS CV outing itself as a WZ Sge.

7.2 Current State of the Field

The field of Cataclysmic Variable study, is as ever a combination of population studies, theoretical modelling and indepth studies of individuals systems. However with the acquisition of such a large sample of CVs from SDSS, all these areas have certainly received a boost in observational data and leads. There is definitely a more concerted effort into characterising a large and well-defined and homogeneous sample of CVs with accurately determined orbital periods, stellar masses and distances, so that the statistical properties can be used to test theories of CV evolution.

At the time of writing, the sample of definite SDSS CVs contains 213 systems, of which 177 are new discoveries (Szkody et al., 2007a). Data Release 7 is due for publication in November 2008, and at this current rate of discovery, the number of systems identified by Sloan may reach 250 systems even 300 if we choose to be optimistic. Establishing the detailed properties of these CVs is a labour intensive task, but by the end of this project, we can be certain that SDSS will have provided the astronomical community with the largest and homogenously selected sample of CVs to date. The newly identified CVs are currently being followed-up by a number of groups (e.g. Wolfe et al., 2003; Pretorius et al., 2004; Woudt & Warner, 2004; Peters & Thorstensen, 2005; Roelofs et al., 2005; Tramposch et al., 2005; Gänsicke et al., 2006; Southworth et al., 2006, 2007a,b; Littlefair et al., 2006a,b).

Regardless of the fact that there are still at least a few years of research before orbital periods can be determined for all CVs within the spectroscopic database, SDSS has already made an important breakthrough. The existence of the long sought after period minimum spike is now a reality and has provided answers and confirmation to an aspect of CV evolution which has been a bone of contention for the past 20 years. As the number of CVs grows so the prominence of the spike will be enhanced further.

With the increased number of systems, another issue is what the implication will be on the derived space density of CVs. This is uncertain. Theoretical predictions of CV space densities are typically higher than those derived from observations. As discussed in Chapter 2, population synthesis suggests that the space density of CVs should range from $10^{-5} - 10^{-4}\mathrm{pc}^{-3}$ (Politano, 1996; de Kool, 1992), whereas the number derived from observations is $10^{-6} - 10^{-5}\mathrm{pc}^{-3}$ (Downes, 1986; Ringwald, 1996; Pretorius et al., 2007b; Araujo-Betancor et al., 2005a; Aung-

werojwit et al., 2006). If the standard model is correct, then the vast number of systems below the period gap would imply a high space density. Unfortunately, current observations have so far identified only 1-10% (Gänsicke et al., 2002b) of the predicted CV population.

Details of space densities are discussed in Chapter 6, but if the method of Pretorius et al. (2007a) is followed and the average of the space densities predicted by CV evolution theory, $\rho = 5 \times 10^{-5}\mathrm{pc}^{-3}$ (de Kool, 1992; Politano, 1996) is used, we expect $\sim$ 210 CVs within a radius of 100 pc of the Earth, and practically all of them should be short-period systems, of which $\sim$ 150 post-bounce. Estimating a CV space density from the SDSS CV sample is beyond the scope of this thesis, but the total number of short-period CVs identified by SDSS is so far incompatible with a space density as high as $5 \times 10^{-5}\mathrm{pc}^{-3}$. A more precise estimate of the CV space density using the SDSS sample is in need of a more complete follow-up of the CV sample, and a detailed investigation of the CV completeness within the spectroscopic identification carried out by SDSS. As a result the estimates of the number densities are unlikely to change in the near future.

In the mean time determination of orbital parameters and investigations of the intrinsic properties of SDSS systems has led to a couple of very interesting discoveries. Firstly, for systems with periods below 86 min, there have been a number of confirmed non-radial white dwarf pulsators orbital periods within the spike (Woudt & Warner, 2004; Woudt et al., 2005; Gänsicke et al., 2006; Nilsson et al., 2006). In this thesis SDSS J0919+0857 (Mukadam et al., 2007) is a confirmed pulsator and SDSS J1457+5148 is also possible candidate, worthy of further investigation. In these systems low mass transfer rates allow for white dwarfs to be cool enough to drive pulsations (Townsley & Bildsten, 2003; Arras et al., 2006).

Finally, the first definite detections of brown-dwarf-mass secondary stars in CVs have been made. Three of the four SDSS CVs with a confirmed brown-dwarf donor are located within the period spike (SDSS J1035+0551, SDSS J1433+1011, and SDSS J1501+5501, Littlefair et al. 2006b, 2008) which confirm long standing theoretical predictions (Littlefair et al., 2006b, 2007). The standard CV population models predict that $\sim$ 99% of all CVs should have periods $\lesssim$ 2 h, and $\sim$ 70 % should be post-bounce systems (Kolb, 1993; Howell et al., 2001) and it is these systems which are most likely highly evolved CVs that have passed beyond the period minimum.

7.3 The Future of Understanding Binary Evolution

The period distribution of SDSS CVs (Figure 6.1) displays a clear spike at the minimum period which is totally absent in the population of previously known CVs. A much higher fraction of the SDSS CVs have $P_{\rm orb} < 2.5\,{\rm hr}$ (81% versus 44% for the previously known population of CVs), but this fraction is still lower than the predicted (99%). It is apparent that although the most quiet and elusive members of the CV population may have been found, a lot of work is necessary to ensure the numbers add up.

I believe future aims and motivations should be to avoid selection effects within the SDSS CV sample that is being followed up. The majority of SDSS CVs are serendipitously discovered amongst the UV excess quasar targets and the SDSS quasar selection is 95% complete (Richards et al., 2004) to a limiting (de-reddened) magnitude of i=19.1. The completeness for the Galactic foreground CVs is assumed to be the same for $g < 19.0$ and it is this magnitude limited sample which should recieve complete attention. Figure 7.3 shows that there is currently still a strong magnitude bias in this sample, with a significant drop in the fraction of systems with measured $P_{\rm orb}$ for $18 \leq g \leq 19$. By observing all the systems within the magnitude limit of $g < 19.0$, the bias can be removed to construct a well defined sample which can then be used to help constrain and test theoretical models of CV evolution.

As part of the afore mentioned motivations, a fundamental analysis of the statistical completeness of the SDSS sample of CVs is important. *Has SDSS found all the CVs that it could possibly find within the* $g < 19.0$ *limit?* To this end we must also ask the following; *Are there any objects with spectra, which are CVs that have not been positively identified?* and *How complete is the spectroscopic follow-up of CVs as a function of colour?*

One can assume, that once CVs have made their way into Sloan's spectroscopic database, the probability of identification is close to 100%, using techniques involving both automated searches and visual inspection for the different types of systems as done by Szkody et al.. A recent undergraduate project at Warwick, supervised by Boris Gänsicke, involved the search of Balmer/He emission line objects in the SDSS database. The results are very promising, the student found all but 2-3 of the CVs as originally identified by Szkody et al. and identified only 1-2 (very faint) systems not previously published by Szkody et al..

The completeness of the spectroscopic follow-up, i.e. the fraction of CVs within the

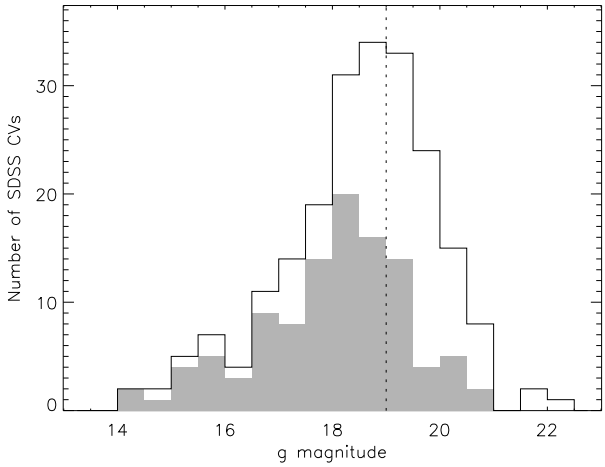

Figure 7.3: *g*-magnitude distribution of 212 SDSS CVs (white), and of 108 with an accurate period measurement (grey) . The magnitude limit $g \leq 19.0$ is marked with a dashed line, and corresponds to the magnitude limit for which the SDSS UV-excess quasar survey is 95% complete. The fraction of CVs with period measurements get lower towards fainter magnitudes, so this sample is biased towards brighter systems. (Figure provided by John Southworth, priv. comm.)

photometric data base for which a spectrum was taken is hoped to be as complete as the SDSS UV-excess survey – 95% at the overlap between QSO and CV colours. This is the region in colour space for which the greatest number of fibres have been allocated to possible QSO targets. However this number is expected to be much lower in other regions of colour space not occupied by QSOs. As CVs inhabit a broad area in colour space, it is feasible to assume that a number of objects with peculiar/extreme colours not associated with QSOs but possibly with CVs have been ignored for spectroscopic follow-up. It is also possible that there exists a very small fraction of objects with follow-up spectra, have yet to be positively identified as CVs.

This analysis, can be expected to be comparable to that carried out by Roelofs et al. (2007) and their study of the AM CVn population from the SDSS. Roelofs et al. carried out an analysis of the spectroscopic follow-up of AM CVns as a function of *u-g* and *g-r*, to a limiting magnitude of $g = 21$. They produced a grey-scale plot which highlighted the areas in colour-space which had received the spectroscopic follow-up with the greatest to the least intensity . It is apparent that an analogous process for CVs would be necessary, in *ugriz* colour space of SDSS to a limiting magnitude of $g = 19.0$. This procedure will be more involved, not only due to the fact that the analysis will be carried out over four dimensional colour space but also because

CVs occupy a large region in colour space compared to AM CVns. The results can then be used to speculate the expected number of CVs in each region of colour space, which in turn, could be compared the number of CVs which actually exist in the SDSS database. This task would involve considering how many CVs were found from the fraction of objects with spectroscopic follow-up. For example, if for every 100 photometric targets, there were 50 objects which had spectra taken and only one resulted in the positive identification of a CV, we can assume if spectra were taken of the remaining photometric targets, at least one other CV would be found.

I believe by ensuring the complete follow-up of the SDSS CV sample, and carrying out detailed investigations of CV completeness within the spectroscopic database of SDSS it would be possible to derive space densities more representative of the intrinsic population of CVs. The result could then be incorporated into population synthesis models to help to modify some of our theories of CV evolution.

Another area of study that will most definitely see growth in the coming years in the follow-up study of brown-dwarf donor systems. According to the standard theory these post-bounce systems make up to 70% of systems below the period gap. Recent studies by Littlefair et al. 2008 of a number of eclipsing systems has allowed for the determination of white dwarf and brown dwarf masses. Further acquisition of observational evidence is necessary to deal with the discrepancies between theory and observational evidence. If successful, like the discovery of the spike at the minimum orbital period, the discovery of a large population of post period bouncers could be another success story in our understanding of binary evolution.

Bibliography

Abbott, T. M. C., Fleming, T. A., Pasquini, L., 1997, A&A, 318, 134

Adelman-McCarthy, J. K., et al., 2007, ApJS, 172, 634

Ak, T., Retter, A., Liu, A., Esenoğlu, H. H., 2005, Publications of the Astronomical Society of Australia, 22, 105

Anderson, S. F., et al., 2005, AJ, 130, 2230

Andronov, N., Pinsonneault, M., Sills, A., 2003, ApJ, 582, 358

Araujo-Betancor, S., Gänsicke, B. T., Long, K. S., Beuermann, K., de Martino, D., Sion, E. M., Szkody, P., 2005a, ApJ, 622, 589

Araujo-Betancor, S., Gänsicke, B. T., Long, K. S., Beuermann, K., de Martino, D., Sion, E. M., Szkody, P., 2005b, ApJ, 622, 589

Araujo-Betancor, S., et al., 2005c, A&A, 430, 629

Arras, P., Townsley, D. M., Bildsten, L., 2006, ApJ Lett., 643, L119

Augusteijn, T., Wisotzki, L., 1997, A&A, 324, L57

Aungwerojwit, A., 2007, PhD Thesis; The properties of a spectroscopically selected sample of Cataclysmic Variables, Deparment of Physics, Warwick

Aungwerojwit, A., et al., 2005, A&A, 443, 995

Aungwerojwit, A., et al., 2006, A&A, 455, 659

Barker, J., Kolb, U., 2003, MNRAS, 340, 623

Beers, T. C., Rossi, S., Ulrich, D., Wilhelm, R., 1996, 112, 1188

Berger, J., Fringant, A.-M., 1984, A&A, 58, 565

Bergeron, P., Wesemael, F., Beauchamp, A., 1995, PASP, 107, 1047

Bertin, E., Arnouts, S., 1996, A&AS, 117, 393

Beuermann, K., Thomas, H.-C., Reinsch, K., Schwope, A. D., Trümper, J., Voges, W., 1999, A&A, 347, 47

Bond, H. E., White, R. L., Becker, R. H., O'Brien, M. S., 2002, PASP, 114, 1359

Bonnet-Bidaud, J. M., Mouchet, M., Somova, T. A., Somov, N. N., 1996, A&A, 306, 199

Boyd, D., Oksanen, A., Henden, A., 2006, Journal of the British Astronomical Association, 116, 187

Boyd, D., Shears, J., Koff, R., 2007, ArXiv e-prints

Bruch, A., Engel, A., 1994, A&AS, 104, 79

Burleigh, M. R., et al., 2006, MNRAS, 373, 1416

Burwitz, V., et al., 1998, A&A, 331, 262

Chen, A., O'Donoghue, D., Stobie, R. S., Kilkenny, D., Warner, B., 2001, MNRAS, 325, 89

Christian, D. J., Craig, N., Dupuis, J., Roberts, B., 2001, Informational Bulletin on Variable Stars, 5032, 1

Cropper, M., 1989, MNRAS, 236, 935

de Kool, M., 1992, A&A, 261, 188

de Kool, M., Ritter, H., 1993, A&A, 267, 397

Dhillon, V. S., Jones, D. H. P., Marsh, T. R., Smith, R. C., 1992, MNRAS, 258, 225

Dillon, M., et al., 2008, MNRAS, 386, 1568

Downes, R. A., 1986, ApJ, 307, 170

Downes, R. A., Webbink, R. F., Shara, M. M., Ritter, H., Kolb, U., Duerbeck, H. W., 2001, PASP, 113, 764

Eggleton, P. P., 1983, ApJ, 268, 368

Esamdin, A., Dong, X., Zhao, Y., 1997, IAU Circ., 6763

Fan, X., 1999, 117, 2528

Farihi, J., Burleigh, M. R., Hoard, D. W., 2008, ApJ, 674, 421

Faulkner, J., 1971, ApJ Lett., 170, L99

Feline, W. J., Dhillon, V. S., Marsh, T. R., Brinkworth, C. S., 2004a, MNRAS, 355, 1

Feline, W. J., Dhillon, V. S., Marsh, T. R., Stevenson, M. J., Watson, C. A., Brinkworth, C. S., 2004b, MNRAS, 347, 1173

Feline, W. J., Dhillon, V. S., Marsh, T. R., Watson, C. A., Littlefair, S. P., 2005, MNRAS, 364, 1158

Frescura, F. A. M., Engelbrecht, C. A., Frank, B. S., 2007, ArXiv e-prints

Fukugita, M., Ichikawa, T., Gunn, J. E., Doi, M., Shimasaku, K., Schneider, D. P., 1996, AJ, 111, 1748

Gänsicke, B. T., Szkody, P., Howell, S. B., Sion, E. M., 2005, ApJ, 629, 451

Gänsicke, B. T., 2000, Reviews of Modern Astronomy, 13, 151

Gänsicke, B. T., 2005, in Hameury & Lasota (2005), p. 3, p. 3

Gänsicke, B. T., Sion, E. M., Beuermann, K., Fabian, D., Cheng, F. H., Krautter, J., 1999, A&A, 347, 178

Gänsicke, B. T., Fried, R. E., Hagen, H.-J., Beuermann, K., Engels, D., Hessman, F. V., Nogami, D., Reinsch, K., 2000, A&A, 356, L79

Gänsicke, B. T., Fischer, A., Silvotti, R., de Martino, D., 2001, A&A, 372, 557

Gänsicke, B. T., Beuermann, K., Reinsch, K., eds., 2002a, The Physics of Cataclysmic Variables and Related Objects, ASP Conf. Ser. 261

Gänsicke, B. T., Hagen, H. J., Engels, D., 2002b, in Gänsicke et al. (2002a), p. 190, p. 190

Gänsicke, B. T., Hagen, H. J., Engels, D., 2002c, in Gänsicke et al. (2002a), p. 190, p. 190

Gänsicke, B. T., Araujo-Betancor, S., Hagen, H.-J., Harlaftis, E. T., Kitsionas, S., Dreizler, S., Engels, D., 2004, A&A, 418, 265

Gänsicke, B. T., et al., 2003, ApJ, 594, 443

Gänsicke, B. T., et al., 2006, MNRAS, 365, 969

Gianninas, A., Bergeron, P., Fontaine, G., 2006, AJ, 132, 831

Green, R. F., Ferguson, D. H., Liebert, J., Schmidt, M., 1982, PASP, 94, 560

Green, R. F., Schmidt, M., Liebert, J., 1986, ApJS, 61, 305

Greenstein, J. L., Giclas, H., 1978, PASP, 90, 460

Gunn, J. E., et al., 1998, 116, 3040

Hagen, H.-J., Groote, D., Engels, D., Reimers, D., 1995, A&AS, 111, 195

Hagen, H.-J., Engels, D., Reimers, D., 1999, A&AS, 134, 483

Hameury, J.-M., Lasota, J.-P., eds., 2005, The Astrophysics of Cataclysmic Variables and Related Objects, ASP Conf. Ser. 330

Harrison, T. E., Johnson, J. J., McArthur, B. E., Benedict, G. F., Szkody, P., Howell, S. B., Gelino, D. M., 2004, AJ, 127, 460

Hellier, C., Ramseyer, T. F., Jablonski, F. J., 1994, MNRAS, 271, L25

Hoard, D. W., Szkody, P., 1997, ApJ, 481, 433

Hoard, D. W., Linnell, A. P., Szkody, P., Fried, R. E., Sion, E. M., Hubeny, I., Wolfe, M. A., 2004, ApJ, 604, 346

Homer, L., Szkody, P., Chen, B., Henden, A., Schmidt, G., Anderson, S. F., Silvestri, N. M., Brinkmann, J., 2006a, AJ, 131, 562

Homer, L., Szkody, P., Henden, A., Chen, B., Schmidt, G. D., Fraser, O. J., West, A. A., 2006b, AJ, 132, 2743

Homer, L., et al., 2005, ApJ, 620, 929

Horne, J. H., Baliunas, S. L., 1986, ApJ, 302, 757

Horne, K., Marsh, T. R., Cheng, F. H., Hubeny, I., Lanz, T., 1994, ApJ, 426, 294

Howell, S., Szkody, P., 1988, PASP, 100, 224

Howell, S. B., Warnock, A., Mason, K. O., Reichert, G. A., Kreidl, T. J., 1988, MNRAS, 233, 79

Howell, S. B., Szkody, P., Kreidl, T. J., Mason, K. O., Puchnarewicz, E. M., 1990, PASP, 102, 758

Howell, S. B., Sirk, M. M., Malina, R. F., Mittaz, J. P. D., Mason, K. O., 1995a, ApJ, 439, 991

Howell, S. B., Szkody, P., Cannizzo, J. K., 1995b, ApJ, 439, 337

Howell, S. B., Rappaport, S., Politano, M., 1997, MNRAS, 287, 929

Howell, S. B., Nelson, L. A., Rappaport, S., 2001, ApJ, 550, 897

Iben, I. J., 1991, ApJS, 76, 55

Iben, I., J., Tutukov, A. V., 1993, ApJ, 418, 343

Jester, S., et al., 2005, 130, 873

Jiang, X. J., Engels, D., Wei, J. Y., Tesch, F., Hu, J. Y., 2000, A&A, 362, 263

Katajainen, S., Lehto, H. J., Piirola, V., Karttunen, H., Piironen, J., 2000, A&A, 357, 677

Katajainen, S., Butters, O. W., Norton, A. J., Lehto, H. J., Piirola, V., 2007, A&A, 475, 1011

Kato, T., Nogami, D., Matsumoto, K., Baba, H., 2004, PASJ, 56, 109

Kilkenny, D., O'Donoghue, D., Koen, C., Stobie, R. S., Chen, A., 1997, MNRAS, 287, 867

King, A. R., 1988, QJRAS, 29, 1

King, A. R., Kolb, U., 1995, ApJ, 439, 330

King, A. R., Schenker, K., 2002, in Gänsicke et al. (2002a), p. 233, p. 233

King, A. R., Schenker, K., Hameury, J. M., 2002, MNRAS, 335, 513

Knigge, C., 2006, MNRAS, 373, 484

Knigge, C., Long, K. S., Hoard, D. W., Szkody, P., Dhillon, V. S., 2000, ApJ Lett., 539, L49

Kolb, U., 1993, A&A, 271, 149

Kolb, U., Baraffe, I., 1999, MNRAS, 309, 1034

Kolb, U., Ritter, H., 1992, A&A, 254, 213

Kolb, U., Stehle, R., 1996, MNRAS, 282, 1454

Kolb, U., King, A. R., Ritter, H., 1998, MNRAS, 298, L29

Liebert, J., Tapia, S., Bond, H. E., Grauer, A. D., 1982, ApJ, 254, 232

Littlefair, S. P., Dhillon, V. S., Marsh, T. R., Gänsicke, B. T., 2006a, MNRAS, 371, 1435

Littlefair, S. P., Dhillon, V. S., Marsh, T. R., Gänsicke, B. T., Southworth, J., Watson, C. A., 2006b, Science, 314, 1578

Littlefair, S. P., Dhillon, V. S., Marsh, T. R., Gänsicke, B. T., Baraffe, I., Watson, C. A., 2007, MNRAS, 381, 827

Littlefair, S. P., Dhillon, V. S., Marsh, T. R., Gänsicke, B. T., Copperwheat, C., 2008, in Phelan, D., Ryan, O., Shearer, A., eds., High Time Resolution Astrophysics: The Universe at Sub-Second Timescales, vol. 984 of *American Institute of Physics Conference Series*, p. 23

Lupton, R., Gunn, J. E., Ivezić, Z., Knapp, G. R., Kent, S., 2001, in Harnden, Jr., F. R., Primini, F. A., Payne, H. E., eds., Astronomical Data Analysis Software and Systems X, vol. 238 of *Astronomical Society of the Pacific Conference Series*, p. 269

Mackie, J., 1920, Astronomische Nachrichten, 210, 79

Marsh, T. R., 1989, PASP, 101, 1032

Martinez-Pais, I. G., Casares, J., 1995, MNRAS, 275, 699

Maza, J., Gonzalez, L. E., 1983, IAU Circ., 3854, 2

Mennickent, R., 1994, A&A, 285, 979

Mennickent, R. E., Diaz, M. P., 2002, MNRAS, 336, 767

Mennickent, R. E., Tovmassian, G., Zharikov, S. V., Tappert, C., Greiner, J., Gänsicke, B. T., Fried, R. E., 2002, A&A, 383, 933

Misselt, K. A., Shafter, A. W., 1995, AJ, 109, 1757

Morris, S. L., Schmidt, G. D., Liebert, J., Stocke, J., Gioia, I. M., Maccacaro, T., 1987, ApJ, 314, 641

Mukadam, A. S., Winget, D. E., von Hippel, T., Montgomery, M. H., Kepler, S. O., Costa, A. F. M., 2004, ApJ, 612, 1052

Mukadam, A. S., Gänsicke, B. T., Szkody, P., Aungwerojwit, A., Howell, S. B., Fraser, O. J., Silvestri, N. M., 2007, ApJ, 667, 433

Nilsson, R., Uthas, H., Ytre-Eide, M., Solheim, J.-E., Warner, B., 2006, MNRAS, 370, L56

Nogami, D., Kato, T., Masuda, S., Hirata, R., Matsumoto, K., Tanabe, K., Yokoo, T., 1995, PASJ, 47, 897

Nogami, D., Masuda, S., Kato, T., 1997, PASP, 109, 1114

Nogami, D., Kato, T., Baba, H., Masuda, S., 1998, PASJ, 50, L1

Nogami, D., Engels, D., Gänsicke, B. T., Pavlenko, E. P., Novák, R., Reinsch, K., 2000, A&A, 364, 701

Nogami, D., Kato, T., Baba, H., Novák, R., Lockley, J. J., Somers, M., 2001, MNRAS, 322, 79

Norton, A. J., Wynn, G. A., Somerscales, R. V., 2004, ApJ, 614, 349

O'Donoghue, D., et al., 2006, MNRAS, 372, 151

Osaki, Y., 1974, PASJ, 26, 429

Osaki, Y., 1995a, PASJ, 47, L11

Osaki, Y., 1995b, PASJ, 47, L25

Osborne, J. P., Beardmore, A. P., Wheatley, P. J., Hakala, P., Watson, M. G., Mason, K. O., Hassall, B. J. M., King, A. R., 1994, MNRAS, 270, 650

Paczyński, B., 1971, ARA&A, 9, 183

Paczynski, B., 1976, in Eggleton, P., Mitton, S., Whelan, J., eds., IAU Symp. 73: Structure and Evolution of Close Binary Systems, D. Reidel, Dordrecht, p. 75

Paczyński, B., 1981, Acta Astronomica, 31, 1

Paczynski, B., Sienkiewicz, R., 1981, ApJ Lett., 248, L27

Paczyński, B., Sienkiewicz, R., 1983, ApJ, 268, 825

Patterson, J., 1984, ApJS, 54, 443

Patterson, J., 1994, PASP, 106, 209

Patterson, J., 1998, PASP, 110, 1132

Patterson, J., Richman, H., Kemp, J., Mukai, K., 1998a, PASP, 110, 403

Patterson, J., Kemp, J., Jensen, L., Vanmunster, T., Skillman, D. R., Martin, B., Fried, R., Thorstensen, J. R., 2000a, PASP, 112, 1567

Patterson, J., et al., 1998b, PASP, 110, 1290

Patterson, J., et al., 2000b, PASP, 112, 1584

Patterson, J., et al., 2003, PASP, 115, 1308

Patterson, J., et al., 2004, PASP, 116, 516

Patterson, J., et al., 2005, PASP, 117, 1204

Pavlenko, E., et al., 2007, in Napiwotzki, R., Burleigh, M. R., eds., 15th European Workshop on White Dwarfs, vol. 372 of *Astronomical Society of the Pacific Conference Series*, p. 511

Peters, C. S., Thorstensen, J. R., 2005, PASP, 117, 1386

Podsiadlowski, P., Han, Z., Rappaport, S., 2003, MNRAS, 340, 1214

Politano, M., 1996, ApJ, 465, 338

Postnov, K. A., Yungelson, L. R., 2006, Living Reviews in Relativity, 9, 6

Potter, S. B., O'Donoghue, D., Romero-Colmenero, E., Buckley, D. A. H., Woudt, P. A., Warner, B., 2006, MNRAS, 371, 727

Press, W., Teukolsky, S., Vetterling, W., Flannery, B., 1992, Numerical Recipes in FORTRAN 77, Cambridge Univ. Press, Cambridge

Pretorius, M. L., Woudt, P. A., Warner, B., Bolt, G., Patterson, J., Armstrong, E., 2004, MNRAS, 352, 1056

Pretorius, M. L., Knigge, C., Kolb, U., 2007a, MNRAS, 374, 1495

Pretorius, M. L., Knigge, C., Kolb, U., 2007b, in di Salvo, T., Israel, G. L., Piersant, L., Burderi, L., Matt, G., Tornambe, A., Menna, M. T., eds., The Multicolored Landscape of Compact Objects and Their Explosive Origins, vol. 924 of *American Institute of Physics Conference Series*, p. 546

Pretorius, M. L., Knigge, C., O'Donoghue, D., Henry, J. P., Gioia, I. M., Mullis, C. R., 2007c, MNRAS, 382, 1279

Pringle, J. E., Wade, R. A., 1985, Astronomy Express, 1, 159

Rappaport, S., Joss, P. C., Webbink, R. F., 1982, ApJ, 254, 616

Rappaport, S., Joss, P. C., Verbunt, F., 1983, ApJ, 275, 713

Rebassa-Mansergas, A., Gänsicke, B. T., Rodríguez-Gil, P., Schreiber, M. R., Koester, D., 2007, MNRAS, 382, 1377

Remillard, R. A., Schachter, J. F., Silber, A. D., Slane, P., 1994, ApJ, 426, 288

Richards, G. T., et al., 2002, AJ, 123, 2945

Richards, G. T., et al., 2004, ApJS, 155, 257

Ringwald, F., 1993, The Cataclysmic Variables from the Palomar-Green Survey, Ph.D. thesis, Dartmouth College

Ringwald, F. A., 1996, in Evans, A., Wood, J. H., eds., Cataclysmic Variables and Related Objects, no. 158 in IAU Coll., Kluwer, Dordrecht, p. 89

Ringwald, F. A., Thorstensen, J. R., Hamwey, R. M., 1994, MNRAS, 271, 323

Ritter, H., Kolb, U., 1998, A&AS, 129, 83

Ritter, H., Kolb, U., 2003, A&A, 404, 301

Robertson, J. W., Honeycutt, R. K., Turner, G. W., 1995, PASP, 107, 443

Rodrigues, C. V., Jablonski, F. J., D'Amico, F., Cieslinski, D., Steiner, J. E., Diaz, M. P., Hickel, G. R., 2006, MNRAS, 369, 1972

Rodríguez-Gil, P., 2005, in Hameury & Lasota (2005), p. 335, p. 335

Rodríguez-Gil, P., Gänsicke, B. T., Araujo-Betancor, S., Casares, J., 2004, MNRAS, 349, 367

Rodríguez-Gil, P., Gänsicke, B. T., Hagen, H.-J., Marsh, T. R., Harlaftis, E., Kitsionas, S., Engels, D., 2005a, A&A, 431, 269

Rodríguez-Gil, P., Schmidtobreick, L., Gänsicke, B. T., 2007a, MNRAS, 374, 1359

Rodríguez-Gil, P., et al., 2005b, A&A, 440, 701

Rodríguez-Gil, P., et al., 2007b, MNRAS, 377, 1747

Roelofs, G. H. A., Groot, P. J., Steeghs, D., Nelemans, G., 2004, in Tovmassian, G., Sion, E., eds., Compact Binaries and Beyond, no. 20 in Conf. Ser., RMAA, p. 254

Roelofs, G. H. A., Groot, P. J., Marsh, T. R., Steeghs, D., Barros, S. C. C., Nelemans, G., 2005, MNRAS, 361, 487

Roelofs, G. H. A., Nelemans, G., Groot, P. J., 2007, MNRAS, 382, 685

Rogoziecki, P., Schwarzenberg-Czerny, A., 2001, MNRAS, 323, 850

Scargle, J. D., 1982, ApJ, 263, 835

Schenker, K., King, A. R., 2002, in Gänsicke et al. (2002a), p. 242, p. 242

Schenker, K., King, A. R., Kolb, U., Wynn, G. A., Zhang, Z., 2002, MNRAS, 337, 1105

Schmidt, G. D., Hoard, D. W., Szkody, P., Melia, F., Honeycutt, R. K., Wagner, R. M., 1999, ApJ, 525, 407

Schmidt, G. D., Szkody, P., Silvestri, N. M., Cushing, M. C., Liebert, J., Smith, P. S., 2005a, ApJ, 630, L173

Schmidt, G. D., Szkody, P., Silvestri, N. M., Cushing, M. C., Liebert, J., Smith, P. S., 2005b, ApJ Lett., 630, L173

Schmidt, G. D., Szkody, P., Henden, A., Anderson, S. F., Lamb, D. Q., Margon, B., Schneider, D. P., 2007, ApJ, 654, 521

Schmidt, G. D., et al., 2005c, ApJ, 620, 422

Schneider, D. P., Young, P., 1980, ApJ, 240, 871

Schneider, D. P., et al., 2007, AJ, 134, 102

Schreiber, M. R., 2007, A&A, 466, 1025

Schreiber, M. R., Gänsicke, B. T., 2003, A&A, 406, 305

Schwarzenberg-Czerny, A., 1989, MNRAS, 241, 153

Schwarzenberg-Czerny, A., 1996, ApJ Lett., 460, L107

Schwope, A. D., Naundorf, C. E., Thomas, H.-C., Beuermann, K., 1991, A&A, 244, 373

Schwope, A. D., Brunner, H., Buckley, D., Greiner, J., Heyden, K. v. d., Neizvestny, S., Potter, S., Schwarz, R., 2002, A&A, 396, 895

Shafter, A. W., Szkody, P., 1984, ApJ, 276, 305

Shafter, A. W., Szkody, P., Thorstensen, J. R., 1986, ApJ, 308, 765

Shears, J., Brady, S., Foote, J., Starkey, D., Vanmunster, T., 2007a, ArXiv e-prints, 711

Shears, J., Klingenberg, G., de Ponthiere, P., 2007b, Journal of the British Astronomical Association, 117, 331

Silber, A. D., Remillard, R. A., Horne, K., Bradt, H. V., 1994, ApJ, 424, 955

Sills, A., Pinsonneault, M. H., Terndrup, D. M., 2000, ApJ, 534, 335

Sion, E. M., 1991, AJ, 102, 295

Sion, E. M., 1999, PASP, 111, 532

Skillman, D. R., Patterson, J., Thorstensen, J. R., 1995, PASP, 107, 545

Smak, J., 2002, Memorie della Societa Astronomica Italiana, 73, 206

Southworth, J., Gänsicke, B. T., Marsh, T. R., de Martino, D., Hakala, P., Littlefair, S., Rodríguez-Gil, P., Szkody, P., 2006, MNRAS, 373, 687

Southworth, J., Gänsicke, B. T., Marsh, T. R., de Martino, D., Aungwerojwit, A., 2007a, MNRAS, 378, 635

Southworth, J., Marsh, T. R., Gänsicke, B. T., Aungwerojwit, A., Hakala, P., de Martino, D., Lehto, H., 2007b, MNRAS, 382, 1145

Spruit, H. C., Ritter, H., 1983, A&A, 124, 267

Stanishev, V., Kraicheva, Z., Genkov, V., 2006, A&A, 455, 223

Steeghs, D., Perryman, M. A. C., Reynolds, A., de Bruijne, J. H. J., Marsh, T., Dhillon, V. S., Peacock, A., 2003, MNRAS, 339, 810

Stobie, R. S., et al., 1997, MNRAS, 287, 848

Stolz, B., Schoembs, R., 1984, A&A, 132, 187

Stoughton, C., et al., 2002, AJ, 123, 485

Szkody, P., Gänsicke, B. T., Howell, S. B., Sion, E. M., 2002a, ApJ Lett., 575, L79

Szkody, P., et al., 2002b, AJ, 123, 430

Szkody, P., et al., 2003a, AJ, 126, 1499

Szkody, P., et al., 2003b, ApJ, 583, 902

Szkody, P., et al., 2004, AJ, 128, 1882

Szkody, P., et al., 2005, AJ, 129, 2386

Szkody, P., et al., 2006, AJ, 131, 973

Szkody, P., et al., 2007a, AJ, 134, 185

Szkody, P., et al., 2007b, ApJ, 658, 1188

Taam, R. E., Sandquist, E. L., Dubus, G., 2003, ApJ, 592, 1124

Thomas, H. C., Beuermann, K., Reinsch, K., Schwope, A. D., Trümper, J., Voges, W., 1998, A&A, 335, 467

Thorstensen, J. R., 1997, PASP, 109, 1241

Thorstensen, J. R., 2003, AJ, 126, 3017

Thorstensen, J. R., Armstrong, E., 2005, AJ, 130, 759

Thorstensen, J. R., Fenton, W. H., 2002, PASP, 114, 74

Thorstensen, J. R., Taylor, C. J., 2001, MNRAS, 326, 1235

Thorstensen, J. R., Smak, J., Hessman, F. V., 1985, PASP, 97, 437

Thorstensen, J. R., Davis, M. K., Ringwald, F. A., 1991a, AJ, 102, 683

Thorstensen, J. R., Ringwald, F. A., Wade, R. A., Schmidt, G. D., Norsworthy, J. E., 1991b, AJ, 102, 272

Thorstensen, J. R., Patterson, J. O., Shambrook, A., Thomas, G., 1996, PASP, 108, 73

Thorstensen, J. R., Fenton, W. H., Patterson, J., Kemp, J., Halpern, J., Baraffe, I., 2002a, PASP, 114, 1117

Thorstensen, J. R., Fenton, W. H., Patterson, J. O., Kemp, J., Krajci, T., Baraffe, I., 2002b, ApJ Lett., 567, L49

Thorstensen, J. R., Patterson, J., Kemp, J., Vennes, S., 2002c, PASP, 114, 1108

Thorstensen, J. R., Fenton, W. H., Taylor, C. J., 2004, PASP, 116, 300

Tovmassian, G. H., Greiner, J., Zharikov, S. V., Echevarría, J., Kniazev, A., 2001, A&A, 380, 504

Townsley, D. M., Bildsten, L., 2003, ApJ Lett., 596, L227

Tramposch, J., Homer, L., Szkody, P., Henden, A., Silvestri, N. M., Yirak, K., Fraser, O. J., Brinkmann, J., 2005, PASP, 117, 262

Uemura, M., et al., 2000, PASJ, 52, L9+

Usher, P. D., Mattson, D., Warnock, III, A., 1982, ApJS, 48, 51

van Zyl, L., Warner, B., O'Donoghue, D., Sullivan, D., Pritchard, J., Kemp, J., 2000, Baltic Astronomy, 9, 231

Vanmunster, T., Velthuis, F., McCormick, J., 2000, Informational Bulletin on Variable Stars, 4955, 1

Verbunt, F., Zwaan, C., 1981, A&A, 100, L7

Voges, W., et al., 1999, A&A, 349, 389

Voges, W., et al., 2000, IAU Circ., 7432

Wagner, R. M., et al., 1998, AJ, 115, 787

Warner, B., 1986, MNRAS, 222, 11

Warner, B., 1995, Cataclysmic Variable Stars, Cambridge University Press, Cambridge

Warner, B., Woudt, P., 2004, in Kurtz, D. W., Pollard, K. R., eds., Variable Stars in the Local Group, ASP Conf. Ser. 310, p. 392

Webbink, R. F., Wickramasinghe, D. T., 2002, MNRAS, 335, 1

Wegner, G., Boley, F. I., 1993, AJ, 105, 660

Wickramasinghe, D. T., Ferrario, L., 2000, PASP, 112, 873

Willems, B., Kolb, U., Sandquist, E. L., Taam, R. E., Dubus, G., 2005, ApJ, 635, 1263

Wolfe, M. A., Szkody, P., Fraser, O. J., Homer, L., Skinner, S., Silvestri, N. M., 2003, PASP, 115, 1118

Woudt, P. A., Warner, B., 2004, MNRAS, 348, 599

Woudt, P. A., Warner, B., Pretorius, M., 2004, MNRAS, 351, 1015

Woudt, P. A., Warner, B., Pretorius, M. L., Dale, D., 2005, in Hameury & Lasota (2005), p. 325, p. 325

York, D. G., et al., 2000, AJ, 120, 1579

Zharikov, S. V., Tovmassian, G. H., Napiwotzki, R., Michel, R., Neustroev, V., 2006, A&A, 449, 645

Zharikov, S. V., et al., 2008, A&A, 486, 505

Zwitter, T., Munari, U., 1996, A&AS, 117, 449